Faculty of Physics and Applied Computer Science

Master thesis

Kacper Biłko

major: **technical physics**

Detailed analysis of the evolution and distribution of the total ionising dose in the LHC arc sections during the accelerator operation

Supervisor at CERN: **Dr. Oliver Stein**
Supervisor at AGH: **Dr. Krzysztof Malarz**

Krakow, November 2018

Aware of criminal liability for making untrue statements I declare that the following thesis was written personally by myself and that I did not use any sources but the ones mentioned in the dissertation itself.

Krakow, 29 November 2018

The subject of the master thesis and the internship by Kacper Biłko, student of 5th year major in technical physics

The subject of the master thesis: **Detailed analysis of the evolution and distribution of the total ionising dose in the LHC arc sections during the accelerator operation**

Supervisor:	Dr. Oliver Stein
Reviewer:	Prof. Dr. Tomasz Szumlak
A place of the internship:	CERN, Geneva, Switzerland

Programme of the master thesis and the internship

1. First discussion with the supervisor on realisation of the thesis.
2. The internship:
   - getting to know the idea of beam loss mechanisms and radiation monitoring at the LHC,
   - developing the software needed for the data analysis,
   - performing the first calculations,
   - discussion with the supervisor focused on the results obtained.
3. Continuation of calculations concerning the thesis subject.
4. Ordering and first analysis of the calculation results.
5. Final analysis of the results obtained, conclusions – discussion with and final approval by the thesis supervisor.
6. Typesetting the thesis.

Dean's office delivery:

Review by Supervisor

Review by Reviewer

Abstract

Continuous particle losses are an integral part of each accelerator operation. Even though they are only a very small fraction of the total intensity, they result in the occurrence of the mixed radiation fields that are hazardous for the reliability and lifespan of equipment including electronic devices. Especially at high energy and high intensity accelerators, like the accelerators at CERN, the mixed radiation fields can influence the operation. With focus on the Large Hadron Collider's (LHC) arc sections, where the magnets structure is a periodic FODO lattice, the total ionising dose distribution has been analysed. The LHC is equipped with a beam loss monitoring system that is used in order to ensure safety of the accelerator's apparatus, however it also provides high resolution dose measurements, both in space and time. The studies of the data presented in this work shows that among regular baseline radiation levels, spikes can be observed. They exceed the baseline levels by up to three orders of magnitude. The location, evolution and cause of these radiation spikes and general baseline behaviour are investigated in detail. For this analysis data from the beam loss monitoring system was used with the separation between the different beam modes of the LHC proton-proton operation from Run 2, that spans over the years 2015-2018.

Streszczenie

Ciągła utrata cząstek z wiązki jest nieodłącznym efektem funkcjonowania każdego akceleratora. Utracone cząstki powodują powstawanie promieniowania jonizującego, które stanowi potencjalne zagrożenie dla niezawodności urządzeń, w szczególności tych elektronicznych. Prawdopodobieństwo wystąpienia błędów, a w konsekwencji wymuszonych przerw w działaniu, wzrasta zarówno z energią, jak i liczbą cząstek w wiązce. Przykładami akceleratorów, w których problem jest obecny, są te w Europejskiej Organizacji Badań Jądrowych (CERN), z największym na świecie Wielkim Zderzaczem Hadronów (LHC) na czele. W pracy zbadano rozkłady dawek w odcinkach łukowych LHC, gdzie główne magnesy ułożone są w sposób periodyczny, w tzw. komórki FODO. Aby zapobiec potencjalnym uszkodzeniom sprzętu znajdującego się w okolicach akceleratora, w LHC zainstalowano system monitorujący utraty wiązki (BLM system). Choć nie jest to głównym przeznaczeniem, detektory systemu BLM można wykorzystać jako dozymetry. W całym LHC zainstalowano ich blisko 4000, a ich odczyty zapisywane są z dużą częstotliwością. Dostępne dane dozymetryczne cechują się zarówno dużą rozdzielczością przestrzenną, jak i czasową. Przy wykorzystaniu danych pochodzących z lat 2015-2018, zarejestrowanych podczas działania opartego o protony pokazano, że pośród regularnych i niskich poziomów dawek można zaobserwować miejsca, gdzie te wartości przekroczone są o blisko trzy rzędy wielkości. W ramach pracy opracowano narzędzia, a następnie przeanalizowano rozkłady i ewolucje dawek zarówno dla przypadków gdzie zarejestrowane wartości były niskie i powtarzalne, jak również dla miejsc, gdzie były one nieoczekiwane.

Acknowledgements

I am extremely grateful to my CERN's thesis supervisor, Dr. Oliver Stein, for all the invaluable support I have received during the studentship and encouragement during the thesis preparation. I would also like to express the deepest appreciation to my supervisor at the University, Dr. Krzysztof Malarz (AGH University of Science and Technology), for all the help I received all along my whole studies. Furthermore, I am deeply indebted to Dr. Fiona Harden for all the insightful comments and suggestions, especially regarding the linguistic aspects. This thesis would not have been possible without the guidance and help of Dr. Yacine Kadi (Monitoring and Calculation Working Group's chairman) and Dr. Ruben Garcia Alia (R2E project leader). Special thanks also to Dr. Anton Lechner and Cristina Bahamnonde Castro for providing the FLUKA simulation results for the LHC arc's half-cell. Finally, I would like to thank Dr. Markus Brugger for giving me the opportunity to be a part of the CERN's EN-EA group.

Contents

1. Introduction

CERN (European Organization for Nuclear Research) houses the largest accelerator complex in the world, with the most acclaimed accelerator being the Large Hadron Collider (LHC). The LHC spans a total circumference of almost 27 km across France and Switzerland and is home to four of the fundamental projects at CERN, i.e. ATLAS (A Toroidal LHC ApparatuS), ALICE (A Large Ion Collider Experiment), CMS (The Compact Muon Solenoid) and LHCb (The Large Hadron Collider beauty). At CERN scientists and engineers collaborate to investigate the underlying mechanisms of the Universe, such as Standard Model predictions (ATLAS and CMS), quark-gluon plasma (ALICE) and matter-antimatter inequalities (LHCb).

These mechanisms are examined by these projects (and others) via the analysis of interactions between highly energetic particles. To achieve these events, particle beams (protons or positive-charged ions) are created and accelerated in the chain of accelerators with the LHC at the end. Two beams, one accelerated clockwise and the other anti-clockwise, enables very high energy collisions (up to $14\,TeV$ in the center-of-mass frame) to occur. At these collisions desired events are observed. To increase the probability of observing the desired events, the number of high energy collisions, which is given in terms of the integrated luminosity, should be maximised.

Figure 1 illustrates the CERNs accelerator complex where the particles beam are accelerated in a the multistage process. At the LHC, in addition to the four experiments, four additional insertion regions (IR) housing additional accelerator equipment are located. They will be described in chapter 2.2.

With the maximum number of particles at the highest energy (7 TeV) more than 360 MJ are stored in each of the LHC beams. Uncontrolled fast losses of a fraction of the beam can already cause quenches or in worst case structural damages, thus stable and controlled operation is necessary to protect the LHC. In case of unstable and potentially dangerous accelerator operations the beams need to be extracted in a fast and controlled way. For this reason the LHC has dedicated beam extraction (dump) systems that can safely dissipate the energy if required.

During the LHC operation small fractions of the beams are being continuously lost, for example due to beam-residual gas interactions. The reasons are discussed in detail in chapter 2.6. As an integral part of the machine protection policy a Beam Loss Monitoring (BLM) system has been developed. It relies on approximately 4000 radiation detectors, mainly ionisation chambers, that provides an input to a Beam Interlock System. If a signal exceeds an allocated threshold, a beam permit is revoked and a beam dump is initiated.

As a consequence of beam losses, hadronic showers occur which results in mixed radiation fields that consist of both particles (hadrons and leptons) and photons. Here ionisation properties can affect electronic equipment which is installed in the tunnel and electronics failures might (and already did) interrupt the accelerators operation. In order to limit breakdowns caused by radiation, to evaluate risks

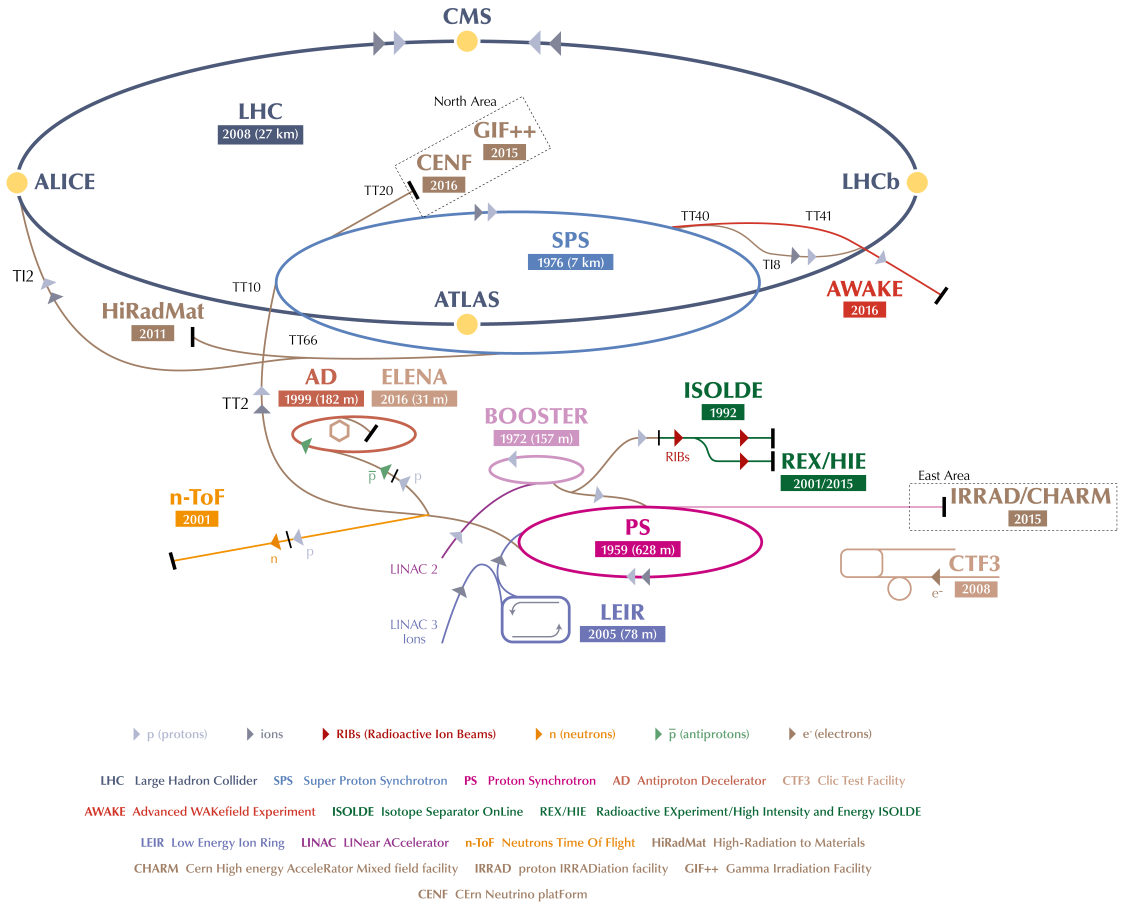

Figure 1: CERN accelerator complex [22].

and to optimise the lifespan of electronic equipment, a dedicated Radiation to Electronics (R2E) project has been established.

Within R2E, Monitoring and Calculation Working Group (MCWG) is investigating ways to improve the knowledge of mixed radiation fields. In addition the MCWG's mandate is to combining results from different radiation detectors in order to provide consolidated reports regarding radiation in the accelerator areas.

This thesis will present the methodology of BLM data analysis that is used by the MCWG and illustrate its direct application to evaluate the dose distribution along the LHC arc sections. There, magnets are placed in the sequence of FODO lattices with the period locations of beam loss monitors (BLMs). With the assumption that the main beam loss mechanism is beam-residual gas interaction and residual gas pressure is constant along an arc section it is expected that dose pattern is also periodic. However, despite the clearly determined baseline dose level spikes can be observed. Their evolutions, with respect to the baseline level, and causes are investigated since they are potentially dangerous for the accelerator components as well as its availability.

2. Theory

2.1. Basics of accelerators/colliders

According to Lorentz force definition (Equation (2.1)), only charged particles can interact with the electromagnetic (EM) field directly. To increase the particles energy an electric field (**E**) is needed, whereas to focus and steer them a magnetic one (**B**) is required. Even though electric field could be used for steering, it is more efficient to use magnetic field, since it scales with the velocity, that is in an ultrarelativistic regime.

$$\mathbf{F} = q\mathbf{E} + q\mathbf{v} \times \mathbf{B} \tag{2.1}$$

To accelerate particles to high energies, particle accelerator are used. There are two main concepts of accelerators that are currently being applied: linear, where the beam of particles travels along a straight line, and circular, where the beam circulates around the loop. The largest accelerators are circular. Such a choice allows a beam to be accelerated continuously because it can pass the acceleration region (Radio-Frequency Cavities) a multiple number of times. In linear accelerators many cavities are connected in series and beam passes them only once. The limitation factor is the maximum electric field that cannot cause breakdowns. On the contrary, synchotron radiation is produced around the ring which is sometimes undesired. By using hadrons instead of electrons, this effect can be decreased, even when accelerating to the same energies because its power scales $\sim \gamma^4$ (where γ is the Lorentz factor).

In circular accelerators it is convenient to define a co-moving coordinate frame with 3 coordinates: x and y which are horizontal and vertical positions in a transverse plane with respect to the third axis s, that is always tangential to the reference (designed) path.

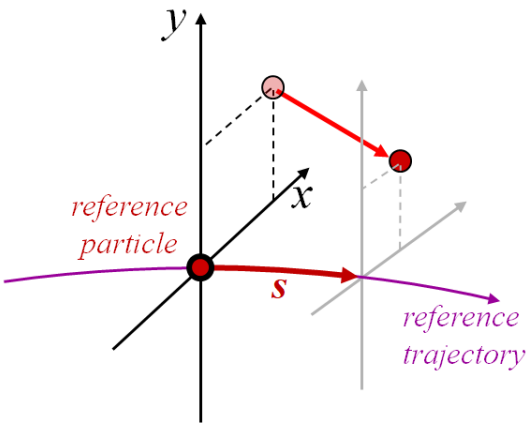

Figure 2: Concept of co-moving coordinate system used in accelerators. x and y are called horizontal and vertical transverse coordinates. [31].

Since it is not possible to set particles' transverse momenta to zero, focusing the beam becomes necessary. This can be achieved by quadrupole magnets that have focusing properties, but only in one plane. In the other transverse plane the beam is then defocused. The magnetic field of an ideal quadrupole is depicted in Figure 3.

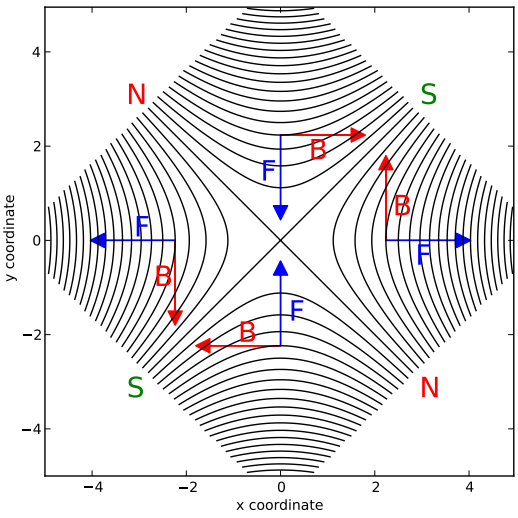

Figure 3: Magnetic field lines of a quadrupole field in the plane transverse to the beam direction [13]. **B** represents the magnetic field and **F** the corresponding Lorentz force direction in case of positive charged particle and velocity pointed into the plot.

To keep the trajectory inside the vacuum beam pipe and close to the design trajectory, focusing is performed in both planes, so that each particle from the beam oscillates around a reference trajectory (as depicted in Figure 4).

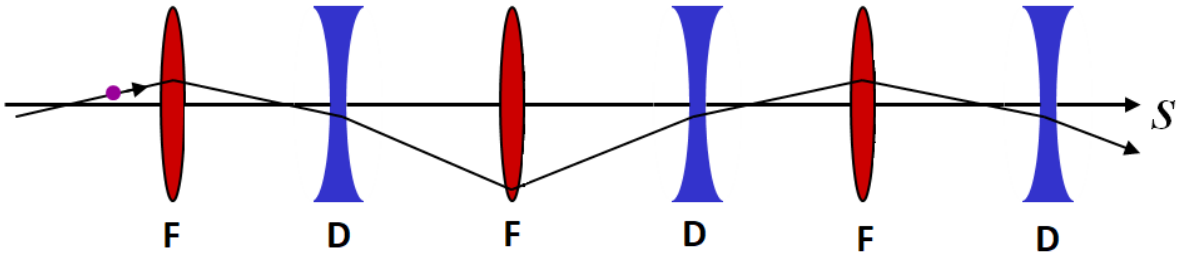

Figure 4: An exemplary particle trajectory through focusing (F) and defocusing (D) magnets (modified [31]). This particle is a part of beam.

Collider is an accelerator, that collides two counter-circulating beams with each other, not with the fixed target. It follows that available collision's energy is much higher, than it would be in a fixed target collision.

There are two key quantities describing each collider: the maximum energy of particles and the luminosity. It describes the efficiency of collisions, i.e. collision frequency normalised with the interaction cross-section. Often an integrated luminosity is used, which is an integral of the luminosity with respect to time. The objective is always to maximise integrated luminosity obtained at high energy.

For head-on collisions of two identical Gaussian shaped beams, the luminosity (L) can be defined as follows [9]:

$$L = f\frac{N_1 N_2}{4\pi\sigma_x\sigma_y} \tag{2.2}$$

where f is the revolution frequency, N_1 and N_2 are the intensities of two colliding bunches, and σ_y and σ_y are the bunches dimensions given in terms of gaussian standard deviation.

The beta function (β) describes optics (i.e. magnet configuration) of an accelerator. The beta function value at the collision point is denoted as β^*. The beam transverse size (σ) is connected with the the beta function via the beam emittance (ϵ), that describes the spread of particles in position-and-momentum phase space, through the equation (in the simplest case):

$$\sigma_{x,y} = \sqrt{\epsilon_{x,y}\beta_{x,y}} \tag{2.3}$$

By decreasing the value of a beta function at the collision point ($\beta^*_{x,y}$) and by increasing intensity, higher luminosity can be obtained because in general $\epsilon_{x,y}$ does not change.

2.2. Large Hadron Collider

The Large Hadron Collider (LHC) is the largest accelerator in the world, that can accelerate protons up to 7 TeV. The two beams circulates in the opposite directions and are collided at the centres of four experiments: ATLAS, ALICE, CMS and LHCb. Owing the fact that it was built in the already existing tunnel, in place of the LEP accelerator, the fixed accelerator's parameter was its circumference – 26658.883 m [6].

The LHC ring can be split into 8 arcs and 8 long-straight-sections (LSS). Each section consists of smaller sections that are called half-cells. An arc is defined as the part of the ring occupied by 46 regular half-cells [6]. An arc half-cell will be presented in chapter 2.3. An octant starts in the centre of an arc and goes to the centre of the next downstream (following the beam 1 direction) arc [6]. Approximately in the middle of each octant a long-straight-section (LSS), which at the LHC can be called insertion region (IR), is located. At the center[1] of each IR, the interaction point (IP) is located [6]. LSSs and arcs are interconnected via dispersion suppressors (DS), that adjusts beam optics between an arc and an IR. Scheme of the LHC is depicted in Figure 5.

Each IR plays different roles in the LHC operation.

Injection from the SPS is performed in two regions: beam 1 is injected upstream of IP2 and beam 2 upstream of IP8.

Acceleration is done in IR4 with the utilisation of radio-frequency (RF) cavities that provide longitudinal focusing of the particles in bunches[2] and acceleration.

Colliding is carried out at the centre of four experiments: ATLAS (IP1), ALICE (IP2), CMS (IP5) and LHCb (IP8).

Collimation is performed in both IR3 and IR7. In IR3 the beams are cleaned with respect to too large longitudinal oscillation amplitudes (momentum cleaning), whereas in IR7 with respect to too large transverse oscillation amplitudes (betatron cleaning) [6].

[1] IP8 is shifted with respect to the middle of IR

[2] time dependent electric field accelerates particles more if they are "late" and less if they are "untimely"

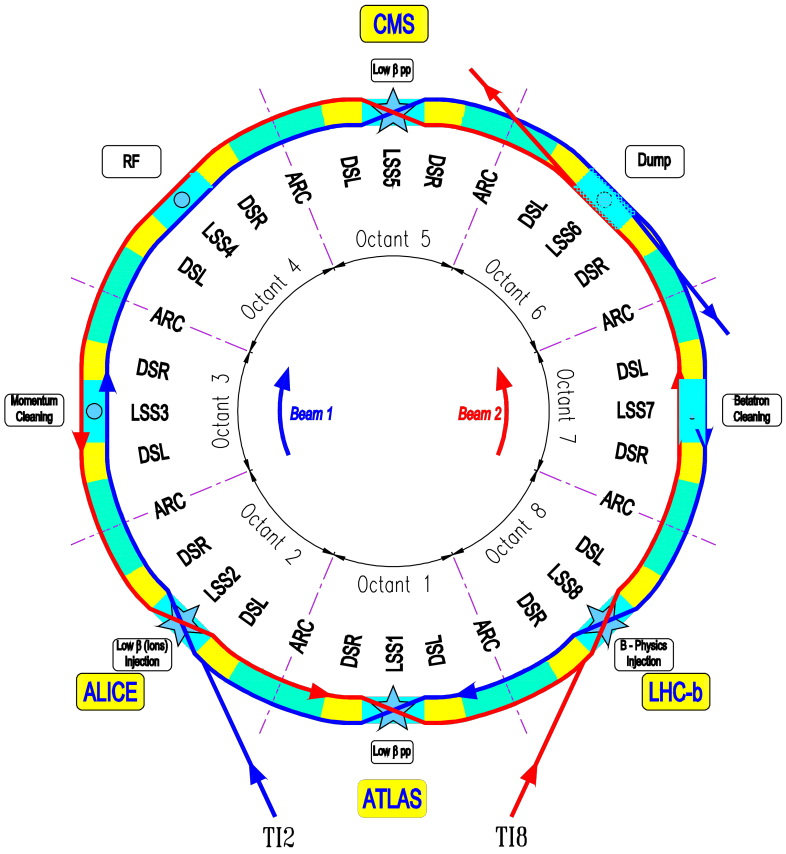

Figure 5: Scheme of the LHC [6].

Extraction is realised in IR6. Due to the amount of energy stored in the beams, the LHC needs to have a dedicated beam abort system in order to dispose the beams in a safe manner. Each ring has their own extraction system – Fast rising extraction magnets direct the beams into dedicated lines with massive dump blocks at the end where the beams are absorbed.

In order to keep the beams at the desired trajectories various magnets are used at the LHC. Providing particles with 7 TeV circulating in the LHC tunnel requires a bending magnetic field of more than 8 T. In ferromagnetic materials saturation effects can be observed at approximately 2 T, therefore superconducting NbTi coils are used. They are powered with the nominal current of 11.85 kA [6]. To ensure stable operation in a superconductive state they are cooled down to 1.8 K, which is far below critical temperature, with superfluid helium. Since its viscosity vanishes, pumping and distribution becomes simpler. ^{4}He loses its superfluidity at 2.17 K. At this temperature it has a peak in the heat capacity dependency. By operating close, but below the transition temperature, high heat capacity can be maintained. Approximately 11 GJ is stored in the 1232 bending magnets.

As a result of the injectors layout and machine protection, to obtain maximum luminosity (by design), particles at LHC are formed into 2808 bunches with 25 ns spacing, each one containing $1.15 \cdot 10^{11}$ particles [6]. Nonetheless, actually less bunches are being injected since each bunch has a higher density [28]. Bunches are not equally distributed, since bigger gaps are needed, e.g. to allow kicker magnets to raise. Moreover, the actual particles energy, that is 6.5 TeV, is lower than designed 7 TeV [24].

2.3. LHC arc section structure

The maximum energy of particles in the accelerator is determined by magnetic rigidity of the beam:

$$\frac{p}{q} = B\rho \tag{2.4}$$

where p is the particle momentum, q is the charge of the particle, B is a bending magnetic field, and ρ is the bending radius of a particle affected by the magnetic field.

As mentioned in chapter 2.2, a beam is divided into bunches, each one containing particles with non-zero transverse momenta, therefore active focusing becomes necessary so that the transverse dimensions of the beam are constrained inside the vacuum chamber. Evolution of the $\beta_{x,y}(s)$ (described in chapter 2.1) along an idealised FODO cells is presented in Figure 6. Focusing/defocusing quadrupoles are located in the extrema of a $\beta(s)$ function.

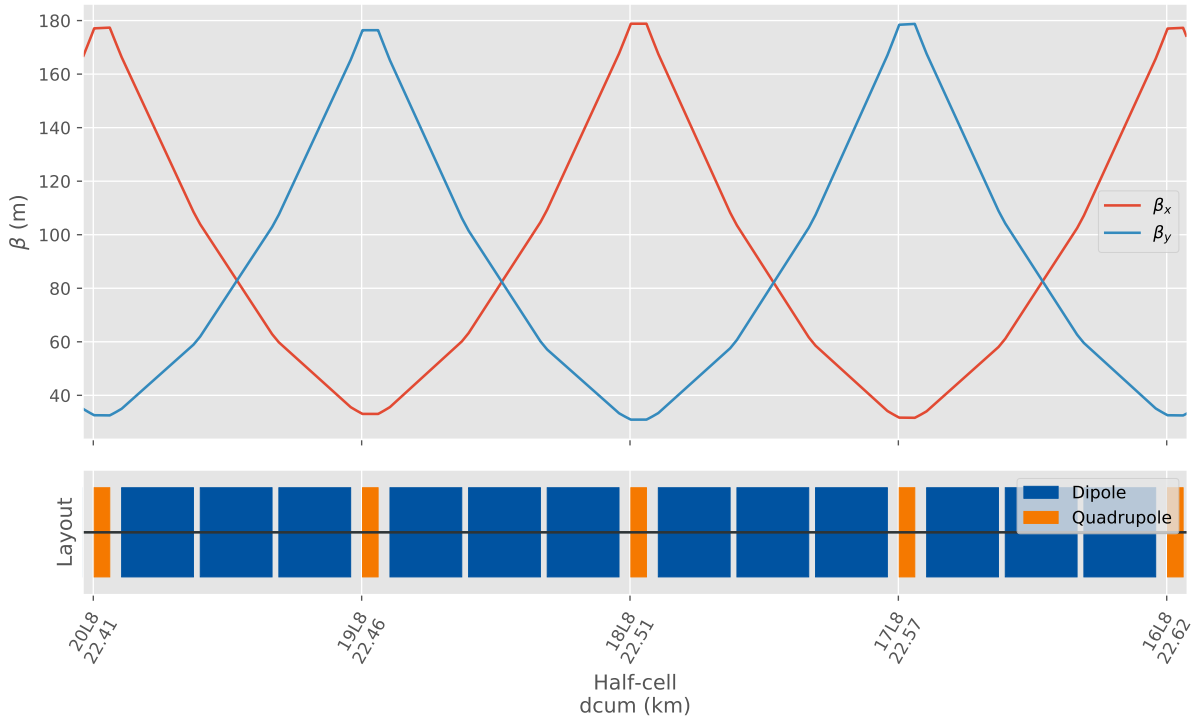

Figure 6: β function for two LHC arc FODO cells. Quadrupole magnets in the half cells 20L8, 18L8 and 16L8 are focusing, whereas in the half-cells 19L8 and 17L8 are defocusing (in the horizontal plane). Plot generated based on 2017 beam 2 optics files for proton-proton collisions at 6.5 TeV with $\beta^* = 30\ cm$ [17].

Starting from the 12$^{\text{th}}$ half-cell of an IR until the 12$^{\text{th}}$ half-cell of the next IR an arc section is placed [6]. Every two half-cells of an arc section constitute so called FODO cell, where the main quadrupole (MQ) and main bending magnets (denoted as MBA, MBB) are periodically arranged. That structure is illustrated in Figure 7. The LHC arc FODO cell consists of: F – focusing quadrupole (MQ), O – three deflection magnets (MBA, MBB, MBA), D – defocusing quadrupole (rotated MQ) and O – another three deflection magnets (MBA, MBB, MBA). With this structure the stability criteria for stored beams is fulfilled. Moreover, each LHC arc cell contains additional magnets in order to correct nonlinear beam effects (e.g. chromaticity) and beam instrumentation, e.g. Beam Position Monitors (BPM).

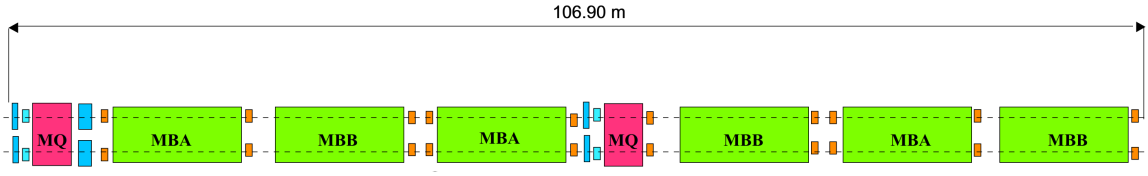

Figure 7: Scheme of a FODO arc cell [7].

2.4. Beam modes

As mentioned previously, the goal of the LHC is to collide the beams at highest energies. The LHC works in cycles. Each cycle is called a fill, and consists of the beams injection, acceleration, colliding and finally extraction. In the beginning the accelerator has to be filled with particles. This step is called injection. After the beams have been injected their energies have to be increased. This step is named acceleration. If the beams have required parameters they can be collided. At the end of each fill extraction (dump) takes place because intensity becomes too low, due to the luminosity burn-off that is described in chapter 2.6, and hence it is no efficient to operate anymore. It might happen that controlled and stable operation cannot be maintained anymore, thus protective dump is executed.

To describe and summarise particular activities conducted in the LHC, so called Beam Modes were proposed [1]. The LHC status and its beam modes are stored in the logging database (LDB).

In total 19 beam modes exist [1], however only the most important (that are a desired part of each fill) are explained below.

INJECTION – consists of three beam modes, in which the purpose is to fill the accelerator with multiple injections (maximum 144 bunches per injection from the SPS [28]) of bunch trains which were prepared in the injector complex.

RAMP – in this beam mode, after the completed injections, the beams are accelerated from the injection energy (450 GeV) to the collision energy (6.5 TeV). Usually this lasts around 20 minutes.

FLAT TOP – entering this mode suggests that intended particles energy (6.5 - 7 TeV) has been reached and the beams have designed parameters.

SQUEEZE – in this beam mode, the beta functions are changed in order to make colliding possible.

ADJUST – the final beam adjustments are performed and the particles start to collide.

STABLE BEAMS – when stable conditions for collisions are achieved, this mode is set – beams are continuously collided, luminosity is being produced, hence collision data are acquired by the experiments.

BEAM DUMP – extraction of the beams from the accelerator is performed.

2.5. Radiation effects on electronics

During the operation of the accelerator small amounts of particles are lost, which create a prompt radiation field along the LHC. The prompt radiation causes accelerated ageing of the exposed elements, e.g. electronics, which results not only in a reduced lifetime. It also may provoke single-event effects (that are explained in this section) which might lead to beam dumps. Therefore the knowledge of the

dose distribution is important for choosing the correct position for the elements in order to optimise their lifespan [29] and reduce interruptions in the accelerator operation caused by electronics failures. To completely express the purpose of the research some radiation effects will be explained.

Three fundamental damage mechanisms, mentioned below, take places in the presence of various radiation fields (e.g. protons, electrons, photons, neutrons etc.).

Displacement damages – The non-ionising energy loss in a material by high energy particles (e.g. neutrons), can change arrangement of the atoms in the crystal lattice. Therefore the number of defects can be increased, resulting in a reduction of the material's robustness (accelerated ageing) or alteration of electrical proprieties. Figure 8 illustrates the idea of the hole creation. An energetic particle interacts with the nuclei of the atom in the lattice and creates damage of the lattice structure by relocation of the atom.

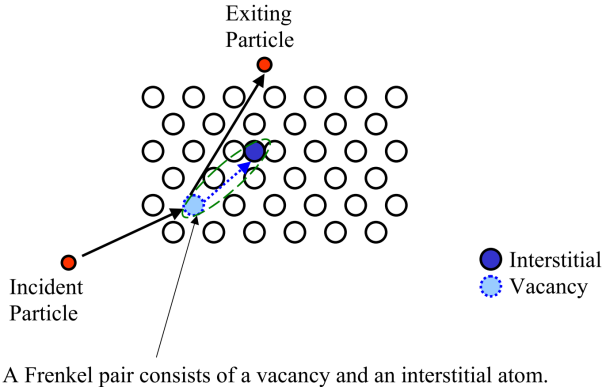

Figure 8: Illustration of a displacement damage [10].

Cumulative ionisation – when a photon or charged particle penetrates a medium it interacts with electrons of the atoms, resulting in the ionisation, i.e. electron - hole pairs creation. This affects conductive properties, e.g. threshold voltage shifts or leakages [8]. A quantity that is used to describe cumulative ionisation effect is called the total ionising dose (TID).

Single-event effects (SEEs) – affect mostly digital devices where information is sent/stored as bits. When an ionising particle goes through a semi-conductor (for example in a transistor), due to ionisation, its state can be modified. Despite the fact that SEE cause is the same as for cumulative ionisation, the effect is different. Here, a single particle is capable of creating an observable effect in the device [8]. SEE can be hard (destructive) or soft (non-destructive).

2.6. Beam losses mechanisms

Always when a particle leaves its stable trajectory it will be lost on either collimator or the beam screen. The causes of particles leaving the stable orbit are numerous. It is expected, that some of the parameters and settings of the accelerator have direct impacts on the losses, e.g. a collimator opening determines losses in the IR7. Generally, local dose levels scale with local losses along the LHC [29].

There are many beam loss mechanisms that are being observed in the LHC, but in this thesis two are considered:

Beam-residual gas interactions – The vacuum in the LHC is not perfect and some residual gas molecules are present in the beam pipes. Some particles in the beams interact with these molecules,

resulting in continuous loss of particles along the accelerator. It is expected that this losses scale linearly with integrated intensity and residual gas density [29].

Luminosity burn-off – During collisions particles that undergo interactions might influence a momentum transfer to the transverse plane. Collision debris, that do not conform with LHC requirements, is lost downstream of the experiments causing locally high radiation levels. In general they should not be observed in the arc sections. These levels scale with the integrated luminosity of the experiment [29].

In order to minimise the losses at the beam screen collimators are used. They deliberately intercept particle that do not have acceptable longitudinal or transverse oscillation amplitudes. As a consequence particles are then removed in the collimators, that are design to withstand high beam losses, to prevent them to have been lost in the more sensitive parts of the LHC.

In the arc sections losses due to beam-residual gas interactions, resulting in the impacting of beam's particles on the beam screen, are the main contributor to the dose. The residual gas pressure is assumed to be constant over an arc.

2.7. Beam loss monitoring

The energy deposition, caused by beam losses, leads to an local increase of the temperature. If the temperature increase in a super conducting element exceeds the critical temperature the superconductor transitions to a normal conductor (it quenches). Therefore, the resistance appears. In order to protect the accelerator, the beam dump is then triggered. The main aim of the BLM system is to prevent damage of machine components and magnet quenches due to beam losses [11], but it is also used as a tool to study causes of the losses [11].

It is based on radiation detectors, in most cases ionisation chambers filled with nitrogen gas, that detect particle showers caused by the beam losses. Exemplary beam loss monitors (BLM) located in the LHC tunnel are shown in Figure 9. The system integrates signal over different time intervals (running sums) and compares with a threshold. If it is exceeded, to ensure safety of the accelerator, a beam dump is initiated and the beams are safely extracted and dumped on the absorber blocks.

Although BLMs had been placed along the whole of the LHC, due to the scope of the thesis, only those at the arc sections are presented. The installation pattern of the BLMs follows the periodic structure of FODO cells in the arcs – each half-cell contains 6 BLMs: 4 (2 for each side) are located at quadrupole magnets (MQ) in the beam plane, and remaining 2 are mounted on top of the pipe close to the interconnection of the dipole magnets (MB). Ionisation chambers, that monitor dose rate nearby the MQs are called *BLMQI*. Those installed on top of the interconnections between MB are named *BLMBI* with the beam number 0. Schematic locations and naming are displayed in Figure 10.

[3] an actual arc BLM configuration is different – only two BLMs are installed in the vicinity of quadrupole magnet at one side

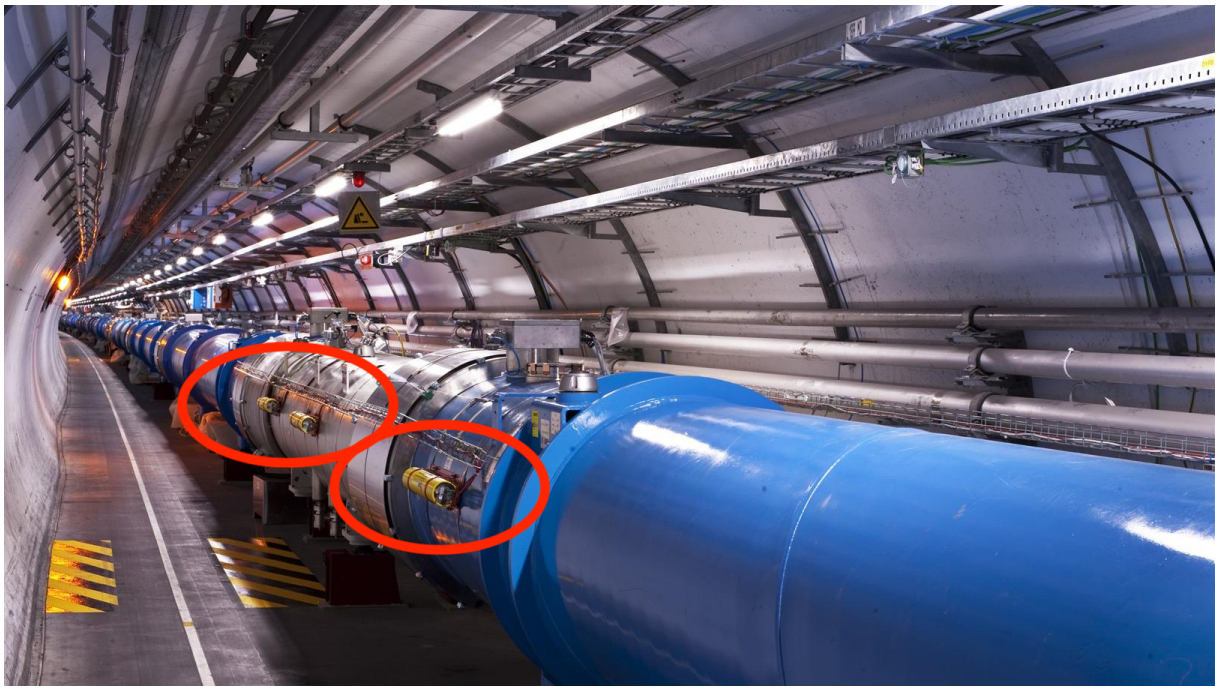

Figure 9: Beam loss monitors (inside red circles) along the LHC[3](modified [5]).

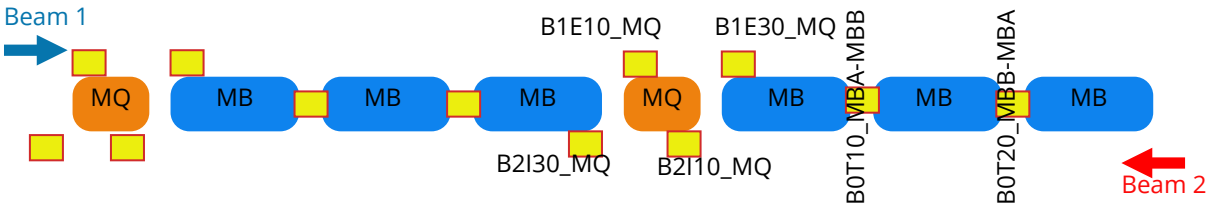

Figure 10: Positioning and naming of the BLMs in the LHC arcs' FODO cells. Letter E (exterior) or I (interior) after a beam number denotes if the beam is outside (E) or inside (I) the LHC circle. For example BLM with the name *BLMQI.22L3.B1I10_MQ* is located at the quadrupole magnet in 22nd half-cell, in the arc section 2-3, at the beam 1 side. The beam 1 in this arc section is closer to the the geometric centre of the LHC than beam 2.

Main focus is emphasised on the total ionising dose (TID) which is used to evaluate cumulative effects. Therefore, high resolution of data is not important, and in order to optimise data handling the longest running sum is considered [4].

[4]LOSS_RS12 – running sum over 83.89 s

3. Methodology and developed tools

3.1. Intensity calculations

In case of stable beam propagation through the arcs, it is expected that the majority of losses is causes by interactions of the beam with the residual gas. In this conditions, according to chapter 2.6, it is expected that losses scale with the beam intensity and residual gas density.

In order to compare dose levels between different periods, normalisation with the integrated intensity has to be performed. Thus the first step was to develop the tool that allows the values for requested periods to be obtained. All presented calculations are based on the total intensity, i.e. sum of the intensities for both beams[1] measured by the beam current transformer(s) (BCTs) located around IP4.

Some special names were introduced to avoid misunderstanding:

Beam interval: A continuous period of time, where at least one of the beam circulates in the LHC. CERN's long-term logging database (LDB) contains beam present flags[2]. The interval is not necessarily one LHC "fill". An example of beam interval is provided in Figure 11.

Beam subinterval: The continuous period of time during a beam interval in which beam mode[3] had been constant. The idea of beam subintervals is highlighted in Figure 13.

[1] LDB's variables: LHC.BCTDC.A6R4.B1:BEAM_INTENSITY and LHC.BCTDC.A6R4.B2:BEAM_INTENSITY
[2] LDB's variables: HX:SMP1_PRESENT and HX:SMP2_PRESENT
[3] LDB's variable: HX:BMODE

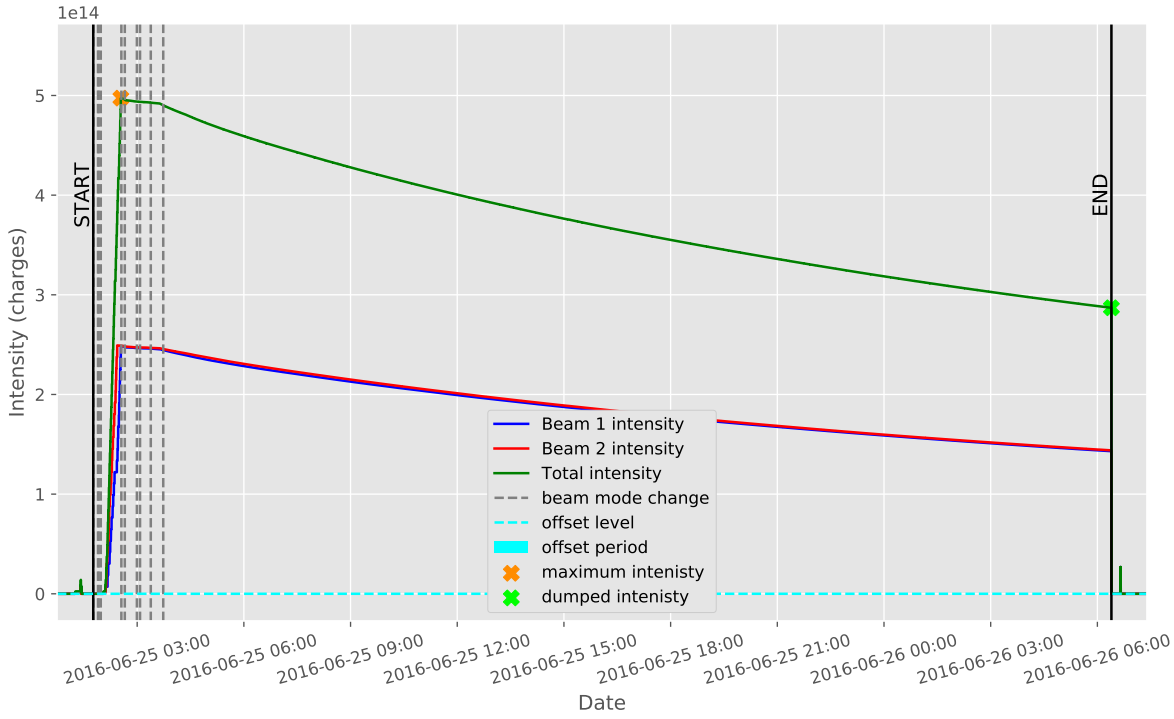

Figure 11: Concept of the beam interval with marked beam mode changes, maximum and dumped intensity. Figure 13 displays the beginning of the beam interval where the offset period and the beam mode changes are visible.

Figure 12 represents the scheme of the intensity calculation. As a first step, based on the beam present flags, beam intervals are created. In order to avoid contributions of a beam-not-present baseline the data is offset corrected on a fill-by-fill basis and then integrated. Finally, beam intervals are saved to the database, which will be presented in chapter 3.3

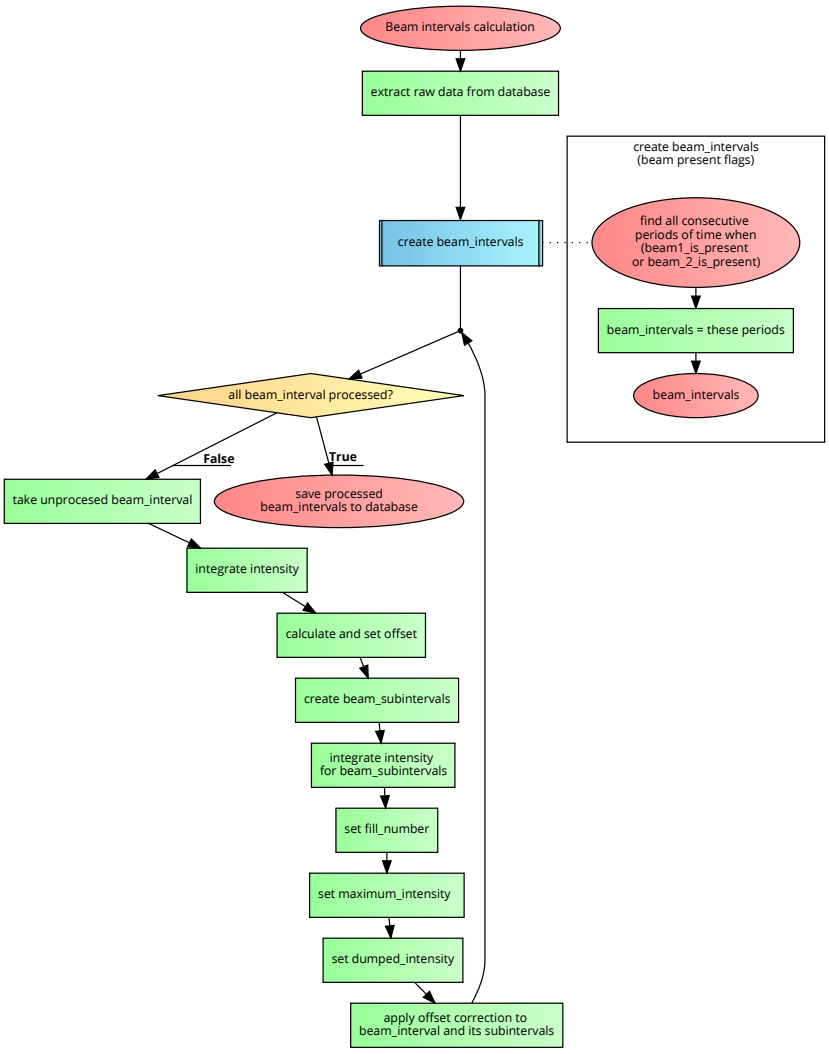

Figure 12: Scheme of the beam intervals calculation.

3.1.1. Beam subintervals

For every change of a beam mode, a new beam subinterval is created. Figure 13 shows the beginning of the beam interval, which has been presented in Figure 11. The scheme of the calculation is shown in Figure 14.

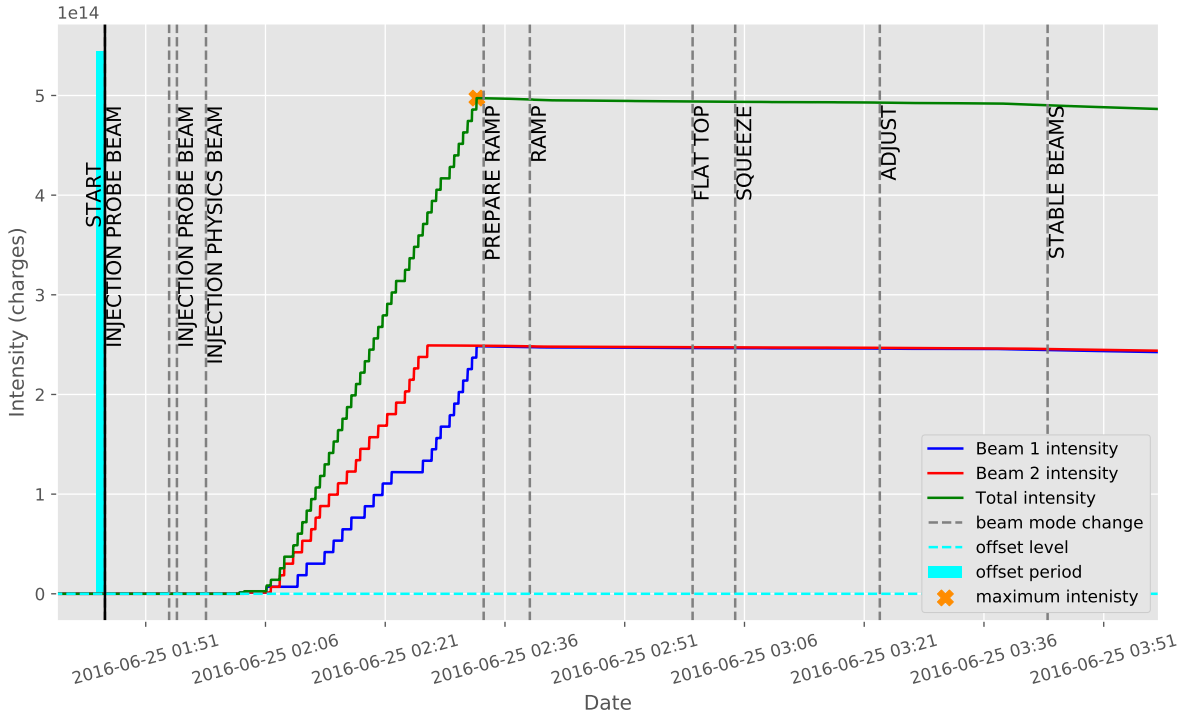

Figure 13: Concept of the beam subintervals for the beam interval presented in Figure 11. Beam mode changes are marked with grey dashed lines (or black solid for boundary ones). Each subinterval is a period with a constant beam mode.

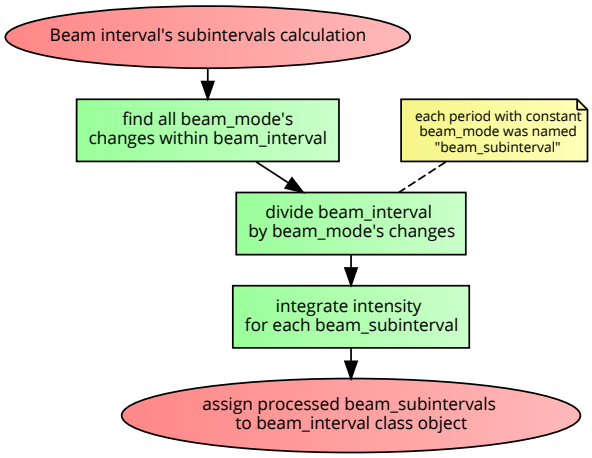

Figure 14: Scheme of the beam subintervals calculation.

3.1.2. Integration of the intensity

For the integration of the intensity for each of the beam intervals and the subintervals over time the trapezoidal rule is used. The result of the integration is called *integrated intensity* and has a unit of ps, which is proton-second (charge×time).

3.1.3. Offset removal

As the consequence of electronics imperfections even without the beam in the LHC the intensity readouts are not equal to zero. That signal can be considered as a beam-not-present baseline, hence the offset removal is performed. Its value is calculated as a mean value of the total intensity in the period that lasts between 65 s and 5 s before each interval starts. After all variables have been calculated the offset removal is performed i.e. from maximum and dumped intensity the offset value is subtracted, whereas for integrated intensities (for both beam intervals and subintervals) the offset value is multiplied by integrated period duration, then subtracted. If any of the results is negative the offset is set to 0 because it is not physical - only positively charged particles in the determined directions are accelerated. Negative intensity would implicate either negative charges present or wrong circulating direction. This can only happen when the signal to noise ratio is very low during a fill and then it will not contribute much to the overall numbers. Moreover, if an offset corrected integrated intensity for a whole beam interval is 0, then 0 is set to all its subintervals.

An example of the offset period is depicted in Figure 13 (with the cyan colour).

3.1.4. Maximum intensity calculation

It is useful to estimate the number of particles injected into the accelerator because through calculations the number of particles lost on the collimators can be approximated. It is set for each of the beam intervals as a maximum intensity value within that interval. However this approach has a few limitations. First of all it is neglected that particles are lost during the injection. Second of all, the presence of the noise is ignored, which means that maximum intensity can be a peak in the noisy signal.

3.1.5. Dumped intensity calculation

Due to collisions the beam's intensity decreases and at some point it is not profitable anymore to use the beams. To provide higher luminosity, it is better to remove all particles from the machine and then reset and refill again. In addition, the LHC operation may become unstable and thus to protect equipment, extraction has to be performed. The goal of dumped intensity calculation is to estimate the intensity that had been sent to the dump blocks, i.e. not lost in the LHC. In Figure 15 the methodology is explained.

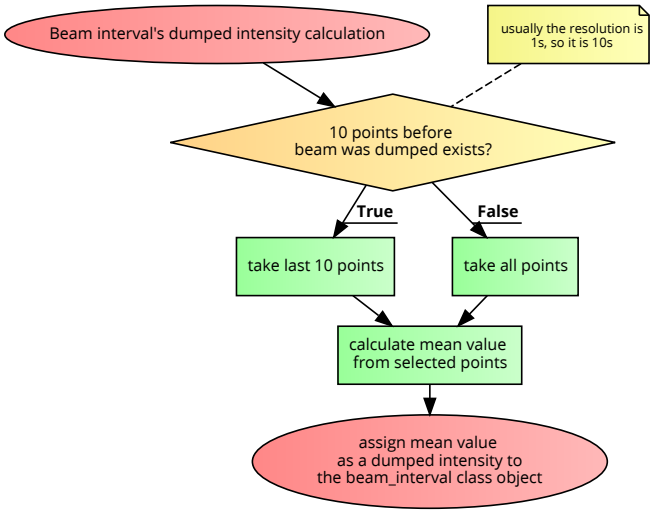

Figure 15: Scheme of the dumped intensity calculation.

3.2. Total integrated dose calculations

Based on the data from Beam Loss Monitors the integration of the dose rate over time is performed. All presented doses have unit of Grays (Gy) in nitrogen[4]. The purpose of the dose calculation is to estimate the risk related to cumulative ionisation along the LHC tunnel (described in chapter 2.5).

Special nomenclature was introduced to avoid misunderstanding:

BLM interval: The period of time for a BLM, in which at least one beam is continuously in the accelerator. The idea of the BLM interval is the same as for Beam interval, but instead of integrated intensity it stores information about integrated dose rate. The beginning and end point are taken from the Beam intervals. An example of a BLM interval is depicted in Figure 16. Each Beam interval results in n BLM interval creations, where n is the number of Beam Loss Monitors in the LHC.

BLM subinterval: The period of time during a BLM interval, in which beam mode has been constant. As previously explained the concept is similar to the beam subinterval, however instead of integrated intensity the integrated dose rate is considered. Typical BLM subintervals are shown in Figure 19.

[4] used BLMs are filled with nitrogen gas

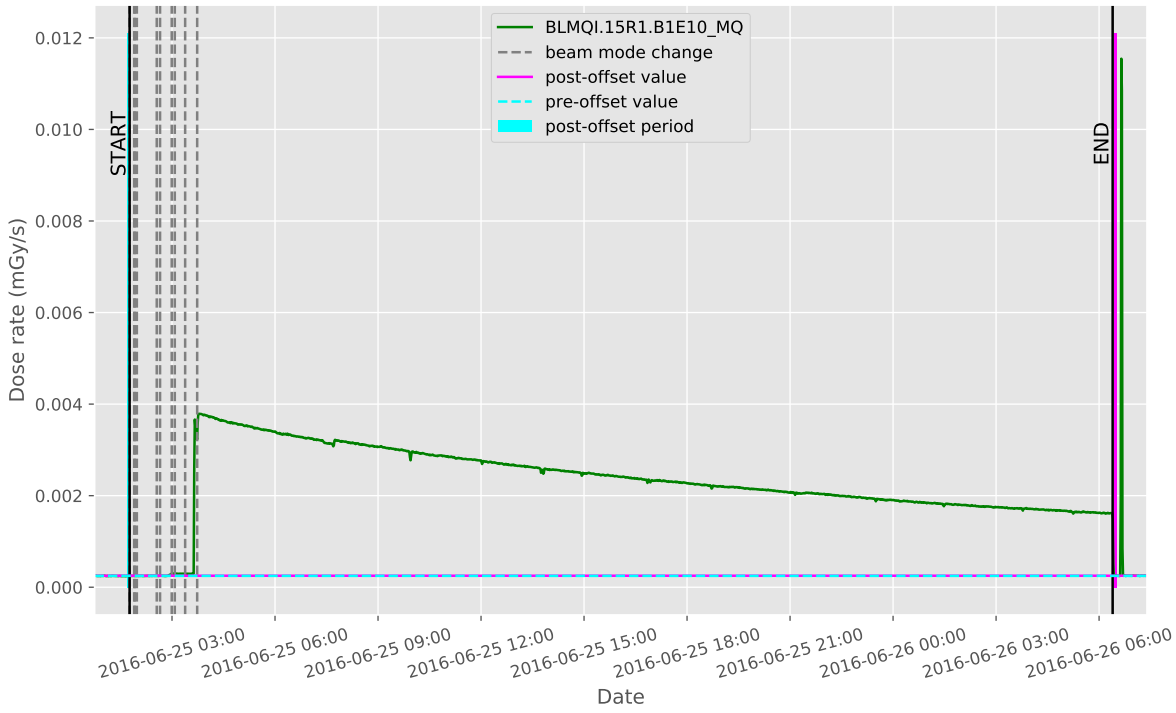

Figure 16: Concept of BLM interval with marked pre- and post-offset.

In Figure 18 the calculations scheme is presented. In the beginning the dates have to be provided, then the program reads beam intervals for the specified period (interval's start time is checked). Based on those, BLM intervals and subintervals are created – the times of both correspond to times in a beam interval and subintervals. After they have been produced, all information is calculated and assigned. It starts with two ways of the offset calculation, which are described in chapter 3.2.2. It is a vital step, especially for low dose areas, where contribution of beam-not-present baseline is not negligible. An example of such a case is depicted in Figure 17.

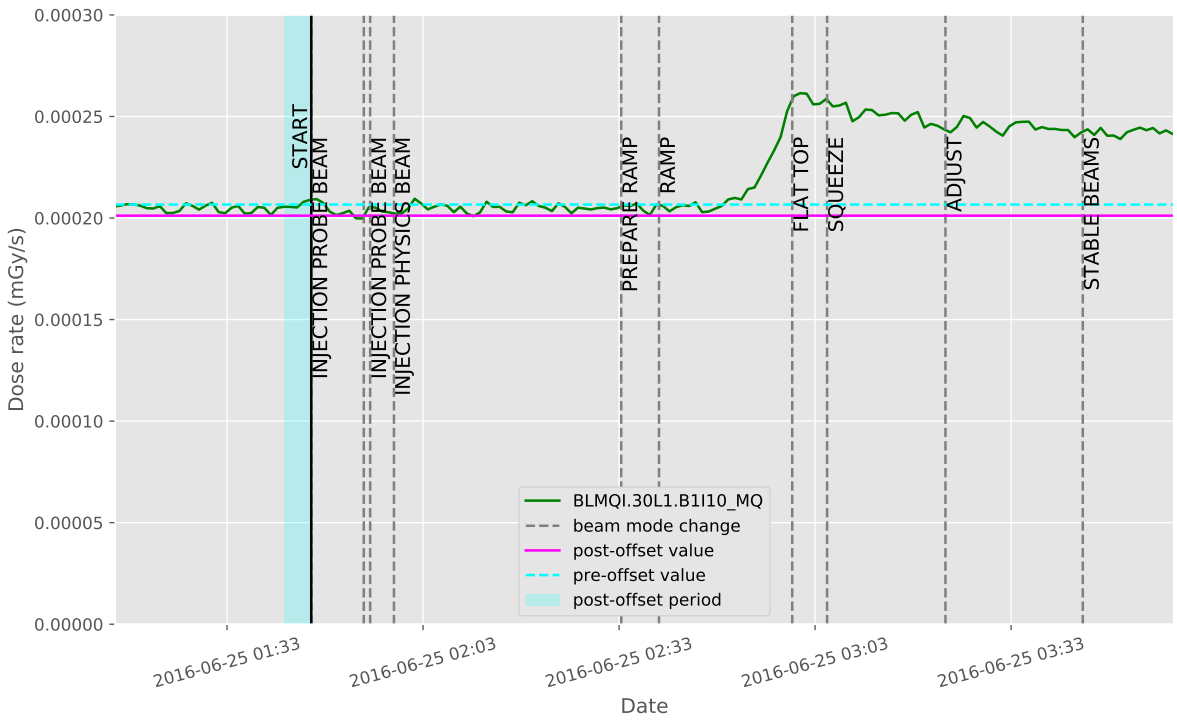

Figure 17: Illustration of the offset calculation importance for the BLM whose losses are dominated by beam-residual gas interactions. The beam-not-present baseline is 0.0002 mGy/s whereas the maximum dose rate is 0.00026 mGy/s. Without offset correction the obtained dose would be highly overestimated (at least 4 times).

By offset calculations, the influence of beam-not-present baseline on calculated total ionising dose is reduced. It may happen that due to BLM system self-testing routines the beam-not-present baseline level changes. Afterwards, the interpolation and integration is carried out (chapter 3.2.3). In the end an offset correction is applied to the results and they are saved to the database.

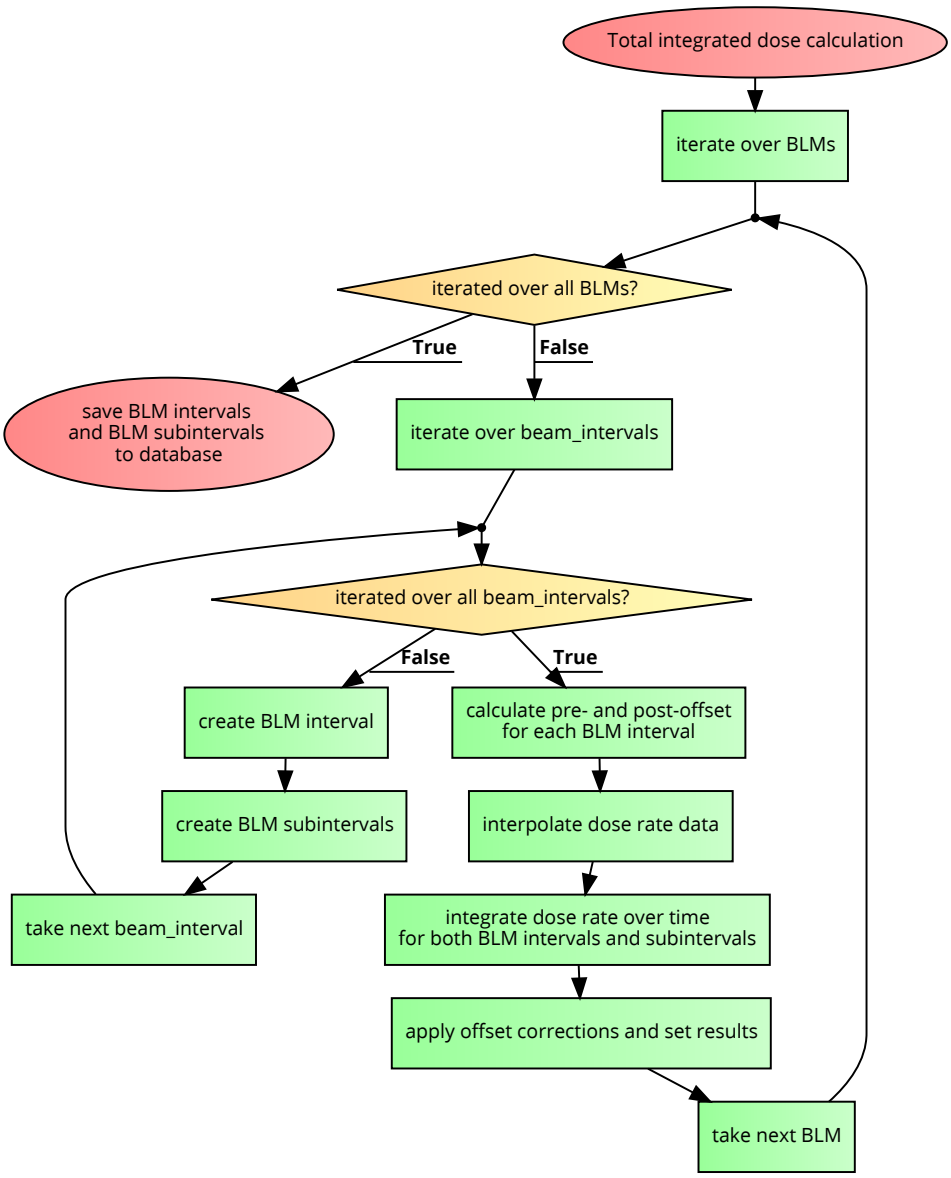

Figure 18: Scheme of the calculation for BLM intervals.

3.2.1. BLM subintervals

A detailed view of the beginning of the typical BLM interval (Figure 16) is presented in Figure 19. BLM subintervals have the same time frames as beam subintervals (Figure 13), but they store information about a different quantity – an integrated dose rate, not an integrated intensity.

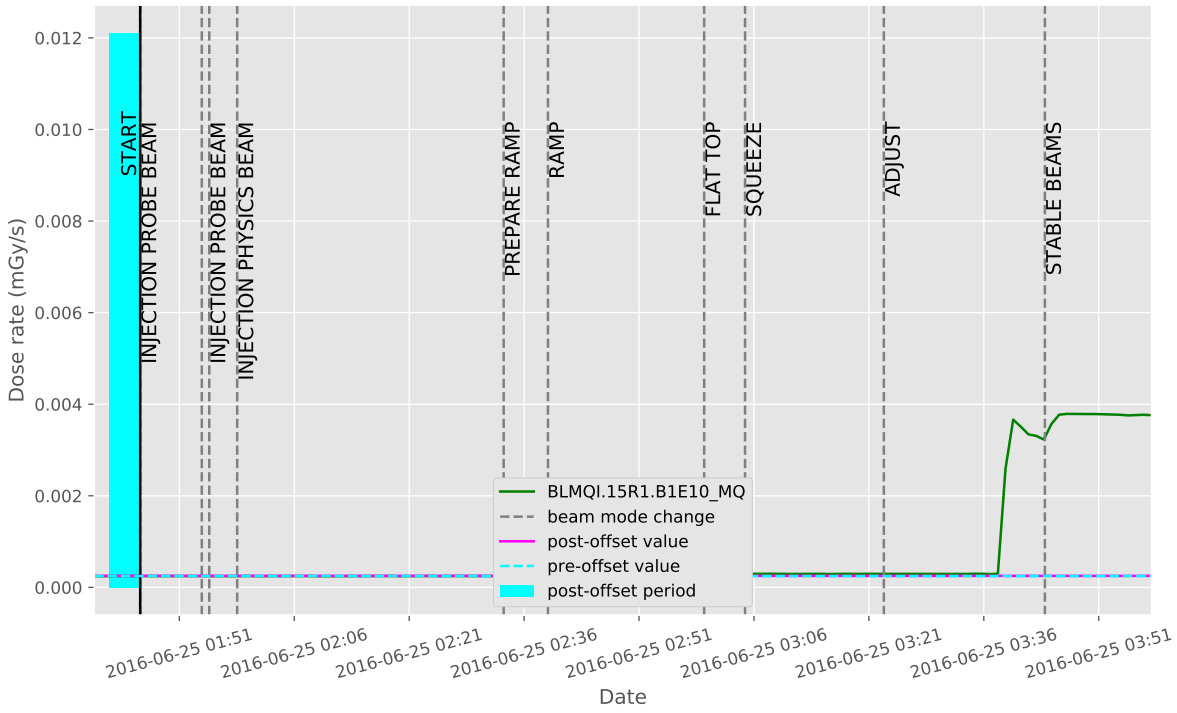

Figure 19: Concept of BLM subintervals. Each subinterval is separated with grey dashed line. As mentioned in chapter 2.4 collisions start in the ADJUST beam mode, therefore the increase of the dose rate in this period can be observed.

3.2.2. Offset removal

As mentioned above, a beam-not-present baseline dose rate level might change. To cope with it an offset calculation and correction is done. It is called the *pre-offset* calculation. The algorithm is illustrated in Figure 20. The idea is to subtract the beam-not-present baseline dose rate level from a dose rate BLM signal. An offset can be estimated as an average dose rate over specific period of time, where there was no beam. The first approach is to average over 5 minutes before a beam has been injected in the machine. Due to missing data or a vicinity of a previous BLM interval, this may not be possible. Then, the period after the BLM interval is averaged. It can happen that it is also not allowed to perform averaging for the same reasons. In such cases the *pre-offset* for a previous BLM interval is taken. Sometimes non-physical spikes exist in the readout, that are caused by DAQ system tests (an example of such a spike is), thus the comparison is carried out. If the ratio between the standard deviation and mean value exceeds 0.5, the data point with largest absolute value is removed and both average and standard deviation is computed again. If the ratio is still above 0.5 the *pre-offset* is assigned with the previous valid value.

A second way of the offset estimation is implemented in the tools. It is called *post-offset*. The only difference with respect to *pre-offset* is the inversed way of iteration over BLM intervals. It starts from the end of the time-ordered list so in the first place the data after a BLM interval ends are taken. If there is a problem (the same as for *pre-offset*) then the data before BLM interval's start is used. Since the reversed order of iteration is applied, in case the second way fails, the *post-offset* of the following (in the time domain) BLM interval is adopted.

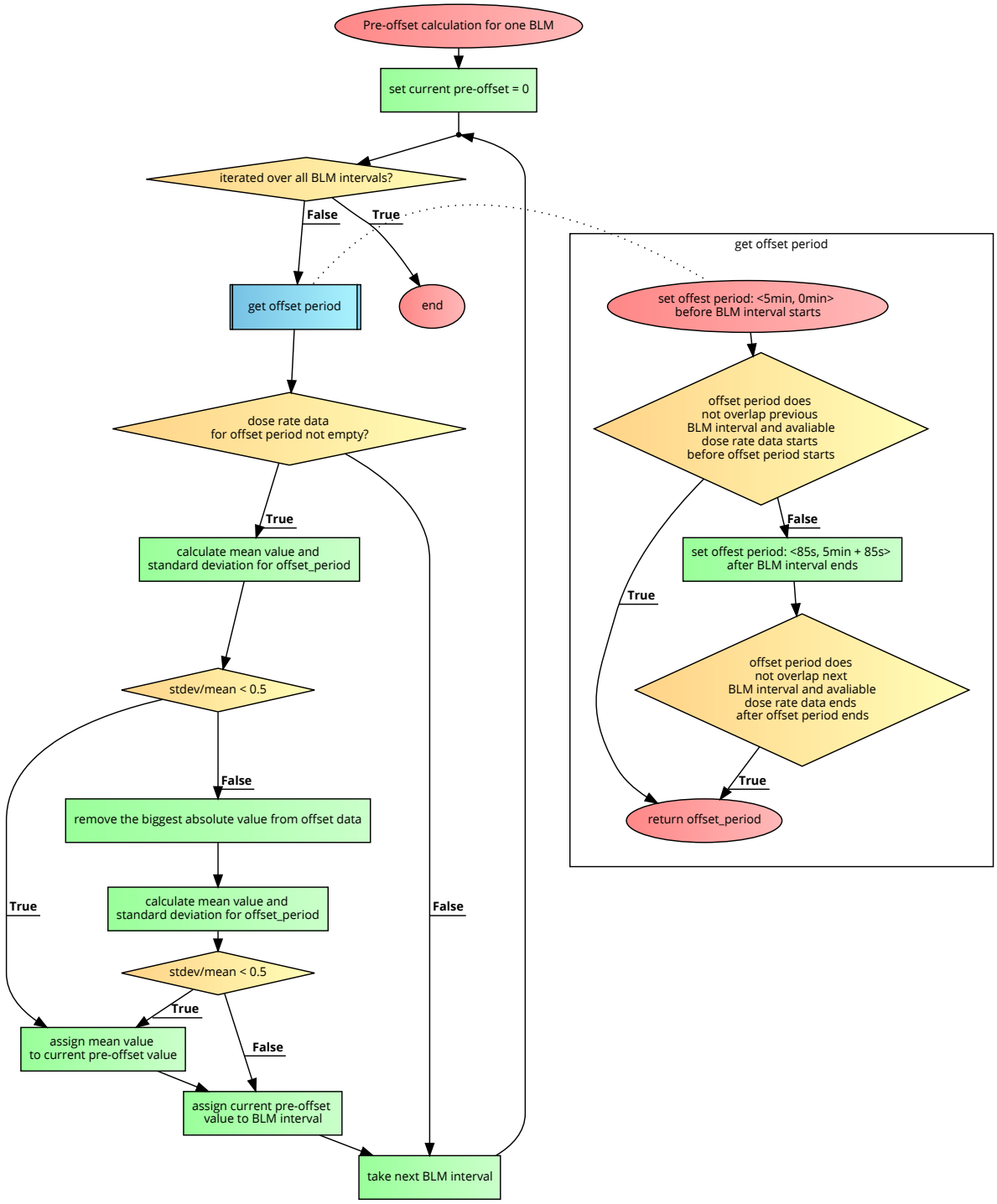

Figure 20: Scheme of the *pre-offset* calculation for BLM intervals.

3.2.3. Integration of the dose rate

Before the integration of the dose rate data the linear interpolation is performed (only for start/end times of BLM subintervals) in order to cope with low resolution of the averaged BLM data. This approach ensures that for each BLM subinterval period, data contains at least two points – for the beginning and for the end of a subinterval. The integration is based, as previously, on the trapezoidal rule.

3.3. Database

In order to speed up the calculations, increase flexibility and simplify maintenance, a dedicated *PostgreSQL* based database server has been set up to allow storage of both raw and processed data. During calculations object-relational mapping, implemented by *SQLAlchemy* [26], is used by the tools described previously. In Figure 21 an entity relationship diagram (ERD) of the database (only part for processed data) is presented.

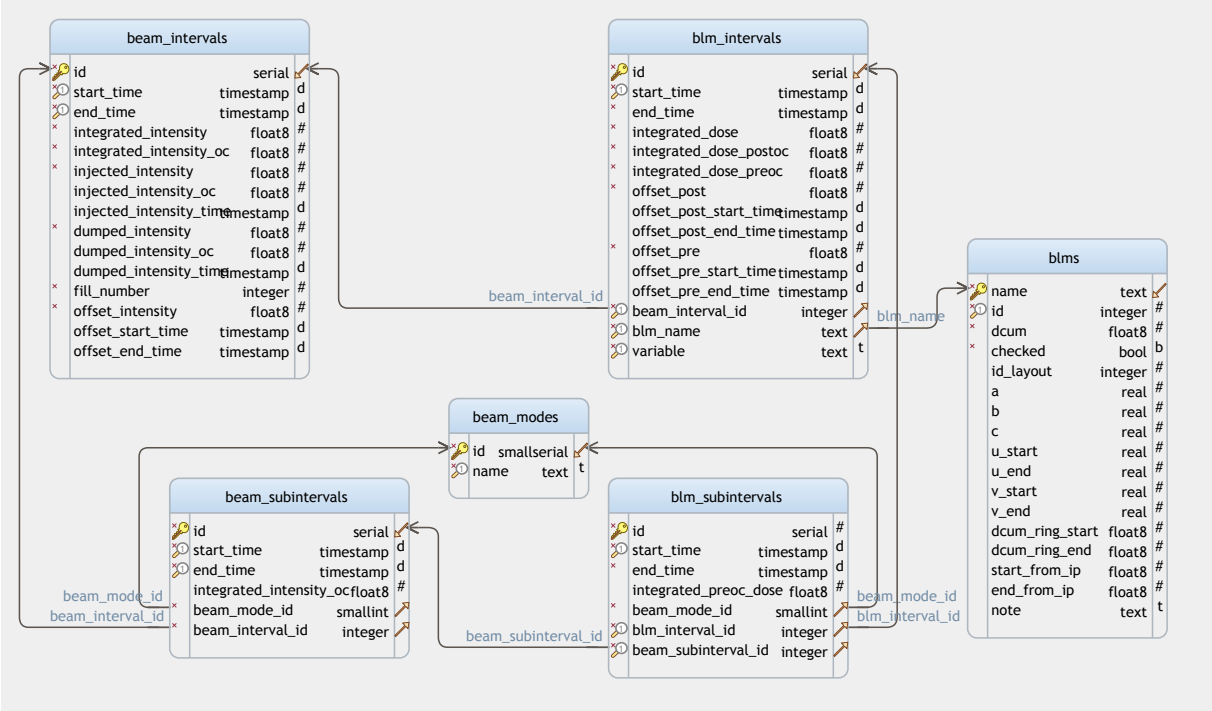

Figure 21: ERD for processed data's database

3.4. Spike and baseline analysis

In an ideal case, the observed loss pattern should reflect a periodic FODO arc structure, because BLMs are installed at the same locations in each cell . However, three conditions have to be fulfilled:

– the only significant beam loss mechanisms should be beam-residual gas interactions,

– the longitudinal residual gas distribution should be uniform,

– each FODO cell should be exactly the same (so the shielding is the same for all BLMs in the family).

Periodic loss pattern can be observed, but often it contains spikes that are not always driven by identified mechanisms. Therefore, analysis of such behaviours is needed in order to understand the causes. Sometimes an integrated dose rate for a spike exceeds the surrounding by a few orders of magnitude, which can have an impact on the lifetime and reliability of the equipment.

Following the assumption that the losses observed by BLMs at the same position in the FODO lattice shall be similar in each arc, the first step of the analysis was to divide the set of BLMs by the arc and by the BLM family (position of the BLM in the FODO cell). In total 48 subgroups can be defined. For

each one the distribution of the dose can be studied. Since the order of magnitude may vary a lot it is convenient to present a set using the boxplot representation (example one can be found in Figure 27), that is based on the three quartiles. Compared to the number of BLMs the spikes are always in the strong minority, therefore it can be said that its dose levels exceed the third quartile Q_3 which means that a maximum 25% of BLMs in the arc can be considered as a spike. However, this algorithm would always detect spikes, even though there were none, thus another filter which takes into account the dose value has to be applied. By considering as spikes only BLMs whose dose exceed Q_3 by more than $k \cdot IQR$, where IQR is the interquartile range (difference between the third and the first quartile).

The algorithm is then more robust to high dose variety in the all subgroup. The factor k was chosen to be 3, since this value provides good separation between large and non-relevant (false) spikes.

In each arc within one BLM family, the majority of BLM shows similar, very low dose level. This value is named *baseline* dose. In the algorithm the baseline dose is defined as an average dose value of all BLMs (within one arc and BLM family) that measured dose below the second quartile (median). The scheme of the calculation is depicted in Figure 24.

In the Figure 22, as an example of the algorithm application, the dose distribution in the arc without significant spikes is presented. Three main quartiles and both baseline and spike dose ranges are depicted. As a contrary, in the Figure 23 the dose distribution for the arc with spikes is shown.

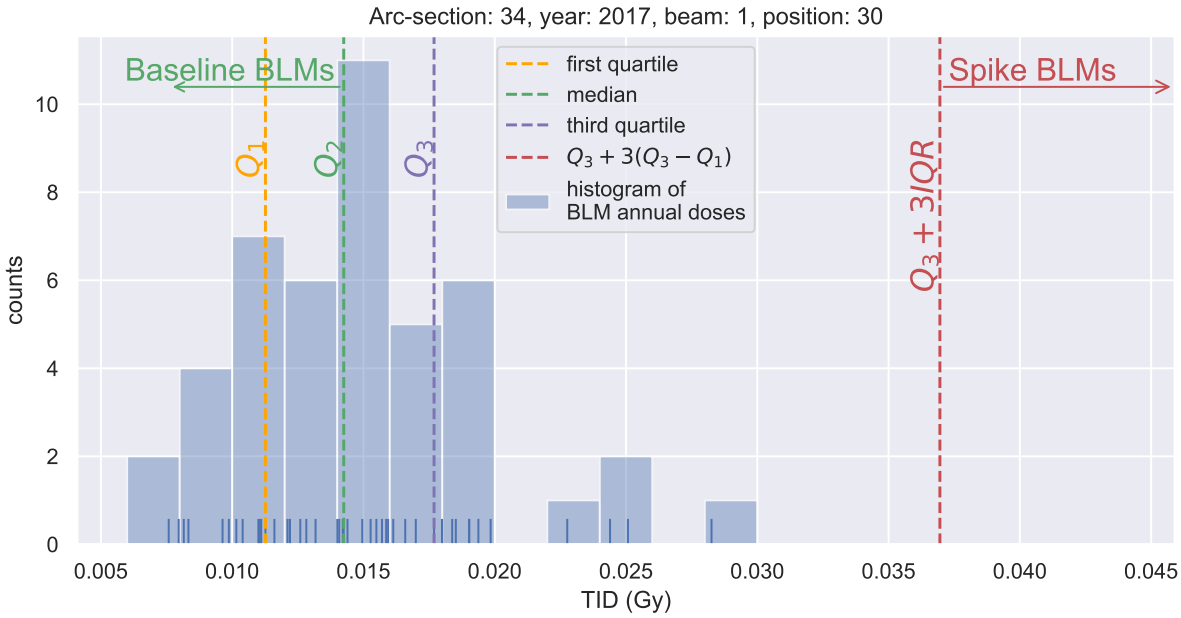

Figure 22: An example of the BLM dose distribution (histogram) with marked three quartiles and both baseline and spikes ranges. Only beam 1 BLMs at position 30 in the arc section 34 considered. In 2017 no significant spikes detected in this arc.

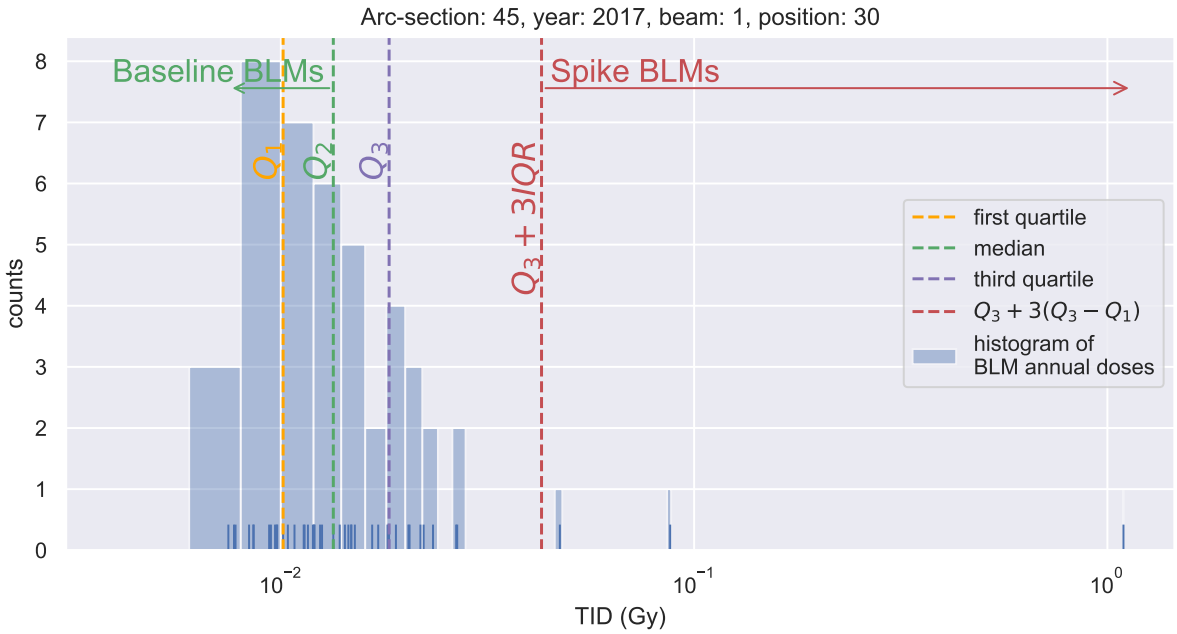

Figure 23: An example of the BLM dose distribution (histogram) with marked three quartiles and both baseline and spikes ranges. Only beam 1 BLMs at position 30 in the arc section 45 considered. In 2017 3 spikes were detected in this arc, thus semi-log representation was used.

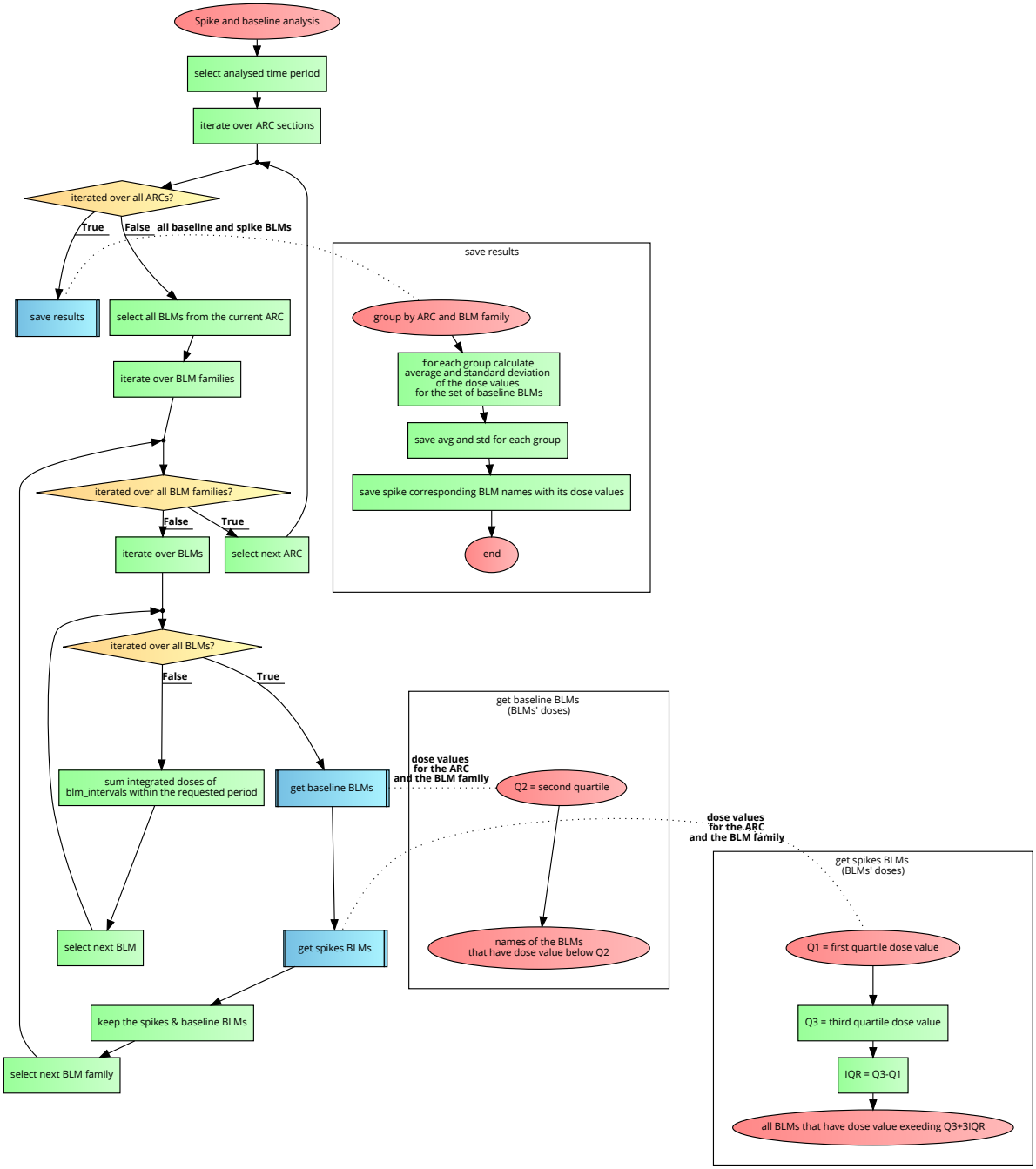

Figure 24: Scheme of the spike and baseline calculation.

The first step of the spike analysis was to determine if a spike was caused by collisions or if it was present regardless of collisions. Thus, the investigation of the dose evolution over the integrated intensity was performed. Integrated intensity was always split into integrated intensity during collision (*ADJUST* and *STABLE BEAMS*) and non-collision (the other) beam modes. The evolution is then compared to the baseline behaviour, accordingly with the arc and the BLM family. If a spike is collision driven, its evolution over the integrated intensity during non-collision beam modes will be similar to baseline behaviour for that modes. Therefore, if a spike is not caused by an experiment, the discrepancy in the evolution with respect to the baseline will be observed for both collision and non-collision modes.

3.5. Automation server

With the described tools a structured monitoring of the dose distributions is possible for the first time. Dose levels are provided on a daily basis to stay up-to-date with the LHC operation.

Jeninks is an automation server, which was set up to perform whole data processing automatically. Every day both dose rate and intensity data are downloaded and processed. Results are then saved to the database, which provides data to other clients.

Grafana is a web based data visualisation tool, that provides easy integration with databases. The server had been configured to provide access to both integrated intensity and integrated dose rate values. It gives an overview of beam mode contribution and evolution over a requested period. Integrated dose rate results can be filtered by multiple criteria, e.g. half-cell(s), beam mode(s) or BLM type(s).

Daily reports are daily created and distributed documents, that contain information about integrated dose rate levels at each IR and at each arc section. Additionally, it provides a summary of the current operation – integrated intensity with division into main beam modes, successfully injected and lost protons. Moreover, for every LHC section 10 BLMs with the highest dose levels are chosen and then compared with the rankings position one week before that time. It should be pointed out that the reports are being actively used by the MCWG.

4. Results

Following chapter 2.6, in the LHC arc sections, where each cell is a FODO lattice, the dominating loss mechanism is the interaction of the beam with residual gas molecules. Therefore it is expected that in the arcs dose levels scale linearly with the integrated intensity, provided that operational condition have not been changed, i.e. the accelerator settings have not been modified and residual gas presure has been constant. Each change could possibly impact the arc loss pattern.

The results section is split into two main sections. Firstly the integrated intensities for different years will be presented. They will be used for the scaling of the dose measurements, thus all the doses can be later scaled and compared. The second part will concern obtained dose values, therefore the behaviour in the arcs will be discussed, with the main focus on prompt dose baselines (from now on called baseline) and spikes evolution.

The presented data sets cover most of the LHC Run 2 which spanned 4 years – 2015-2018. To ensure comparable conditions, only periods with the proton-proton operation were chosen. The LHC schedules for these periods can be found in the Appendix (Figures 43, 44, 45 and 46). Year 2018 has been considered until Technical Stop 1 (18.06.2018).

4.1. Integrated intensity for different years

Integration of the intensity was performed using the developed software that has been described in chapter 3.1. In Table 1 both integrated intensity and duration of the active operation are presented. The contribution of the selected beam modes are highlighted. It is assumed that the intensity is split equally between the two beams, which is one of the aims of the LHC operation, because in such a case the highest luminosity is achievable.

The 2015 year was the first one after Long Shutdown 1 (LS1), therefore non-physics injections were performed. It implied that total integrated intensity and contribution of the stable beams mode, was lower than in the following years, whereas contribution of the injection modes was higher. The main reason was that more time was spent in *Recommissioning with beam* and *scrubbing* than in the years 2016-2018. *Recommissioning* stage is necessary to ensure that all components of the LHC works safely and properly. The injected beam has low-intensity, that prevents damages in case of a system failure. The LHC, during the scrubbing, is filled with the high intensity and low energy (450 GeV) proton beam and is kept only in an injection beam mode. The objective of a scrubbing process is to reduce the electron-cloud effect [23], i.e. release as many trapped residual gas molecules as possible from the surface of the vacuum chamber so they do not interfere with the high energy beam [23].

In Figure 25 evolution of the integrated intensity over time is depicted. Collision modes (STABLE BEAM and ADJUST) and injection modes were highlighted.

Table 1: Integrated intensities and durations for different years with contribution of the selected beam modes.

	2015	2016	2017	2018
start date	05.04. 00:00	29.03. 00:00	01.05. 00:00	28.03. 00:00
end date	10.11. 00:00	01.11. 00:00	11.11. 00:00	19.06. 00:00
Total integrated intensity (ps)	**7.16E+20**	**2.60E+21**	**2.51E+21**	**1.06E+21**
Injection modes (%)	22.1	4.6	10.3	8.3
Ramp modes (%)	7.4	6.5	7.1	7.2
Squeeze mode (%)	2.7	2.9	2.2	2.4
Adjust mode (%)	2.5	3.0	2.4	1.8
Stable beams mode (%)	63.9	84.1	78.2	80.9
Total duration (h)	2633	3276	2975	1314
Injection modes (%)	46.5	21.7	24.6	25.4
Ramp modes (%)	11.6	9.9	7.5	9.9
Squeeze mode (%)	7.0	6.2	3.0	5.5
Adjust mode (%)	5.8	9.4	8.0	8.2
Stable beams mode (%)	26.3	54.2	55.8	51.0

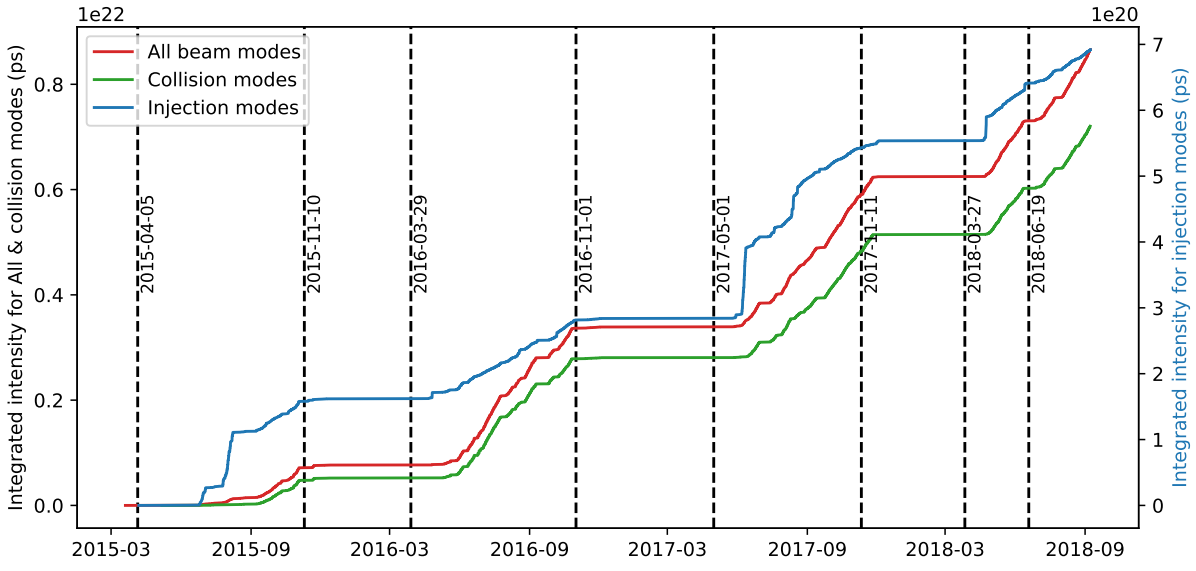

Figure 25: Evolution of the integrated intensity over the years.

It can be observed, that injection modes grew the most in 2015 and 2017, which is because of the long scrubbing periods in these years. The plateaus with constant integrated intensity represent the periods without LHC operation due to technical stops or other interruptions. The total integrated intensity is dominated by the integrated intensity in the collision modes (more precisely by STABLE BEAMS beam

mode).

It was observed that some arc BLM doses do not scale with the integrated intensity, but with the integrated luminosity, i.e. they accumulate much more dose when the beams are collided. That behaviour is expected only around the experiments, but not in the arc sections, since collision debris (off momenta particles) shall be intercepted by local collimators around an experiment and in general shall not last until the arc section.

Since the luminosity is produced only during collision modes it makes more sense to compare integrated luminosity versus integrated intensity for collision modes only.

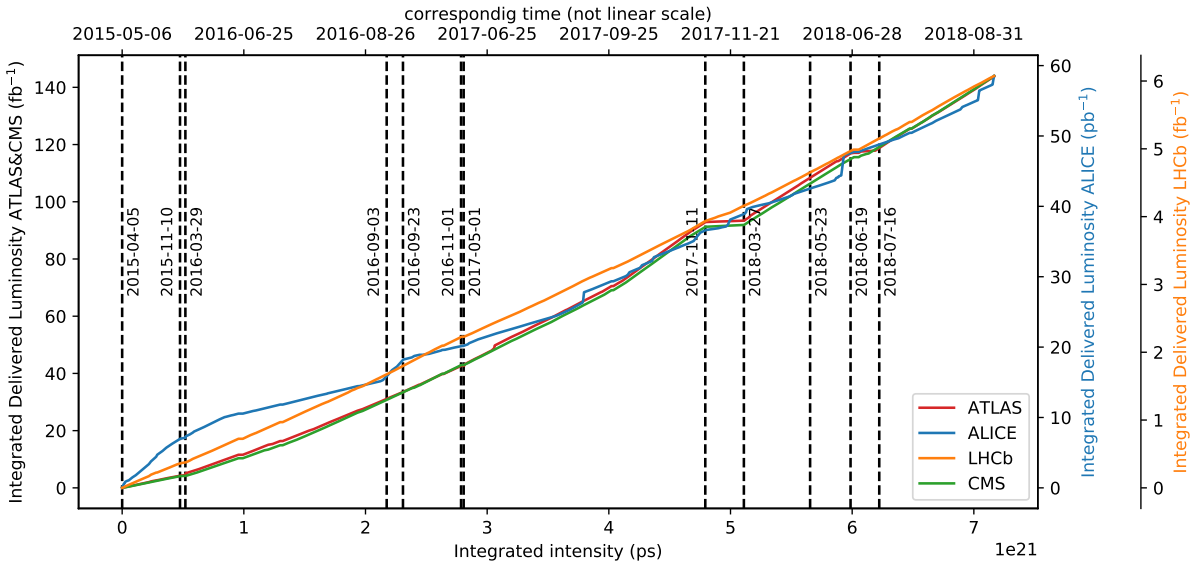

Figure 26: Evolution of the integrated delivered luminosity over the integrated intensity for collision modes only. Since LHCb and ALICE experiments produce much less luminosity, each one has its own y axis.

For the considered periods in the years 2016-2018, described in Table 1, the linear slope of the integrated luminosity over the integrated intensity for collision modes only is approximately preserved for the three experiments – ATLAS, CMS, LHCb. It is illustrated in Figure 26. For ATLAS and CMS the 2015 year had lower integrated luminosity per unit integrated intensity (mainly due to the β^* change). Further, it will be assumed that luminosity driven spikes scale with the integrated intensity for collision modes.

4.2. Dose analysis

As it has been described in chapter 2.2, the LHC consist of 8 arc sections that span between dispersion suppressor regions. Each arc starts at cell 12 of the right side of an IP and ends at the left side of the following downstream IP (with respect to beam 1). It was mentioned in chapter 2.7, that BLMs in the arcs can be split into 6 groups by their position in the periodic FODO cell (*beam 0* or *B0* refers to the Top BLMs). In the analysis all BLMs were split by an arc and a BLM family into 48 subgroups.

Obtained doses for each year were normalised with the corresponding integrated intensities, presented in Table 1 to allow a comparison of BLM doses among different years.

In the box plots Figure 27 and Figure 28 annual (for the selected periods) integrated doses are presented for the beam 1 and the positions 10 and 30 (in the beginning and after a quadrupole respectively).

This representation gives a good overview of the evolution of dose levels over the years and over the arc sections.

Each box represents integrated intensity normalised dose for all BLMs from one subgroup whose calculated doses are between the first and the third quartile (Q_1 and Q_3). In this thesis end of the lower whisker represents the BLM with the lowest normalised dose. The end of the upper whisker represents a BLM, which has the largest normalised dose, that is still within 3 IQR distance above the Q_3 ($\leq Q_3 + 3(Q_3 - Q1)$). All BLMs normalised doses that are above this value are treated as spikes. Their number is presented as a bar above each box. An example of the dose distribution with marked quartiles and both baseline and spike ranges was presented in chapter 3.4.

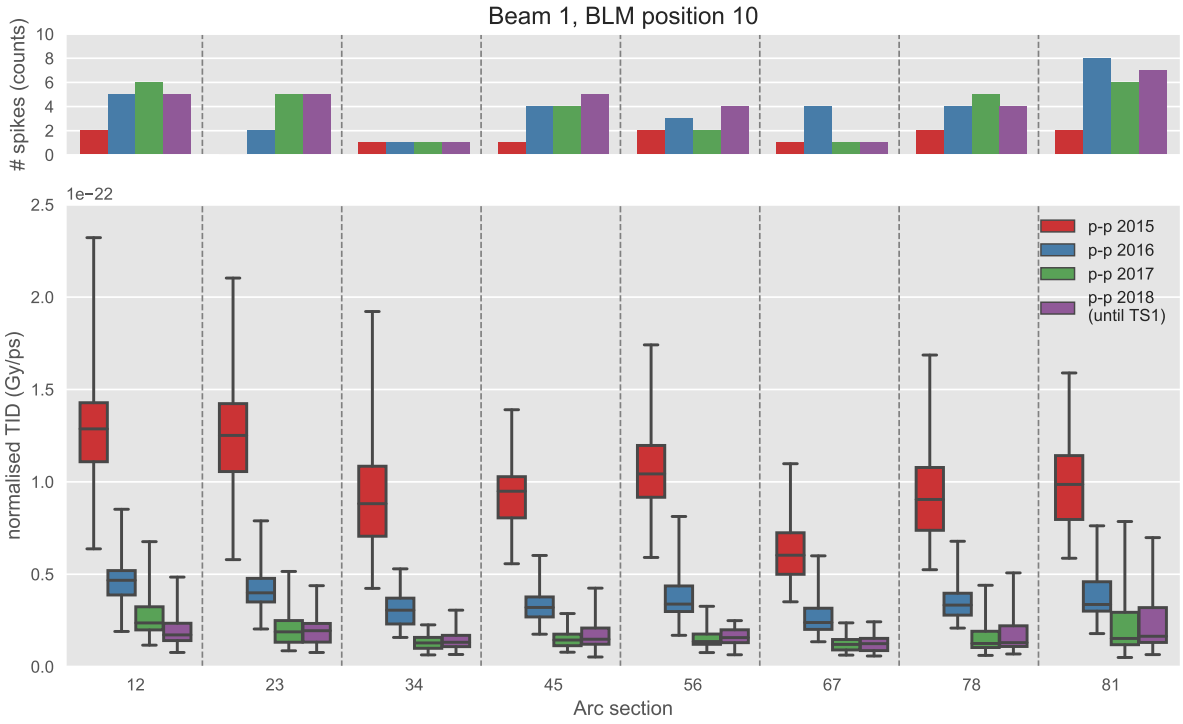

Figure 27: Box plot of the total normalised integrated dose rate for years 2015-2018. Only beam 1 BLMs with position 10 considered. Ends of the whiskers represents: the lowest BLM's normalised TID still within 3 interquartile range (IQR) of the lower quartile, and the highest datum still within 3 IQR of the upper quartile. Data above an upper whisker is treated as spikes and its counts are presented on the top of the plot.

For both beams the dose levels in position 30 were lower than in position 10, which is also visible in the simulation [12]. It can be observed that in the years 2015-2017 normalised dose levels were decreasing. In 2018, apart from the arc section 12, they slightly increased. It is possible that it because 2018's data was considered until the 19.06.2018, therefore the *Recommissioning* period could contribute more. The decrease in the normalised dose level in the arc section 12, between the year 2017 and 2018, is most likely to be caused by the 16L2 problem. That will be presented in chapter 4.2.2 and is visible in all BLM families.

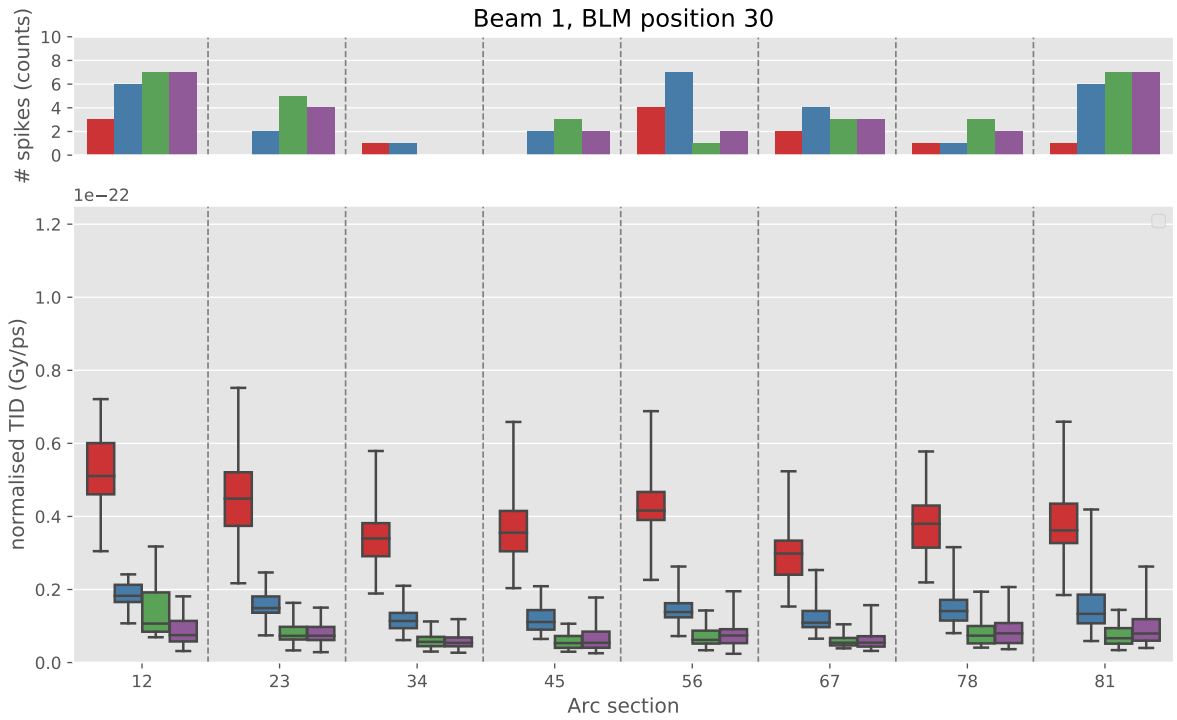

Figure 28: Box plot of the total normalised integrated dose rate for years 2015-2018. Only beam 1 BLMs with position 30 considered. Ends of the whiskers represents: the lowest BLM's normalised TID still within 3 IQR of the lower quartile, and the highest datum still within 3 IQR of the upper quartile. Data above an upper whisker is treated as spikes and its counts are presented on the top of the plot.

Box plots for Beam 2 and Top BLMs can be found in the appendix (Figures: 47, 48, 49, 50).

4.2.1. Baseline analysis

As it was mentioned in chapter 3.4 the *baseline* is the averaged dose level in one subgroup (one family of BLMs in one arc section). Averaging is performed among BLMs, whose calculated dose is below the median value for a subgroup in order to avoid inclusion of spikes. The expectation is that beam losses are determined only by beam-residual gas interactions. It is assumed that the residual gas pressure is constant in the arc, however the assumption has to be validated in the future.

For each arc and BLM family (subgroup) normalised annual baseline dose levels were calculated. The results for the beam 1 and position 10 are presented in Table 2, whereas for the other BLM families they can be found in the appendix (Tables 4, 5, 7, 8).

Table 2: Total integrated dose baseline levels for different years, normalised with integrated intensities, with the standard deviation. Only B1 and 10 position's BLMs considered.

ARC	2015	2016	2017	2018	unit
12	10.8±1.7	3.80±0.62	1.97±0.33	1.35±0.26	10^{-23} Gy/ps
23	10.0±1.9	3.24±0.67	1.34±0.29	1.37±0.29	10^{-23} Gy/ps
34	6.6±1.3	2.35±0.42	1.01±0.20	1.03±0.19	10^{-23} Gy/ps
45	7.58±0.99	2.59±0.41	1.09±0.20	1.12±0.24	10^{-23} Gy/ps
56	8.7±1.3	2.89±0.39	1.15±0.14	1.25±0.22	10^{-23} Gy/ps
67	4.76±0.84	1.93±0.32	0.90±0.19	0.88±0.19	10^{-23} Gy/ps
78	7.2±1.1	2.66±0.35	1.02±0.17	1.09±0.16	10^{-23} Gy/ps
81	8.0±1.1	2.79±0.50	1.12±0.26	1.26±0.26	10^{-23} Gy/ps

In general normalised dose levels were decreasing in the years 2015-2017. In 2018 values were similar as in 2017. Contribution of different beam modes can be found in Table 15 and Table 16. The baseline dose levels in position 30 for both beams are lower than in position 10. The same behaviour was observed in the simulations (both described in the residual gas pressure paragraph and [12]). The percentage contribution of the injection modes in the doses for BLMs at positions 30 was higher than at position 10. It refers to both beams. It has to be investigated in the future why contribution of injection modes in 2016 was lower than in the other years. One of the possible explanation is that it was because of the long scrubbing runs (performed in injection beam modes) in both 2015 and 2017. The year 2018 was not included entirely and *Recommissioning with the beam*, which also contains a lot of injections, had higher contribution to the 2018's analysed period than to the remaining years. On the other hand, it was shown [3] that for IR7 doses during injections (excluding scrubbing) were lower in 2016 than in 2017.

Evolution of the baseline over integrated intensity

The developed tools allowed the evolution of the dose over the integrated intensity to be investigated. Figure 29 depicts evolution of the baseline of all 6 BLM families for the arc 12. The behaviour is not linear over the years for all the arc sections, but in the second half of 2017 (after mid. August) and 2018 it tends to be linear. This change may imply that the residual gas pressure stabilised, and hence the level of beam losses to due to beam-residual gas interaction had been constant.

The plots for the different arcs are attached in the appendix (Figures 51, 52, 53, 54, 55, 56, 57).

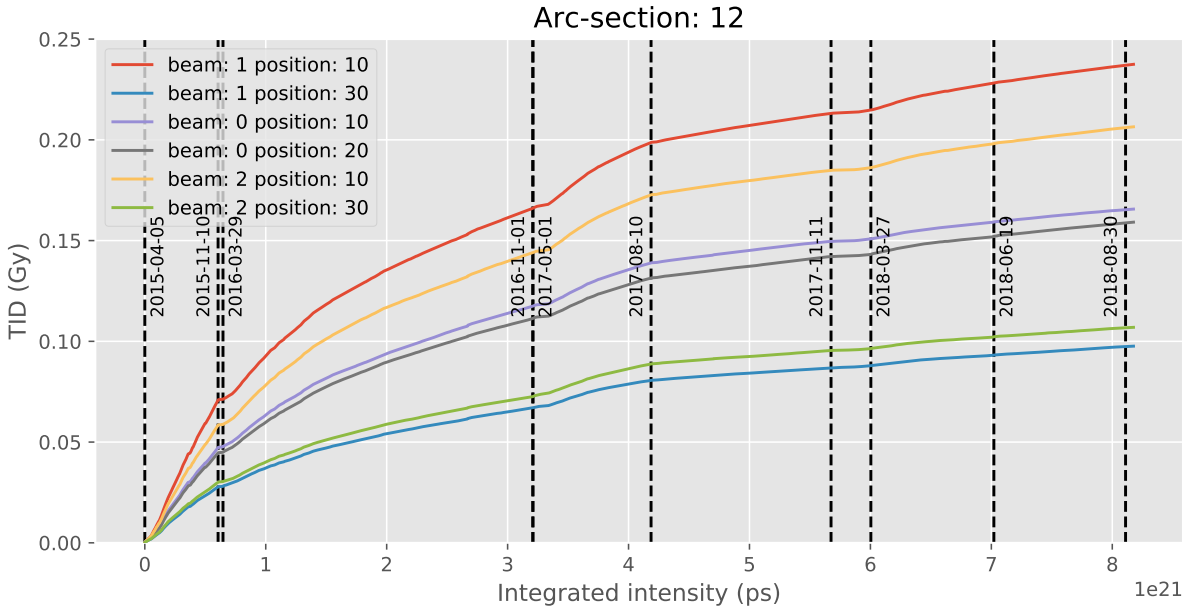

Figure 29: Evolution of the prompt dose baselines over integrated intensity for arc12 for all beam modes. Each BLM family is plotted separately.

Implication on the residual gas density

Thanks to the FLUKA simulation results[1] (Table 17) it was possible to obtain estimations of the residual gas density in the LHC arc sections. For the input conditions[2] the simulation gives doses levels normalised with the integrated intensity and residual gas density at the BLM positions in the FODO cell. By choosing such a residual gas density that minimises the difference between measurements from the BLMs and the scaled simulation, its value can be estimated. The simulation is based on a few assumptions, like constant both transverse and longitudinal residual gas profiles or symmetry in the both beams, that have to be verified in the future.

[1] provided by Cristina Bahamonde Castro, Rubén García Alía and Anton Lechner (CERN, EN-STI).

[2] ARC section length = 1267 m, cross section for the $p - H_2$ interaction = $38.4 \cdot 10^{-27}$ cm^2, revolution frequency = 11245 s^{-1}

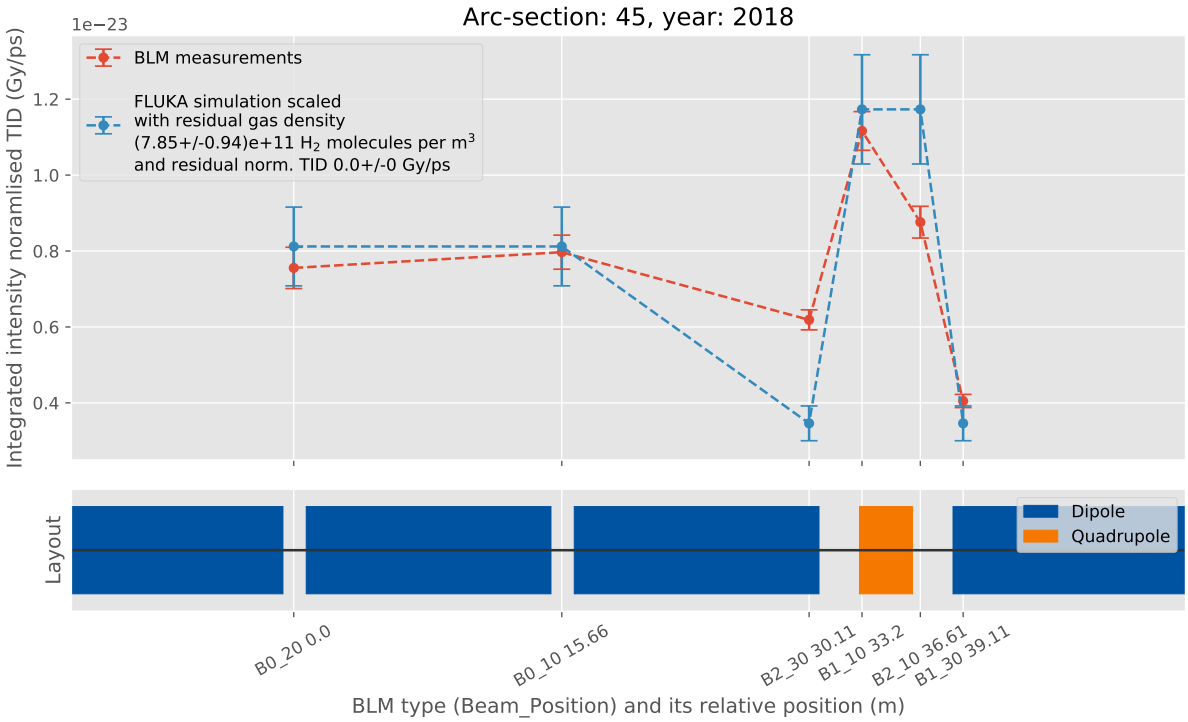

Figure 30: An example of the comparison between BLM measurements and the FLUKA simulation for the FODO cell. For the simulation scaling residual gas density in arc 45 in 2018 was used. Moreover, it is assumed that residual dose is 0.

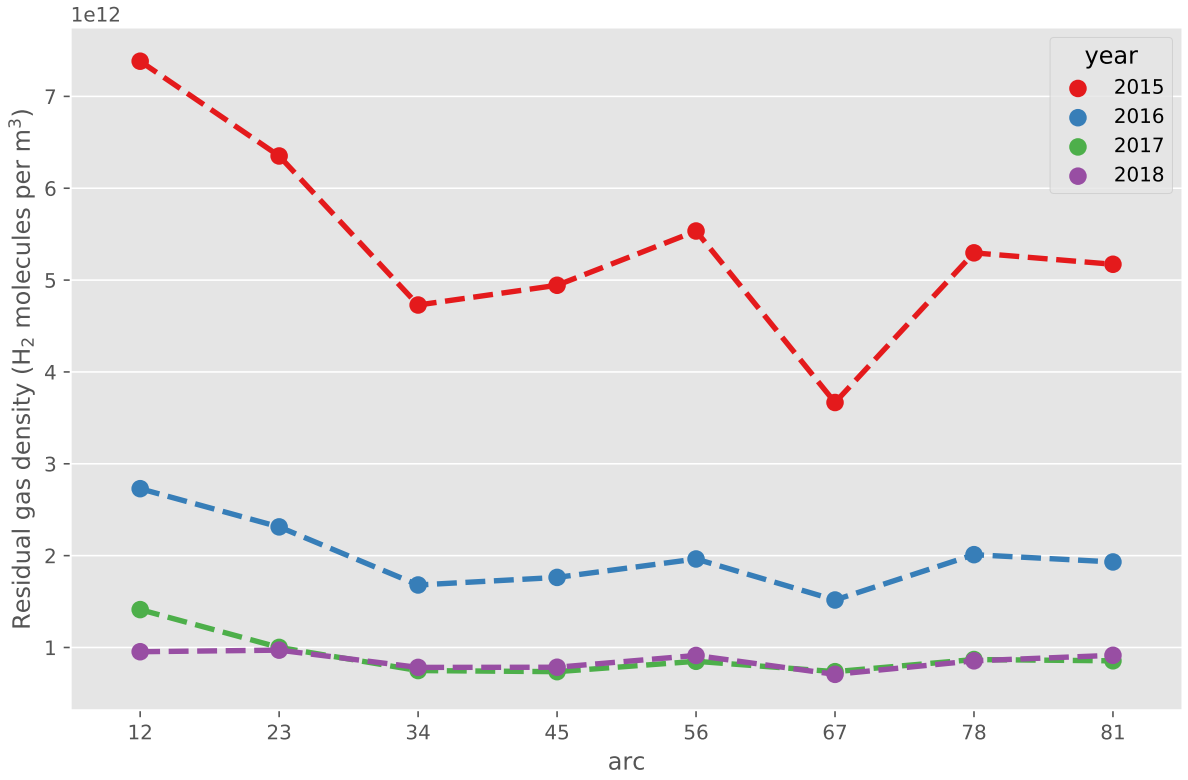

Figure 31: Estimations of the annual residual gas densities for all arc sections based on the baseline doses and the FLUKA simulation. It is assumed that residual dose is 0.

Obtained results, depicted in Figure 31, show that residual gas pressure has decreased over the years 2015-2017, keeping the same level in 2018. In all years arc12 seems to have the highest residual gas pressure, but in the last two years values for the arcs are similar. The small differences in the residual gas densities between the different arc sections are not directly correlated with differences of up to factor 4 in the heat load on the beam screen [15].

A comparison between the measurements and simulation is presented in Figure 30. The agreement is good, however by assuming that small residual dose would remain even if there was no residual gas in the vacuum, the better agreement can be obtained Figure 59. In such a case the estimations of residual gas densities would be even lower, as shown in Figure 58.

4.2.2. Identification of spikes

As it was presented in chapter 4.2 in each arc section there are BLMs which reported much higher doses with respect to the baseline level. Deviations between the calculated doses in different FODO cells might be explained by the LHC imperfections (aberrations from the theoretical model). It was assumed that the spike is each BLM, whose normalised dose exceeded the arc's third quartile (for BLMs within the same family) by more than 3 $\times$ interquartile range, is considered as a spike. Setting the factor 3 provides good separation between irrelevant small spikes and the large ones that are highlighted in this section. Top BLMs are not investigated in detail because they are located in the different plane with respect to the beam, so they can not be directly compared with beam 1 or beam 2 BLMs.

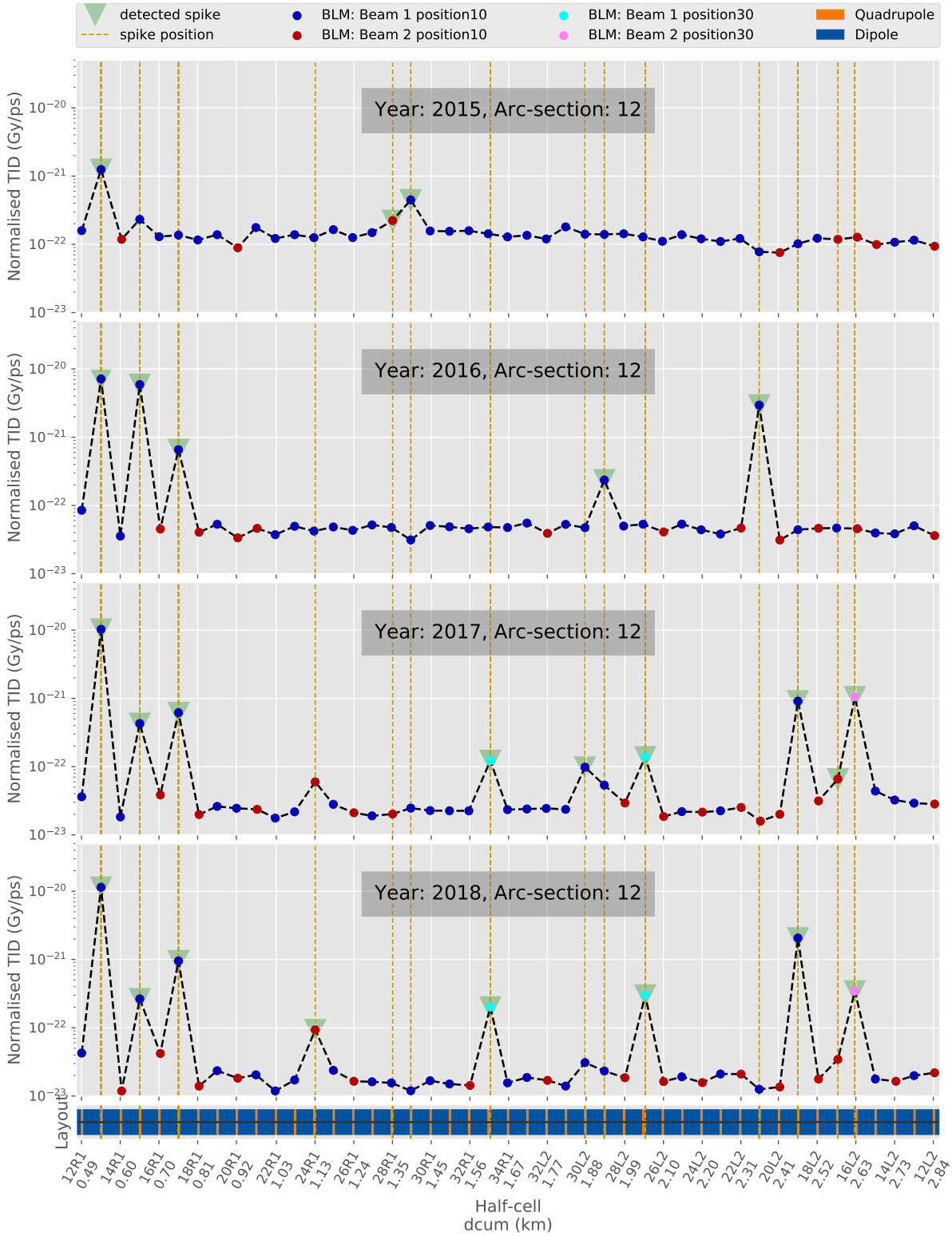

Figure 32: Normalised dose levels in the arc 12 for the years 2015-2018. Top BLMs are not considered and for each half-cell only BLM with highest dose is plotted. Black dashed line has been plotted for the readability only, because dose levels between BLMs cannot be interpolated.

All spikes that were detected and raise significantly above a baseline with the normalised doses over the years are listed in Table 3. The biggest number of them can be observed in the arc sections which

surround high luminosity experiments, i.e arc12, arc81, arc56 and arc45, as indicated in Figure 33.

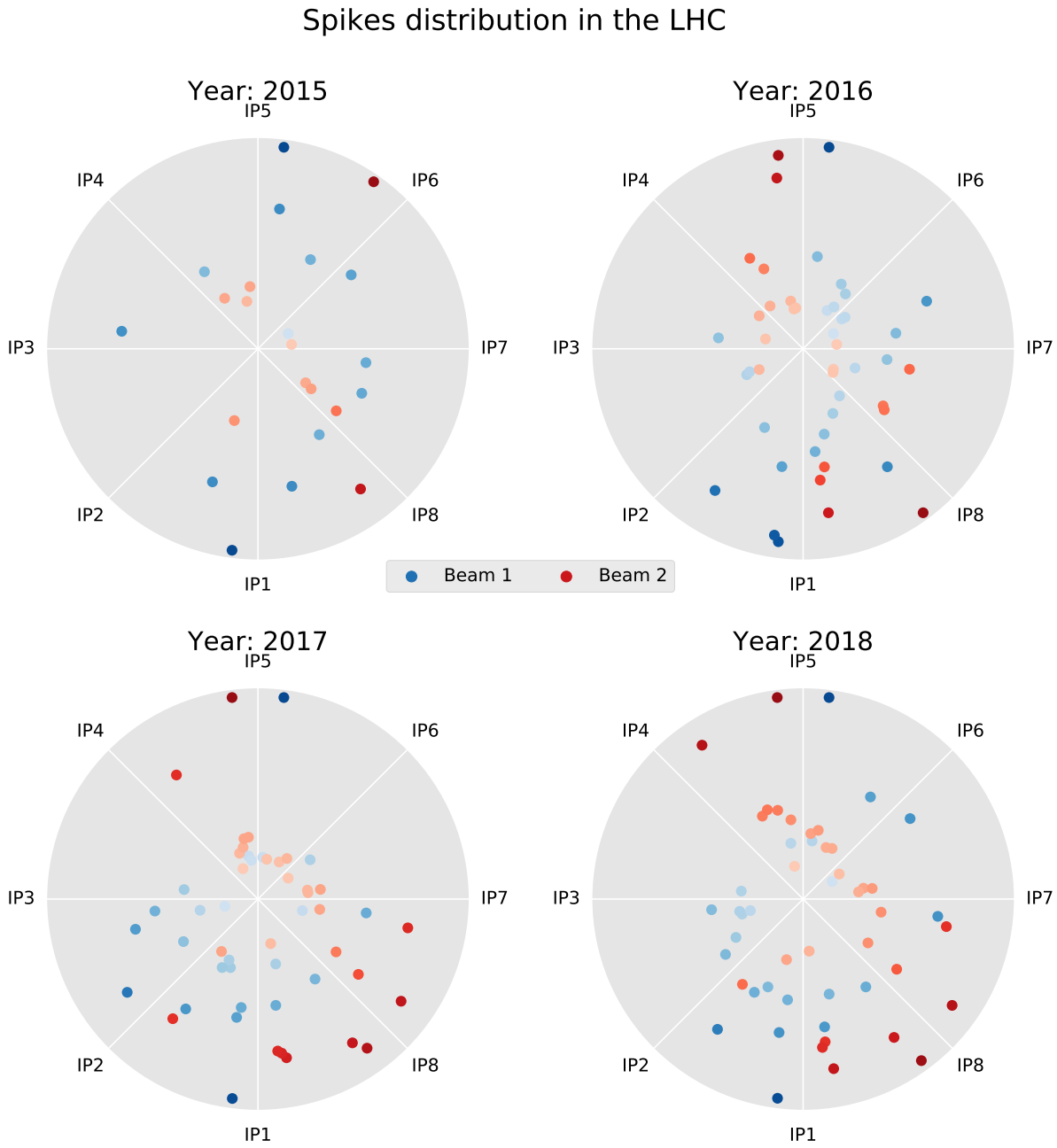

Figure 33: Spikes distribution in the LHC for the years 2015-2018, for both beams BLMs. The radius and colour at the plot reflects the spike strength with respect to the highest spike in the beam1s at the given year.

Table 3: List of selected spikes.

ARC	BLM name	half-cell	dcum	normalised TID ($\#10^{-21}$ps)			
				2015	2016	2017	2018
ARC34							
	BLMQI.13R3.B1I10_MQ	13R3	7207	0.42	0.22	0.13	0.06
ARC23							
	BLMQI.12L3.B1I10_MQ	12L3	6173	0.11	0.04	0.35	0.18
	BLMQI.22L3.B1I10_MQ	22L3	5638	0.13	0.05	0.76	0.06
	BLMQI.24R2.B1I10_MQ	24R2	4462	0.21	0.08	0.19	0.10
	BLMQI.16R2.B1I10_MQ	16R2	4035	0.12	0.04	2.51	0.21
ARC12							
	BLMQI.16L2.B2I30_MQ	16L2	2624	0.07	0.04	1.05	0.34
	BLMQI.19L2.B1E10_MQ	19L2	2467	0.10	0.04	0.91	2.07
	BLMQI.21L2.B1E10_MQ	21L2	2360	0.08	2.96	0.02	0.01
	BLMQI.27L2.B1E30_MQ	27L2	2045	0.05	0.02	0.14	0.30
	BLMQI.29L2.B1E10_MQ	29L2	1932	0.14	0.24	0.05	0.02
	BLMQI.30L2.B1E10_MQ	30L2	1879	0.14	0.05	0.10	0.03
	BLMQI.33R1.B1E30_MQ	33R1	1618	0.06	0.02	0.12	0.20
	BLMQI.17R1.B1E10_MQ	17R1	756	0.14	0.66	0.62	0.95
	BLMQI.15R1.B1E10_MQ	15R1	649	0.23	5.92	0.43	0.27
	BLMQI.13R1.B1E10_MQ	13R1	543	1.25	7.15	10.29	11.45
ARC81							
	BLMQI.13L1.B2E30_MQ	13L1	26110	0.03	1.06	1.30	1.40
	BLMQI.15L1.B2E10_MQ	15L1	26010	0.06	2.85	1.42	1.19
	BLMQI.16L1.B1I10_MQ	16L1	25953	0.07	0.03	0.40	0.76
	BLMQI.17L1.B2E10_MQ	17L1	25903	0.06	0.73	1.70	2.84
	BLMQI.22L1.B1I10_MQ	22L1	25633	0.45	0.24	0.02	0.02
	BLMQI.24L1.B1I10_MQ	24L1	25526	0.13	0.04	0.10	0.23
	BLMQI.19R8.B2E10_MQ	19R8	24193	0.07	0.04	2.44	2.30
	BLMQI.15R8.B2E10_MQ	15R8	23979	0.65	8.55	3.73	6.78
ARC78							
	BLMQI.14L8.B2I30_MQ	14L8	22725	0.08	0.24	0.52	0.51
	BLMQI.16L8.B2I10_MQ	16L8	22625	0.19	0.39	2.77	3.97
	BLMQI.18L8.B2I10_MQ	18L8	22518	0.09	0.06	0.18	0.15
	BLMQI.18R7.B2I30_MQ	18R7	20801	0.06	0.52	1.27	1.24
	BLMQI.16R7.B2I10_MQ	16R7	20701	0.09	0.03	0.06	0.16
	BLMQI.13R7.B1E10_MQ	13R7	20537	0.27	0.21	0.42	0.96
ARC67							
	BLMQI.13L7.B2I10_MQ	13L7	19452	0.14	0.06	0.04	0.08
	BLMQI.15L7.B2I10_MQ	15L7	19345	0.07	0.03	0.06	0.12
	BLMQI.16L7.B1E10_MQ	16L7	19289	0.04	0.29	0.01	0.01
	BLMQI.17L7.B2I10_MQ	17L7	19238	0.04	0.02	0.04	0.09
	BLMQI.32L7.B1E10_MQ	32L7	18433	0.10	0.98	0.01	0.01
	BLMQI.14R6.B1E10_MQ	14R6	17257	0.06	0.08	0.09	0.89
ARC56							
	BLMQI.17L6.B2I30_MQ	17L6	15900	0.90	0.02	0.01	0.01
	BLMQI.19L6.B1E30_MQ	19L6	15802	0.05	0.02	0.01	0.57
	BLMQI.24L6.B2I10_MQ	24L6	15532	0.10	0.03	0.03	0.08
	BLMQI.32L6.B2I10_MQ	32L6	15105	0.05	0.02	0.01	0.08
	BLMQI.20R5.B2I10_MQ	20R5	14250	0.09	0.03	0.03	0.12
	BLMQI.15R5.B1E10_MQ	15R5	13979	0.45	0.28	0.03	0.05
	BLMQI.13R5.B1E10_MQ	13R5	13872	1.25	9.44	11.07	12.50
ARC45							
	BLMQI.13L5.B2E10_MQ	13L5	12788	0.19	6.71	6.89	7.44
	BLMQI.15L5.B2E10_MQ	15L5	12681	0.10	3.48	0.06	0.16
	BLMQI.33L5.B2E30_MQ	33L5	11712	0.04	0.01	0.04	0.26
	BLMQI.29R4.B2E30_MQ	29R4	11391	0.02	0.29	0.02	0.24
	BLMQI.23R4.B2E30_MQ	23R4	11071	0.07	0.47	0.01	0.01
	BLMQI.19R4.B2E10_MQ	19R4	10863	0.13	0.03	1.11	4.10

4.2.3. Evolution of the selected spikes

Selected spikes are investigated in detail in this paragraph. Often, spikes can be grouped because they share similar behaviour (time evolution). It is the case for the spikes produced as an indirect effect of collisions at the experiments since then the spikes can be observed at both sides of an IP, but in the different beams due to the symmetry in the collisions. Figure 34 depicts raw dose rate signal for collision driven spike with the CMS luminosity. The evolution of dose rate follows the luminosity of CMS. However, due to the linearity between the integrated luminosity and integrated intensity (Figure 26), it can be assumed that in a long term evolution the dose of a collision driven spike scales linearly with the integrated intensity for collision beam modes.

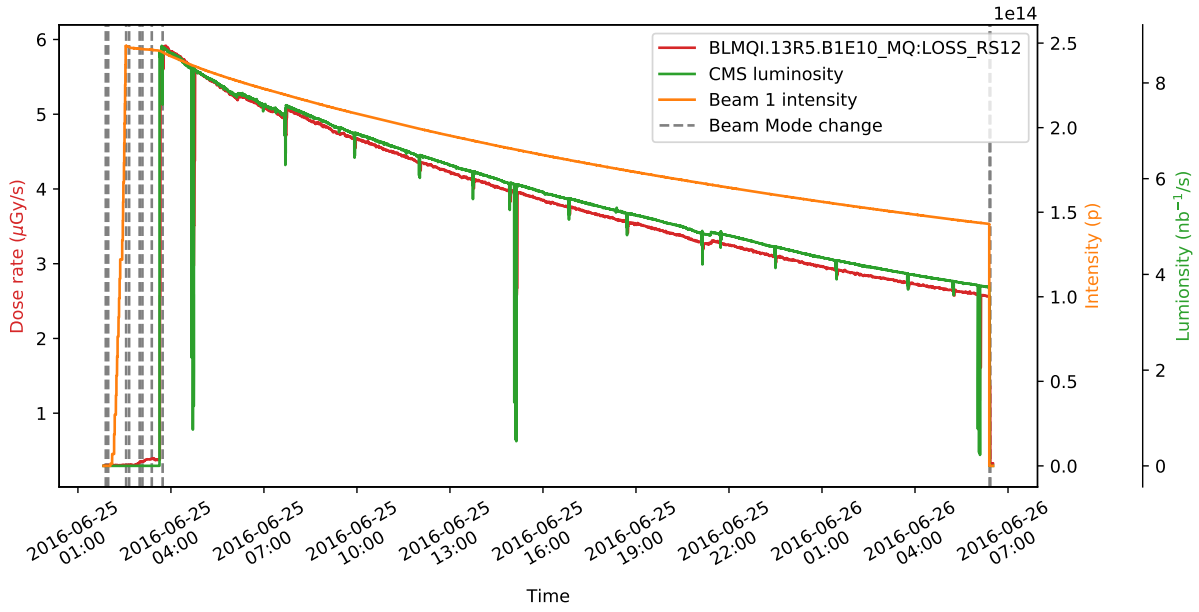

Figure 34: An example of the dose rate for the collision driven spike, i.e. BLMQI.13R5.B1E10_MQ, with the intensity and luminosity evolution. Dose rate signal reflects the CMS luminosity.

The procedure of the spikes analysis has been described in detail in chapter 3.4. The first step was to determine if a spike is collision driven based on the comparison of the evolution with the corresponding (the same arc and BLM family) baseline evolution. Period after 11.11.2017 until the end of 2017 contained special physics runs and cannot be compared with the standard LHC operation.

BLMQI.13R5.B1E10_MQ and BLMQI.13L5.B2E10_MQ ("DS-like" spikes)

The two spikes at both sides of CMS in the 13th cells (Figures 64 and 65) are the representative ones. They are caused by the particles with too large dispersion after passing dispersion suppressor regions. The linear behaviour, shown in Figure 35, for the collision modes can be observed over the years 2016-2018, irrespective of the LHC parameter changes. For non-collision modes slopes are comparable with the baseline, thus these spikes are collision driven. It has to be pointed out that this does not imply that the cause is a collision itself, but rather the change of the accelerator settings needed to perform collisions. Asymmetry between the beams can be observed. The spike at beam 1 is higher, than respective spike at beam 2. This inconsistency is a matter of the ongoing investigation. Similar spikes are expected to be observed at ATLAS (that is the twin experiment). Indeed, on the right side of IP1 in the 13th half-cell a spike with similar dose level can be noticed (BLMQI.13R1.B1E10_MQ – Figure 32). However, on the left side in the same half-cell the dose levels are lower and the hottest BLM is after the quadrupole (BLMQI.13L1.B2E30_MQ). The spike in the 13L5 was not present in 2015 and further investigation of the cause might be useful.

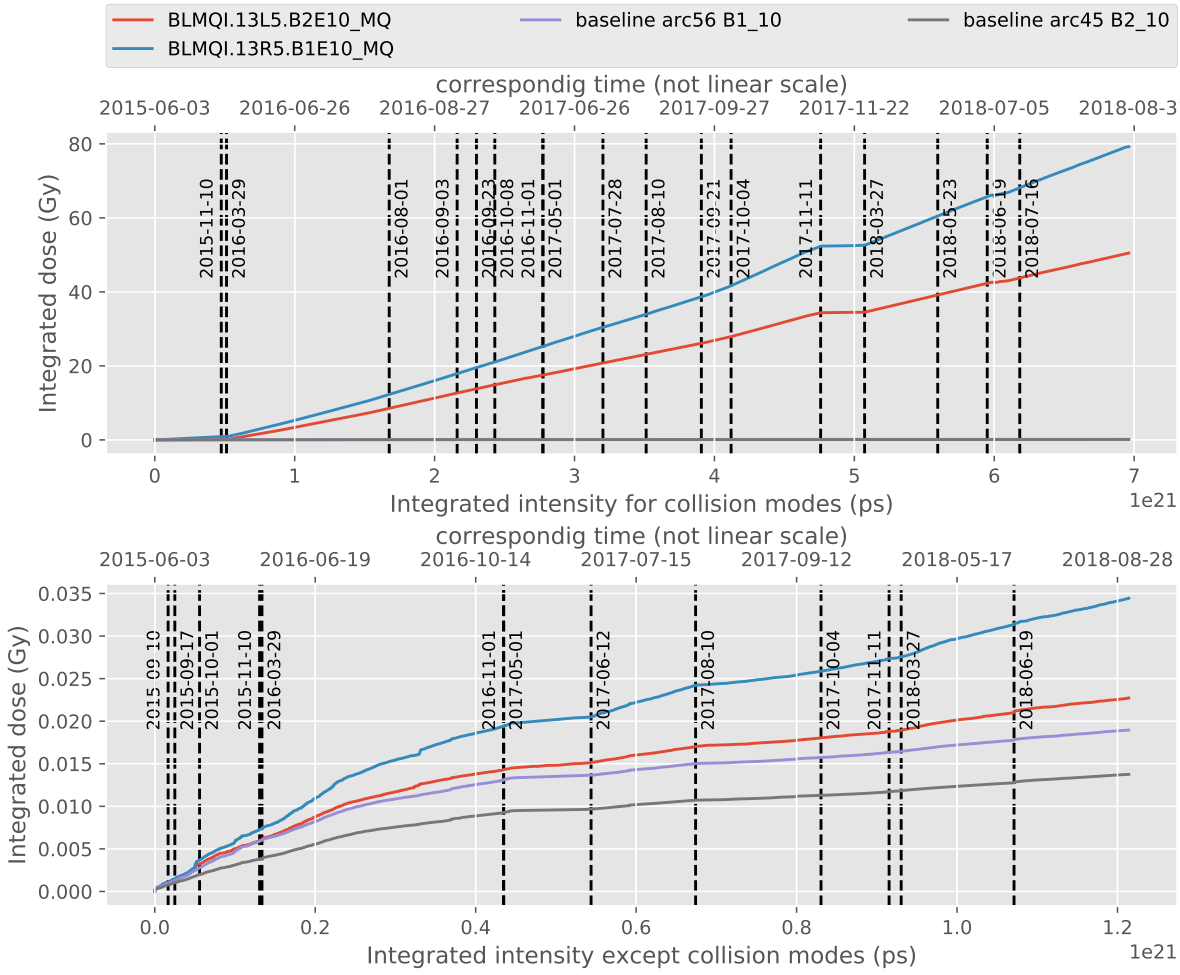

Figure 35: Dose evolution over the integrated intensity for BLMQI.13R5.B1E10_MQ and BLMQI.13L5.B2E10_MQ with the contradistinction for collision and non-collision beam modes.

BLMQI.16L2.B2I30_MQ

The spike in the half-cell 16 on the left side of ALICE (half-cell 16L2) was a reason of multiple beam dumps in 2017[16]. The highest dose is observed in the BLM located on the beam 2 side, at the position 30. It appeared in the beginning 2017, after Extended Year End Technical Stop (EYETS). It is not collision driven, since it can be observed in both collision and non-collision beam modes. Out of analysed spikes, this one had the highest dose contribution during non-collision beam modes. The most probable source of the spike is the accidental air inlet into the beam vacuum during the EYETS [16]. During the LHC operation protons in the beam interacted with the frozen gasses, leading to beam losses and dumps. On the 10^{th} of August 2017 beam screen "flushing" was performed, but it made dumps appear even more often. The slope in Figure 36 decreases at that time, so beam screen flushing reduced steady state losses that contributed to the dose, but also increased the peak losses that triggered dumps.

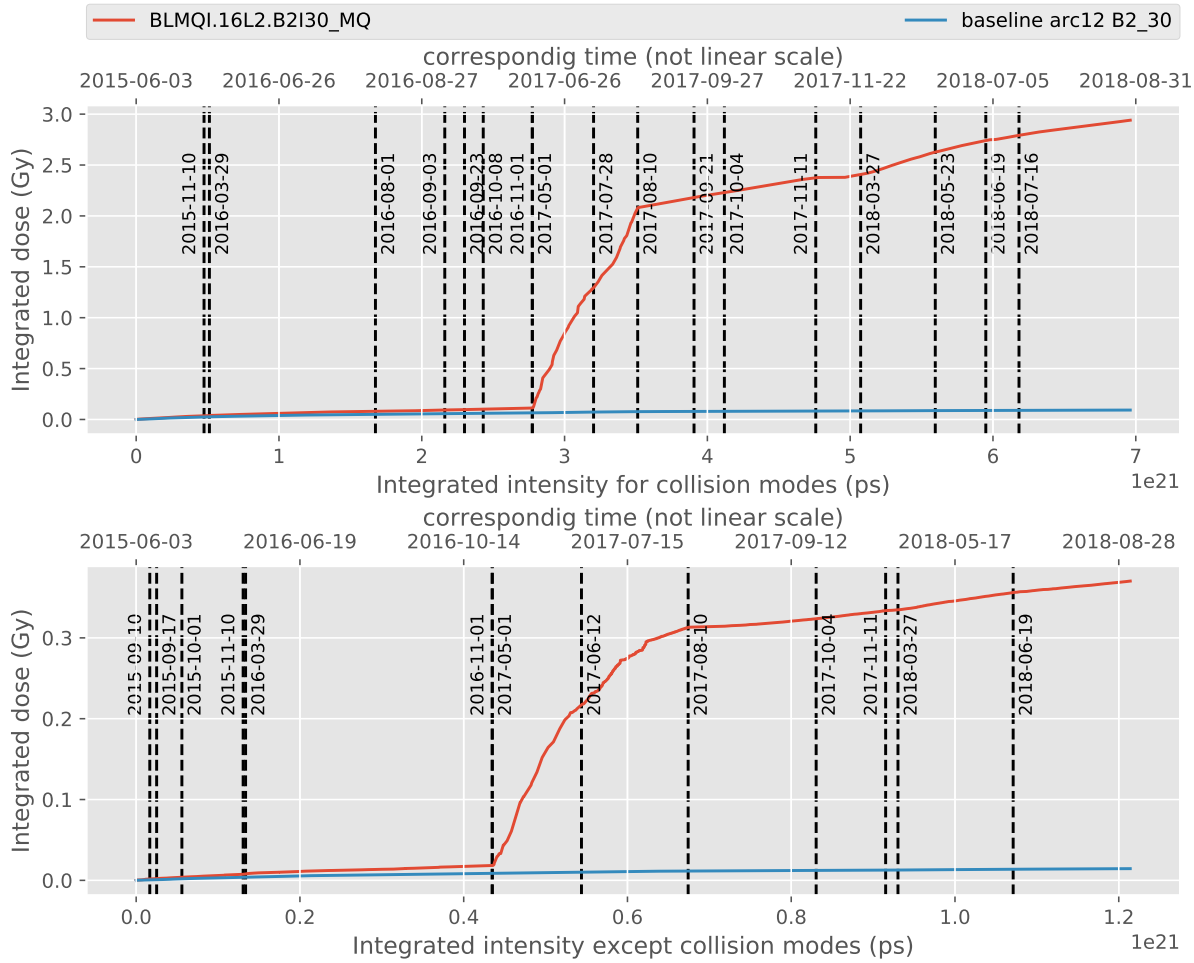

Figure 36: Dose evolution over the integrated intensity for BLMQI.16L2.B2I30_MQ with the contradistinction for collision and non-collision beam modes.

BLMQI.16L1.B1I10_MQ

The next spike is located at the 16$^{\text{th}}$ half-cell on the left side of the ATLAS experiment in beam 1 (Figure 32). It appeared in 2017. Evolution is presented in Figure 37. It suggest that spike is not collision driven because difference a behaviour with respect to the baseline can be observed in both subplots.

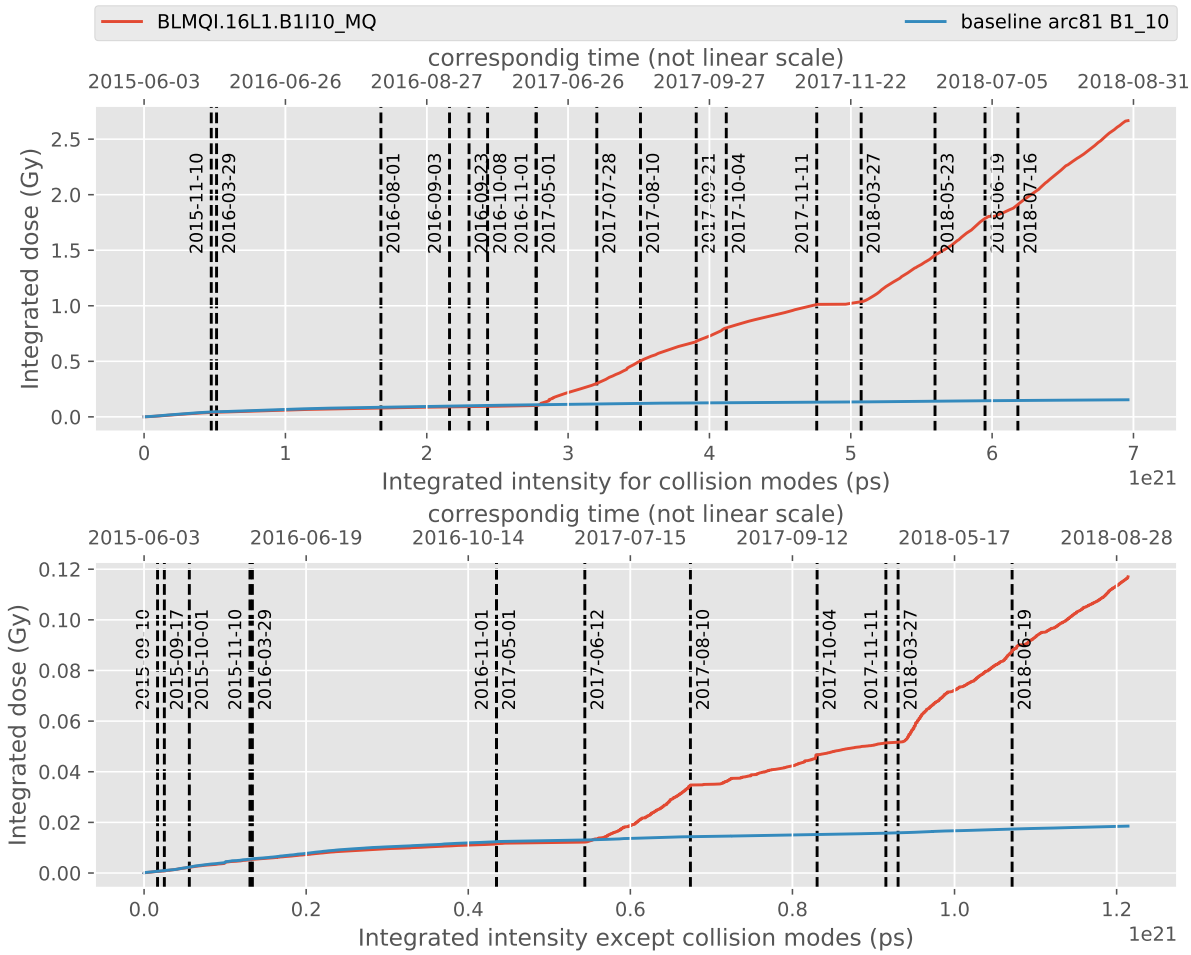

Figure 37: Dose evolution over the integrated intensity for BLMQI.16L1.B1I10_MQ with the contradistinction for collision and non-collision beam modes.

For this spike it is worth noting the evolution divided between different energies. Protons in the beam have 450 GeV after the injection and 6.5 TeV after the acceleration, which is performed during *RAMP* beam mode (not included in the evolution). In Figure 38 it can be seen, that for 450 Gev beam modes spike behaves in a similar way to the baseline, but for 6.5 TeV beam modes slope differs a lot from the baseline since 2017. It changed between 2017 and 2018 by getting steeper.

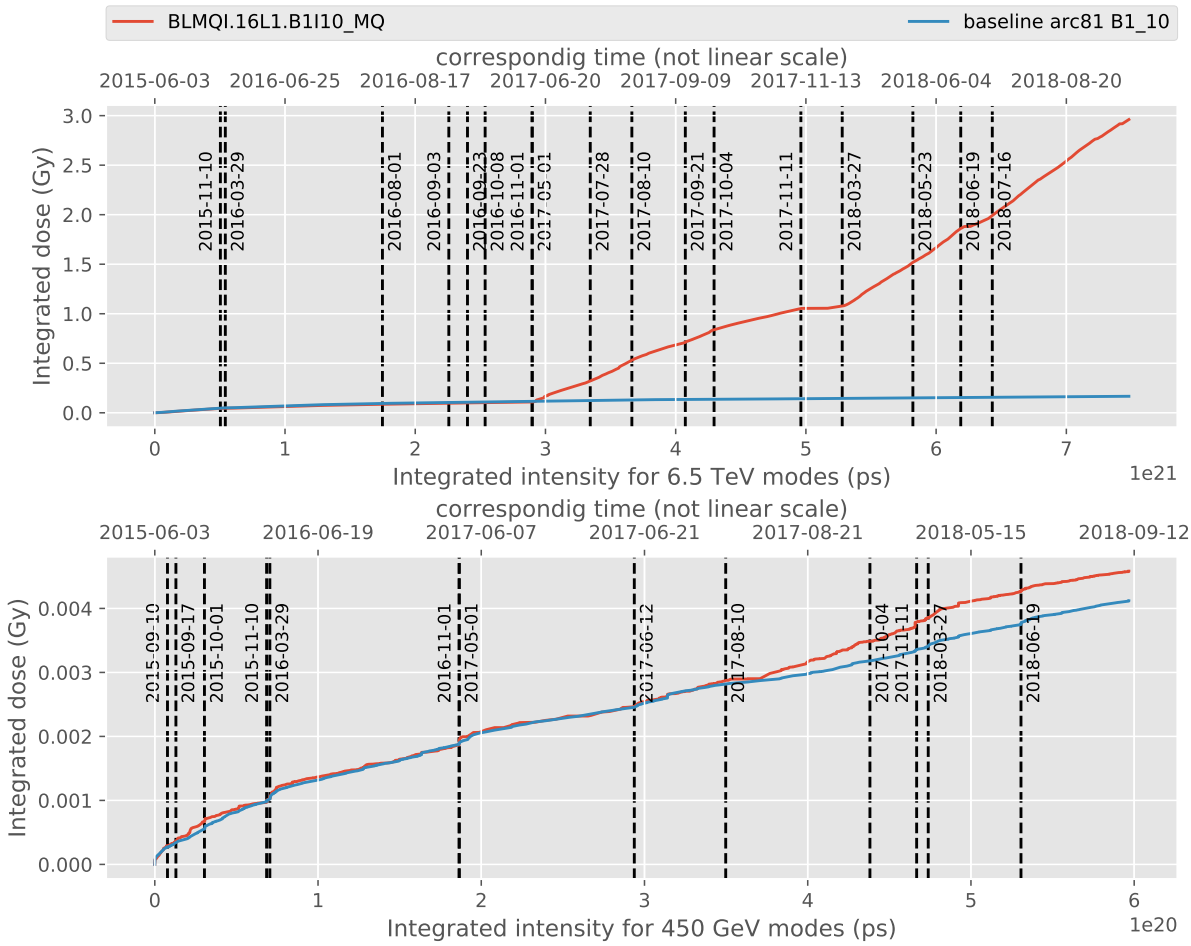

Figure 38: Dose evolution over the integrated intensity for BLMQI.16L1.B1I10_MQ with the contradistinction for 450 GeV and 6.5 TeV beam modes.

BLMQI.19L2.B1E10_MQ and BLMQI.19R8.B2E10_MQ

Another correlated set of spikes was identified in the 19$^{\text{th}}$ half-cells – for beam 1 at the left side of ALICE (arc12 – Figure 32) and for beam 2 at the right side of LHCb (arc81 – Figure 69). Both are collision driven and in non-collision beam modes agree/coincide withe the corresponding baseline as presented in Figure 39. They are symetric with respect to IP1. Both spikes appeared in 2017 and exist in 2018. One of possible causes is the introduction of Achromatic Telescopic Squeezing (ATS) scheme in the beginning of 2017. In 2017, around the beginning of October (approximately 04.10.2017) the slope of the evolution of both spikes increased. At that time luminosity levelling technique started to be used [30]. The cause of non-linear behaviour in the beginning of 2018 (until the middle of July) has to be investigated in the future.

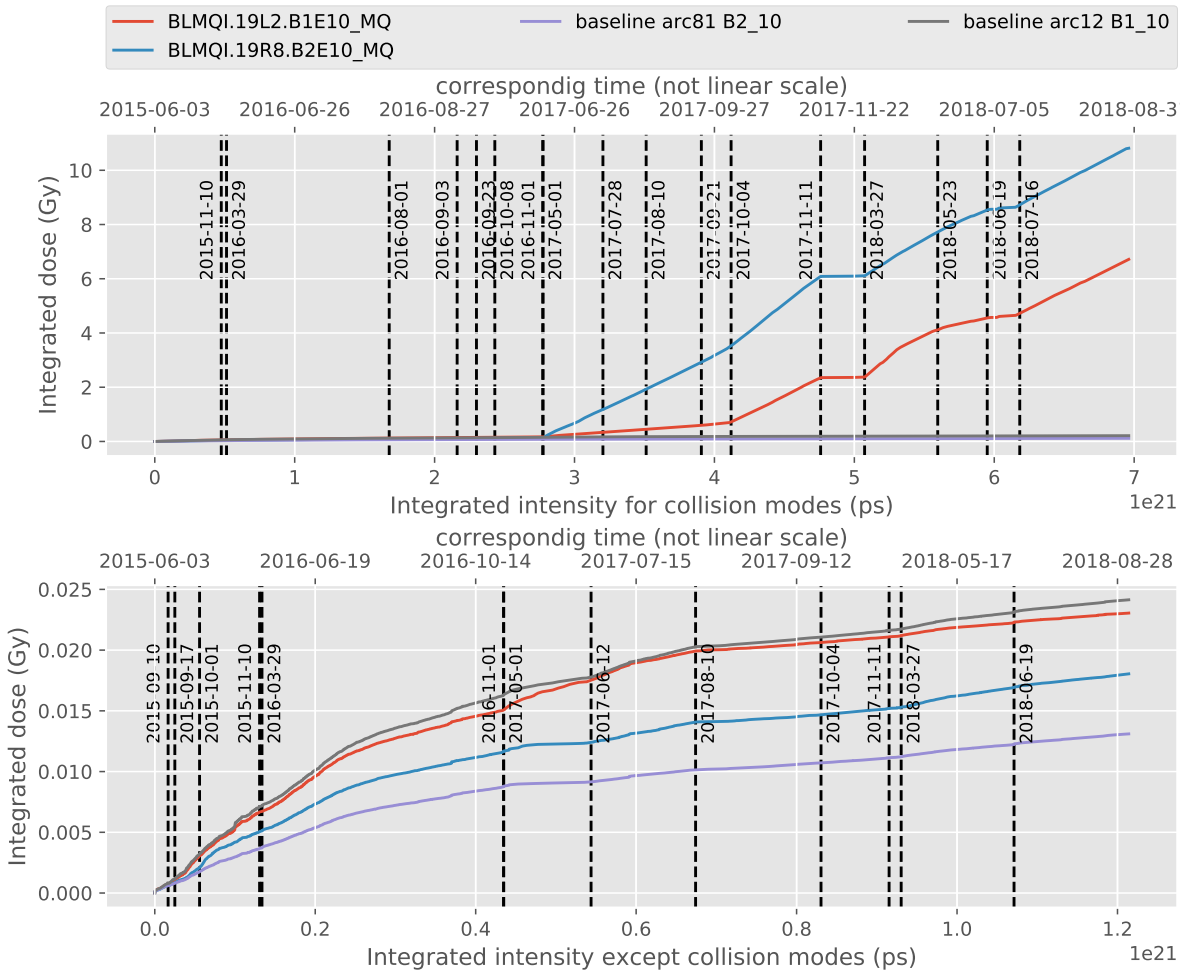

Figure 39: Dose evolution over the integrated intensity for BLMQI.19L2.B1E10_MQ and BLMQI.19R8.B2E10_MQ with the contradistinction for collision and non-collision beam modes.

Do this behaviour exists on the CMS side? Even though a significant spike can be found in the same position with respect to CMS (19R4 - Figure 40) a correlated spike in the half-cell 19L6 does not exists. Furthermore, the behaviour of the 19R4 spike is not correlated with neither BLMQI.19L2.B1E10_MQ nor BLMQI.19R8.B2E10_MQ. However, ATLAS and CMS collide in the different planes, therefore it would be informative to study if it could cause this asymmetry between the twin experiments.

BLMQI.19R4.B2E10_MQ

The spike that is visible in the 19$^{\text{th}}$ cell on the right side of IP4 is due to the collisions. It grew up in 2017 and since then had linear behaviour that changed two times - in the middle of September 2017 the slope decreased and in the beginning of 2018 operation it increased significantly. First date corresponds to the β^* change (21.09.2017), but it is likely that the cause is different. Since the 2018 the β^* is the same as at the end of 2017. It might be worth investigating what happened around the middle of September 2015. For non-collision beam modes a huge increase can be observed. To be more precise it is only visible in *RAMP*, *FLAT TOP*, *SQUEEZE* and *ADJUST* beam modes.

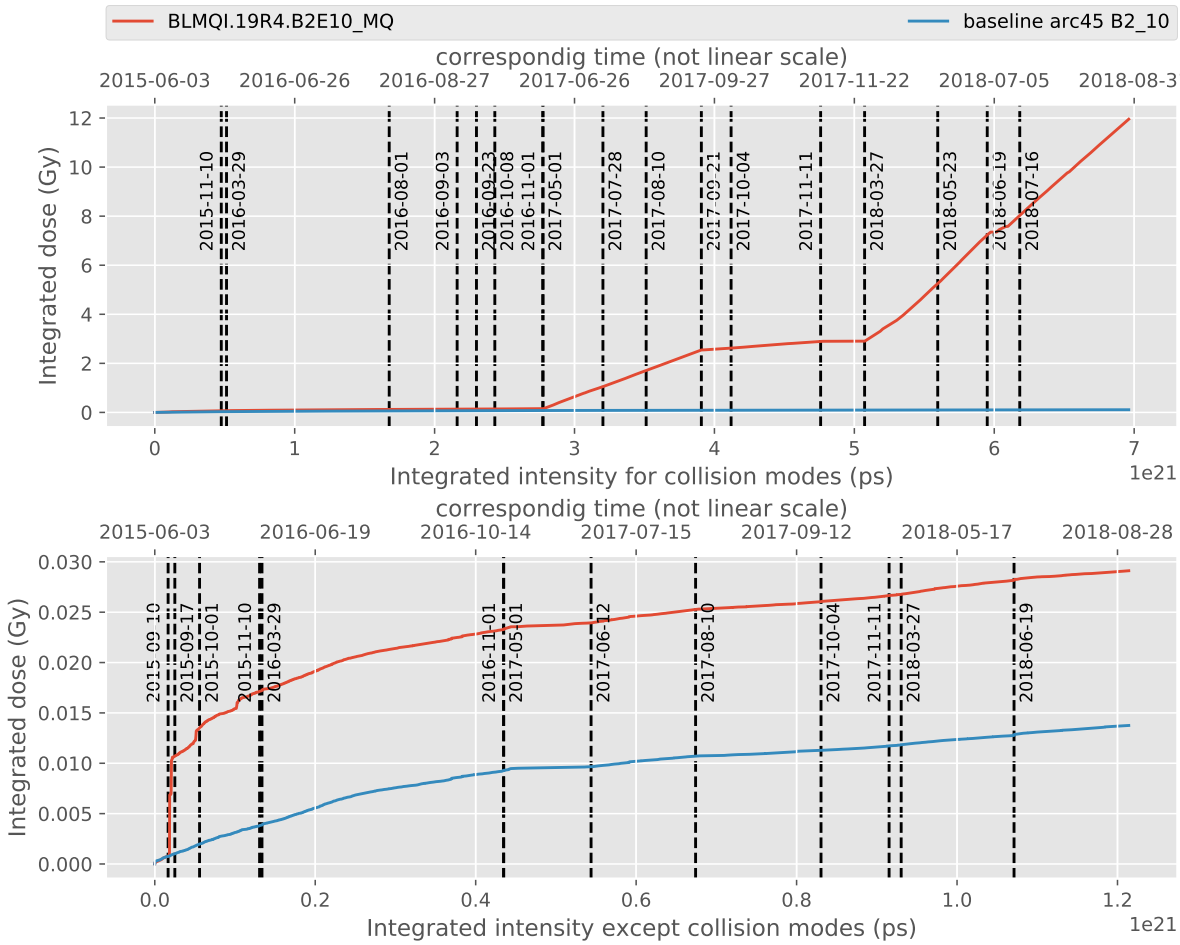

Figure 40: Dose evolution over the integrated intensity for BLMQI.19R4.B2E10_MQ with the contradistinction for collision and non-collision beam modes.

BLMQI.20R5.B2I10_MQ, BLMQI.32L6.B2I10_MQ and BLMQI.24L6.B2I10_MQ

In arc56, that is illustrated in Figure 65, spikes in beam 2 can be observed. The spike related to BLMQI.32L6.B2I10_MQ appeared in 2017, whereas BLMQI.20R5.B2I10_MQ and BLMQI.24L6.B2I10_MQ were already visible. At the beginning of 2018, a significant increase of all three spikes with respect to the baseline was observed. Though the difference in 2017, BLMQI.32L6.B2I10_MQ and BLMQI.24L6.B2I10_MQ share the same linear behaviour in 2018. Since the clear discrepancy with the baseline can be observed only during collision modes, these spikes are likely to be collision driven.

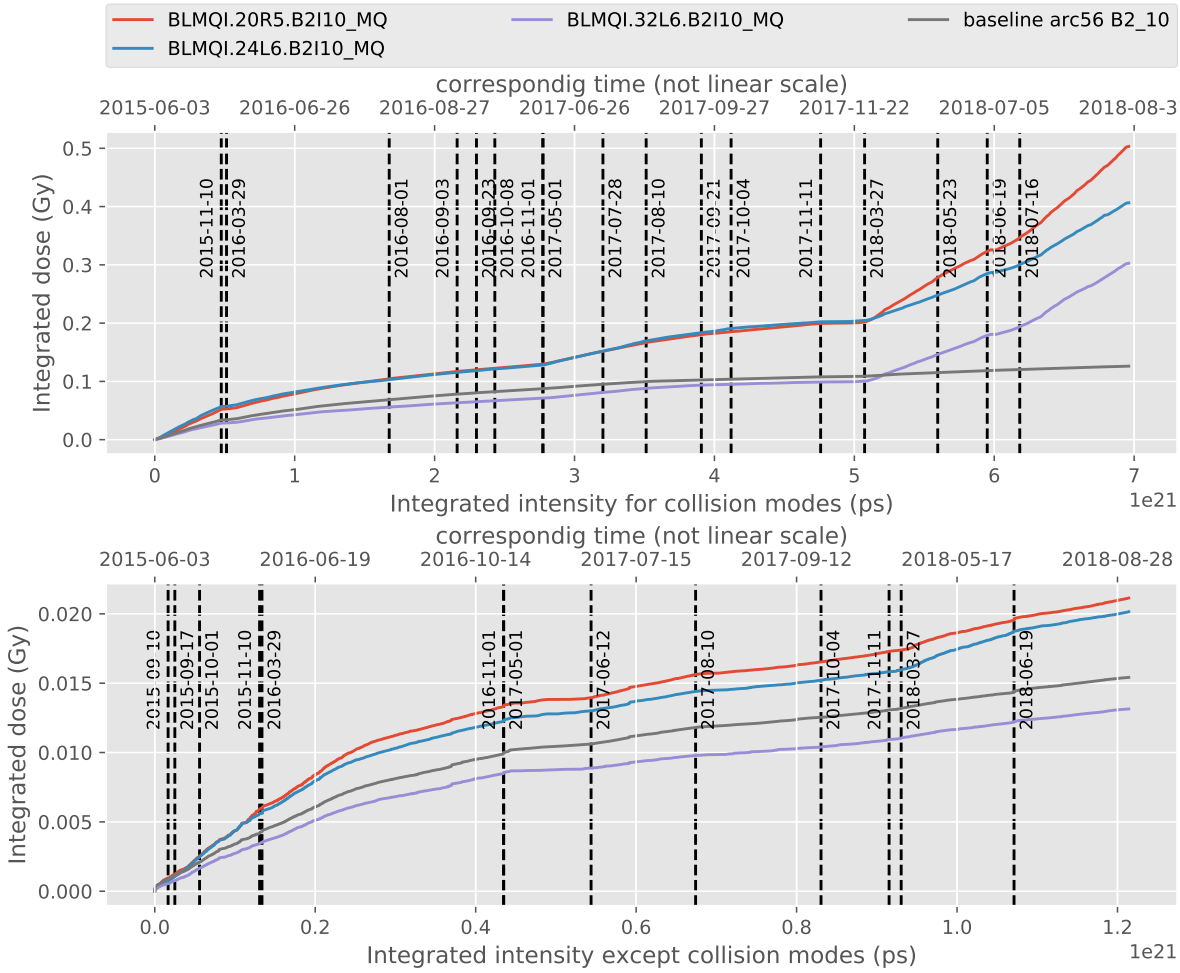

Figure 41: Dose evolution over the integrated intensity for BLMQI.20R5.B2I10_MQ, BLMQI.32L6.B2I10_MQ and BLMQI.24L6.B2I10_MQ with the contradistinction for collision and non-collision beam modes.

BLMQI.22L3.B1I10_MQ and BLMQI.24R2.B1I10_MQ

In Figure 61 two spikes in the deep arc were noticed. Their evolution is depicted in Figure 42. What makes them interesting is the behaviour in 2017 during collision modes. Since the beginning of the year until the middle of September their doses increased linearly. After Technical Stop 2 (TS2) their slopes increased, but remained linear. It might be due to the β^* change from 40 cm to 30 cm but in principle it should not affect arc optics. Around the beginning of October until the end of 2017's considered period (11.11.2017) BLMQI.22L3.B1I10_MQ increased even more, whereas BLMQI.24R2.B1I10_MQ stayed almost flat. It has to be investigated if start of the luminosity levelling was the cause. The levelling is used also in 2018, but that steep incline of BLMQI.22L3.B1I10_MQ is not observed. Moreover, the levelling in general should not be observed in arcs that are not adjacent to the high luminosity experiments.

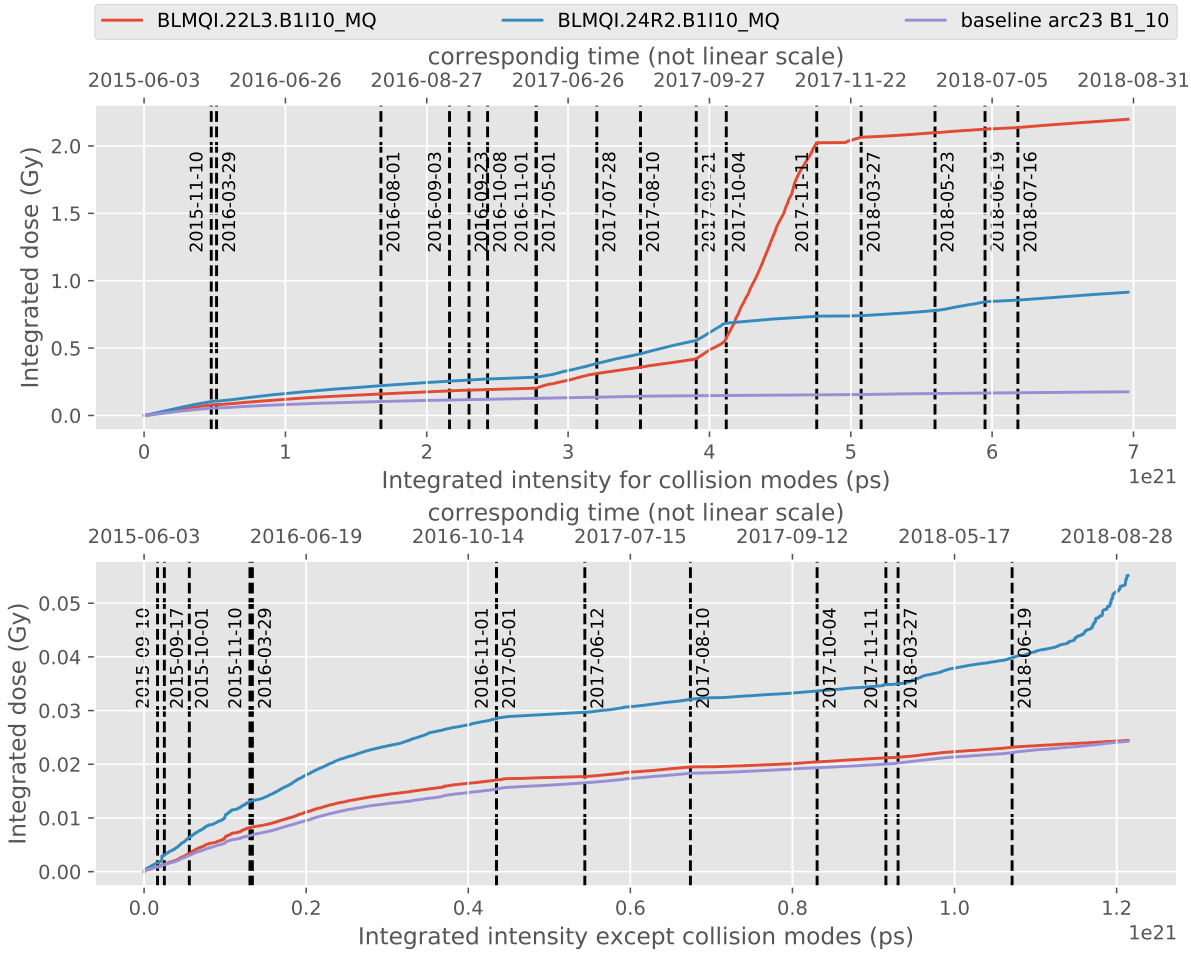

Figure 42: Dose evolution over the integrated intensity for BLMQI.22L3.B1I10_MQ and BLMQI.24R2.B1I10_MQ with the contradistinction for collision and non-collision beam modes.

4.2.4. Top BLMs

Spikes observed in the top BLMs were not studied in detail. Apart from arc34 (Figure 63) and arc67 (Figure 67) dose levels in at the dipole interconnections were lower than at the quadrupoles. However, they cannot be directly compared due to the location in the different plane. Spikes in those two arcs show similar behaviour in the considered years. Both arcs are located close to the collimation regions (IP7 or

IP3) and a collimation related mechanism might be the cause. The distribution of the top BLMs spikes in the LHC is illustrated in Figure 60.

5. Discussion

In this thesis the behaviour of total ionising dose during Run 2 has been presented. With the focus on the Large Hadron Collider's arc sections, during proton-proton operation, its evolution and distribution has been evaluated. Following the assumption that the main contributor in the arc losses are beam-residual gas interactions, which are proportional to the intensity and residual gas density, data from Beam Loss Monitors were analysed. Each arc section consists of a sequence of FODO cells, where BLMs are periodically distributed. It was hypothesised that the loss pattern, and hence the dose, follows the periodic arc structure. This was studied throughout this thesis and is discussed below.

The first part of the dose analysis examined in detail the dose distributions with focus on the typical behaviour. This behaviour was that the majority of the BLMs in each arc section, within the group that shares the same BLM location with respect to the FODO cell, shows similar evolution over time.

It was observed that over the years 2015-2017 integrated intensity normalised annual dose values were decreasing for all arc sections. It suggests that the vacuum levels improved yearly. The most likely cause is due to the continuous operation of the vacuum pumps. However, it is also possible that a different beam loss effect started to dominate, thus further vacuum improvement cannot be observed in the baseline doses. It might then explain the comparable levels in 2017 and 2018; the vacuum level should have slightly improved resulting in the baseline remaining at the same level. Nevertheless, the most reasonable explanation is that vacuum pumps have not been able to improve vacuum anymore and hence the residual gas density remained constant. Baseline annual dose values for arc section 12 were always the highest. It could be explained by the *16L2* problem [16] in the years 2017-2018, but that behaviour has been observed since the beginning of Run 2. The first possible explanation is the proximity of the ATLAS experiment. As a result of luminosity production collision debris is created. If it is not intercepted by the experiment's collimators or lost before the arc, it could be lost in the adjoining arc sections and thus influence baseline dose levels. Due to the local symmetry of the layout with respect to IP1, this behaviour should be observed in the both neighboring arcs but in different beams (for arc 81 in beam 2; for arc 12 in beam 1). However, the levels in arc 81 are lower than in arc 12, therefore the likely explanation is the worse vacuum in arc section 12.

Not only annual normalised dose levels were presented, but also their changes over time. It was proven that each baseline evolution over the integrated intensity was not linear in the years 2015-2016 and at the beginning of 2017. It supports the hypothesis about the vacuum conditioning, thus the continuous reduction of residual gas density. At the beginning of 2017 the strongest nonlinear evolution was observed for arc 12 which supports the hypothesis about the worst vacuum quality in this arc section. Since 10^{th} of August 2017 the dose growth became linear. Around this date the bunch number has been reduced to prevent dumps caused by the *16L2* problem [16] from occurring. It might be a coincidence that at that time vacuum reached the conditioned state, but it is also possible that the bunch number, thus the longitudinal distribution of the intensity, has an impact on the baseline level. At the beginning of September 2017 the filling scheme changed (*BCMS* to *8b4e*) in order to reduce electron cloud effect

[27]. Even though this effect has been weakened, the change was not visible in the baseline evolutions. Although this effect is the main contributor to the heat load [14, 15] on the beam screen, it is not clearly visible in the BLM losses. Despite the differences (up to a factor of 4) in the heat load among the different arc sections [14, 15], dose levels, thus the beam losses, were similar. This confirms that heat load at the beam screen is not beam loss driven.

An example of the direct application of the baseline dose levels was presented. By combining obtained values with the FLUKA simulation it was possible to obtain estimations of the residual gas densities in the different years and arcs. Provided that the assumptions of the simulation are valid, it was observed that residual gas densities decreased in the years 2015-2017 and then remained stable in 2018. Moreover the differences in density among the different arc sections dropped. In 2018 all densities were almost the same among all arc sections as well as in the previous year. It suggest that the conditioned state had been achieved and further vacuum improvement was not observable.

However a question remains; how can the results be verified? Firstly, the conversion between density and pressure has to be defined (could the ideal gas law be applied?). The second limitation is the precision of the LHC vacuum pressure sensors because the actual pressure is below their detection limit. Although it was shown that FLUKA simulation for the arc half-cell agrees with the baseline values, the assumption that losses at the beam 1 and beam 2 sides are equal should be investigated in the future, because BLM based measurements are not symmetric with respect to the beams. In addition a scaling function between the FLUKA simulation and normalised dose requires additional studies. It was shown that by assuming that a residual dose will appear even without residual gas molecules, a better agreement with the simulation can be obtained. This residual dose might be caused by the different beam loss mechanisms, imperfections in the offset correction or by a too idealised FLUKA model. Detailed investigation of this phenomena would be useful in the future. For example the information on how the residual dose would change if the calculation was performed without offset correction could be applied to the final tuning of the offset correction algorithm.

The second part of the dose analysis examined the strong anomalies in the periodic loss pattern, i.e. spikes. For spikes the main mechanism of beam losses was no longer interactions of beam with residual gas molecules. All LHC arc sectors were investigated for the existence of relevant irregularities from the annual perspective.

Since many accelerator settings might have an impact on the dose evolution, the spike developmnet was always compared with the corresponding baseline. That approach provides a way to separate changes of accelerator/beam parameters that had an impact on the losses in general and those that affected the selected spike only. Spikes were categorised into two groups – collision driven and non-collision driven. Collision driven spikes followed baseline evolution for non-collision beam modes, whereas non-collision spikes mismatched the baseline evolution for both collision and non-collision beam modes. Such an approach provides a systematic way of spike classification. Often, due to the symmetry of the LHC, collision-driven spikes share similar or correlated behaviour. For example in the 13^{th} and 15^{th} cell, at both sides of ATLAS and CMS, spikes in the outgoing beams can be noticed, however the dose values are not symmetric. Since ATLAS and CMS collide in different planes and arc quadrupole BLMs are always located in the horizontal plane, it would be interesting to investigate the possibility that spikes appear only in a vertical plane, and therefore is not observed by a horizontal BLM.

It is important to point out that these studies would not be possible without the preceding software development. This is the first structured and systematic approach to the dose analysis based on the BLM data. All developed tools are now highly utilised by MCWG in the groups daily activities. Presented results will also be used within the R2E project to estimate risks of radiation related electronics failures

and material ageing of equipment installed in the LHC tunnel. By combining the obtained dose levels with a FLUKA simulation it will be possible to convert total ionising dose, that is useful for cumulative effects evaluation, into the *high energy hadron fluence* that is used in the estimation of single event effects occurrence probability [25]. Knowledge about the conversion factor will allow an assessment of single event effects in the electronic racks located directly under the beam pipe. Provided that spikes are monitored the developed tools will also play a preventive role. The occurance of a spike or an unexpected increase of dose levels would trigger actions, that hopefully would save exposed equipment.

6. Outlook

This thesis focused on the arc section dose evaluation. However, the design of the developed tools enables a further radiation examinations relatively effortless. The considerations about possible upgrades should start from the improvement of the tools, that are the core of each analysis.

Intensity calculation

Referring to the intensity calculation, the first extension would be to estimate losses during the injection. It could be achieved by setting together the injected intensity with the intensity extracted from SPS. Although noise level in the intensity readout is quite low, the signal flattening for injected intensity calculations would avoid detecting peak in the noise around the genuine injected intensity value.

The second improvement would be the disentanglement of the intensity calculation for both beams. In fact it would not improve the existing calculation but the information about integrated intensities for each beam could be useful for asymmetries explanation or for FLUKA simulation scaling.

Dose calculation

Moving to the dose calculations, detailed analysis of the different beam modes contribution requires higher precision in the raw data, especially for short beam modes. Currently data is interpolated in order to make the integration period cover the whole *beam subinterval*. If the losses in two adjacent beam subintervals differed a lot, the interpolation would entangle the results, and therefore would make drawing conclusions more discommoding. The stronger the impact is, the shorter and the more diverged the beam subintervals are. The first enhancement would be then to study a higher resolution of data[1] for selected BLMs only, i.e. spikes. However, such an improvement requires additional investment in the hardware.

Although in recent years, for considered proton-proton operation, integrated intensity for collision modes scaled linearly with the integrated luminosity of the high luminosity experiments, Run 3 may differ. Therefore, to provide collision driven spikes analysis, looking at the dose evolution over the integrated luminosity for an experiment might be needed. In that case spikes could be compared also with the behaviour in Run 2. The algorithm should be analogous to the intensity calculation, however integrated luminosities for each experiment should be calculated.

Analysis extension and further applications

The design and the automation of the tools provides easy access to the processed data, thus developing new packages for further analysis becomes possible. Firstly, the current baseline and spikes studies should be extended with the missing part of proton-proton run of 2018. Likewise the dose levels during the ion run should be investigated with the same methodology.

As shown, the FLUKA simulation for the arc FODO cell shows good agreement with the measured doses. It would be interesting to investigate the conversion between obtained residual gas densities and

[1] LOSS_RS09 – running sum 1.03 s

pressures in order to compare with the vacuum pressure measurements. Moreover, the unified algorithm of BLM data processing ensures the comparability of obtained normalised doses. Consequently, they can be used for various FLUKA simulation scaling.

Since Beam Loss Monitors are used in the rest of CERN accelerators, it would also be useful to extend the systematic and automated analysis to the SPS, PS, PSB accelerators (depicted in Figure 1). However they are different to those installed at LHC, therefore the development of new algorithms becomes necessary.

Although the BLM system allows the calculation of the TID, it is not primarily a dosimetry system. Thus, a comparison with dedicated radiation detectors, like RadMONs [2], would validate the BLM based analysis and provide additional data.

Even though the spike analysis is well structured, a spike can be detected only when it exceeds significantly the baseline. The process of dose accumulation requires time. Automation of the comparison of a BLM evolution with the respective baseline evolution would allow to detect anomalies immediately after they started. Moreover, the analysis of machine learning feasibility in the TID evolution monitoring should be studied.

Finally, it would be very informative to estimate which accelerator/beam parameters are relevant for baseline dose levels. Considerable approach would be to apply *Random Forests* [4] which are one of machine learning algorithms.

7. Conclusions

The continuous particle losses are an integral part of the LHC operation, however occurring mixed radiation fields are able to impact on accelerator electronics causing both cumulative and single event effects. The fundamental part was the dedicated software development that enabled data from Beam Loss Monitors to be analysed. With almost 4000 monitors distributed along the LHC the high resolution studies of both total ionising dose's evolution and distribution in the years 2015-2018 were performed. Such a structured and systematic approach has been utilised for the first time. The research and analysis presented throughout this thesis has provided great insight into the evaluation of dose levels in the LHC arc sections, each consisting of the FODO cells sequence. It was proven that for a given BLM family the majority of BLMs shows similar dose level (i.e. baseline), that is extremely low in terms of radiation impact on the lifetime of the equipment. By combining baseline measurements with the FLUKA simulation the lowest achievable residual gas density has been potentially identified. It occurred that over the years 2015-2017 densities were decreasing and remained constant in 2018, when no clear differences among different arc sectors could be identified. However, doses measured by particular arc BLMs exceeded the baseline by up to 3 orders of magnitude. For selected spikes the evolution and underlying mechanisms were investigated. The evidence from this study indicates that dynamic spikes behaviour makes the continuous monitoring critical in terms of equipment protection.

A. LHC Schedules

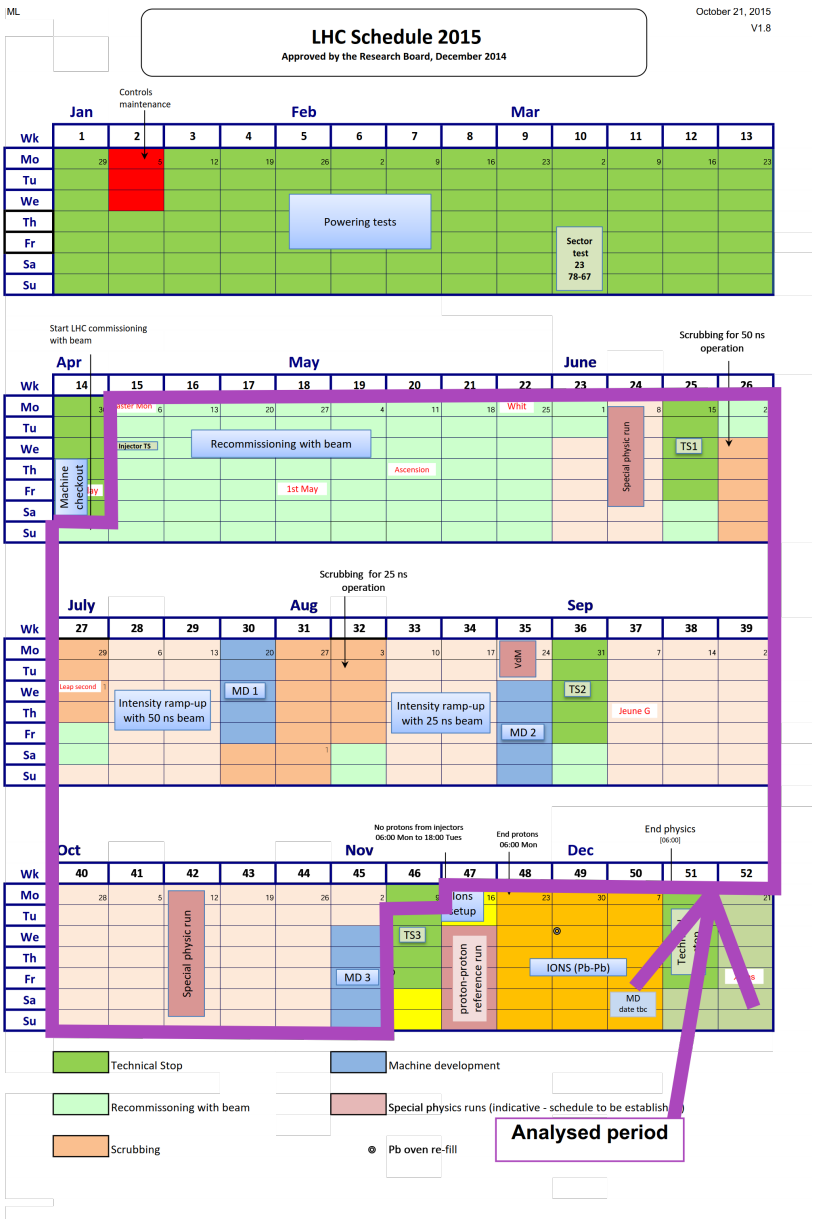

Figure 43: LHC Schedule for 2015 [18].

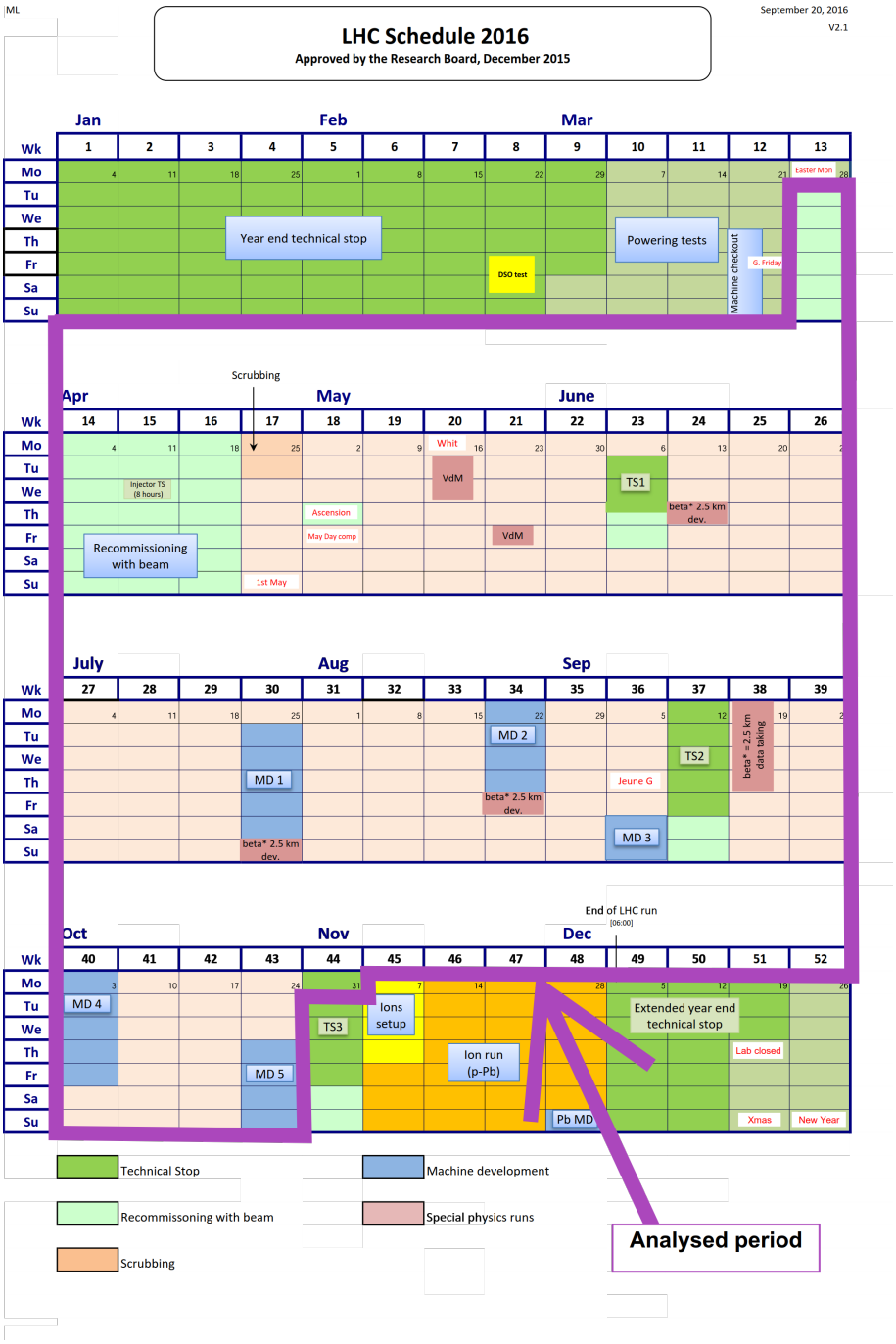

Figure 44: LHC Schedule for 2016 [19].

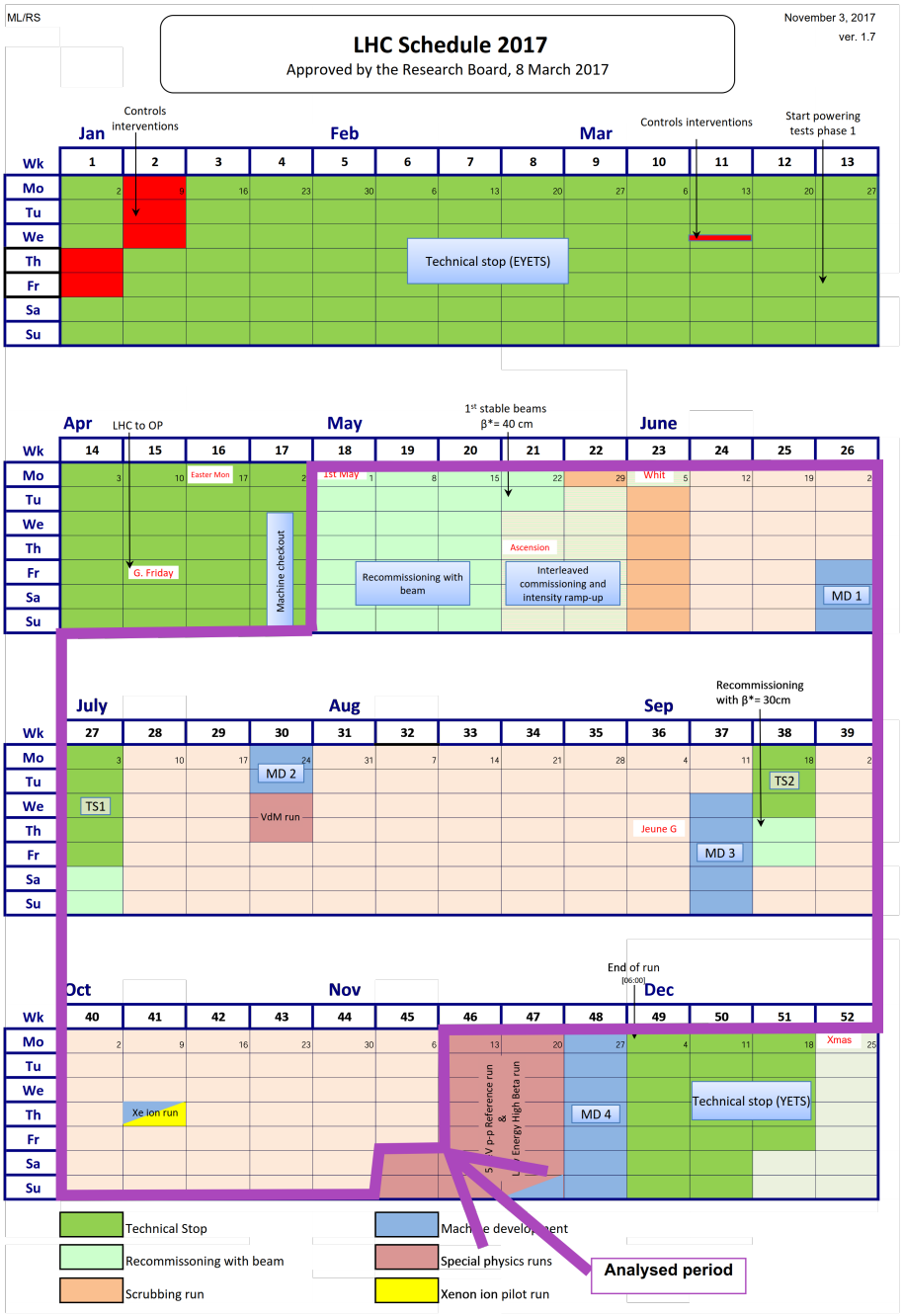

Figure 45: LHC Schedule for 2017 [20].

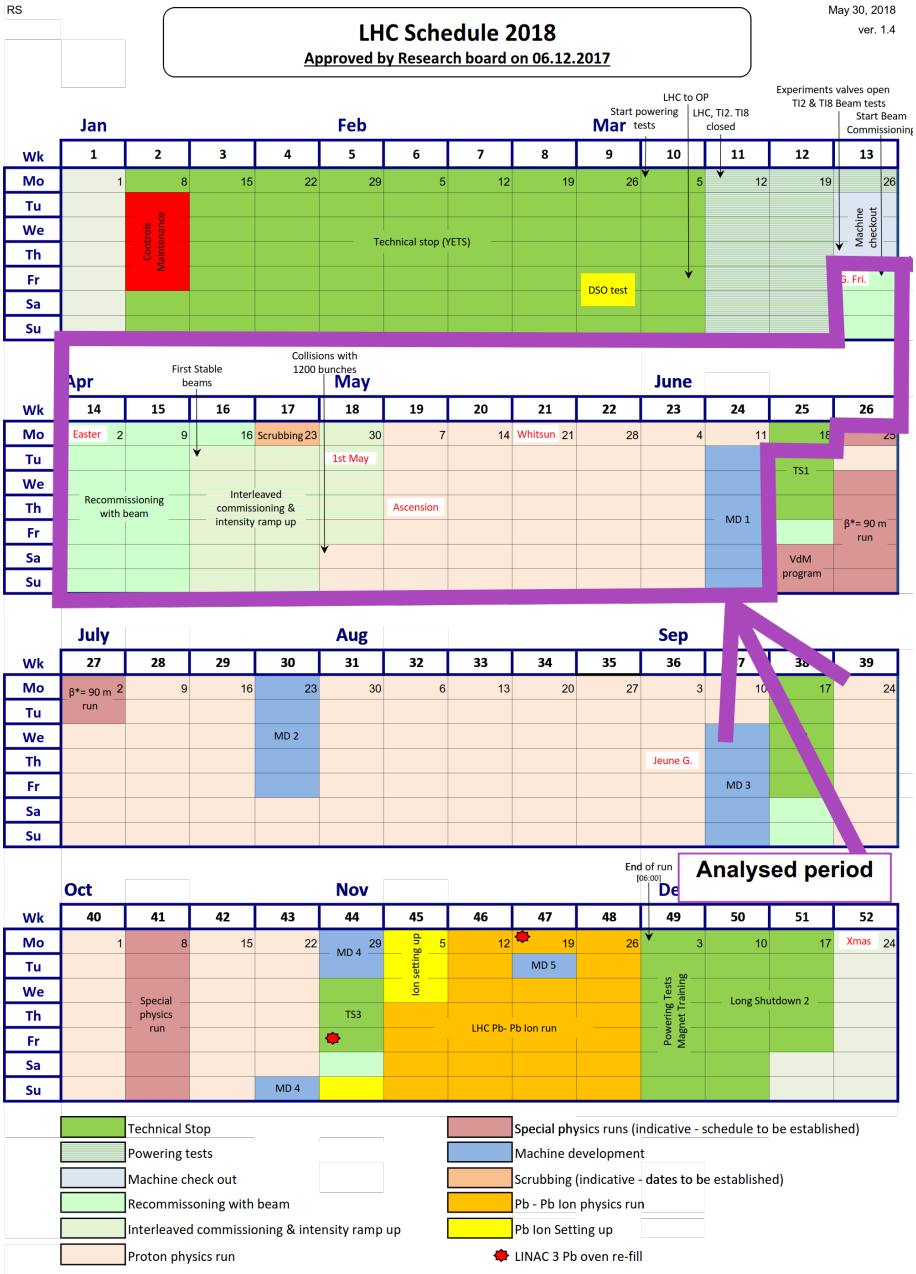

Figure 46: LHC Schedule for 2018 [21].

B. The arc sections dose distribution

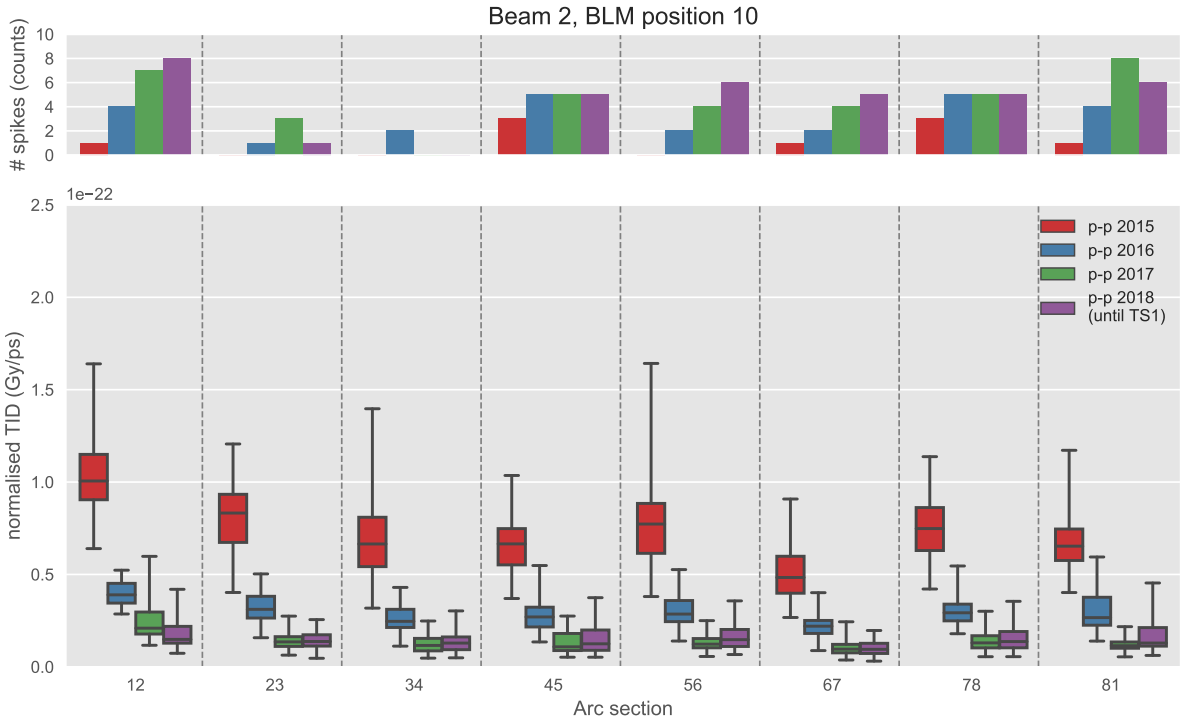

Figure 47: Box plot of the total normalised integrated dose rate for years 2015-2018. Only beam 2 BLMs with position 10 considered.

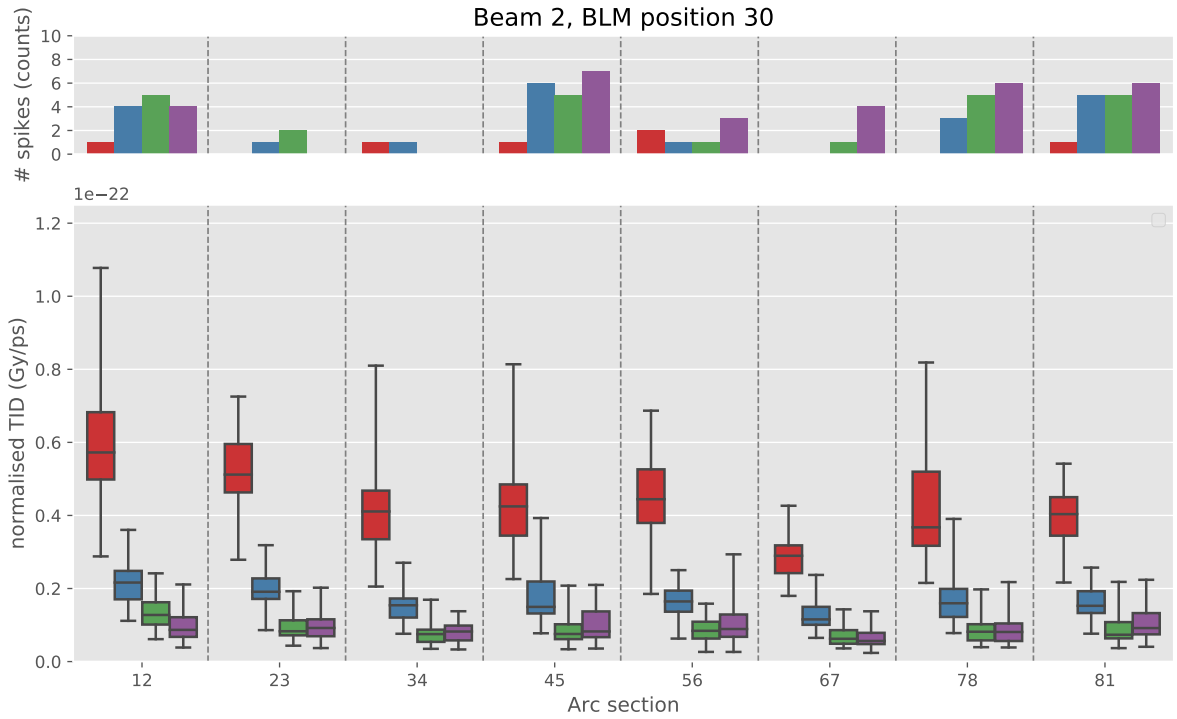

Figure 48: Box plot of the total normalised integrated dose rate for years 2015-2018. Only beam 2 BLMs with position 30 considered.

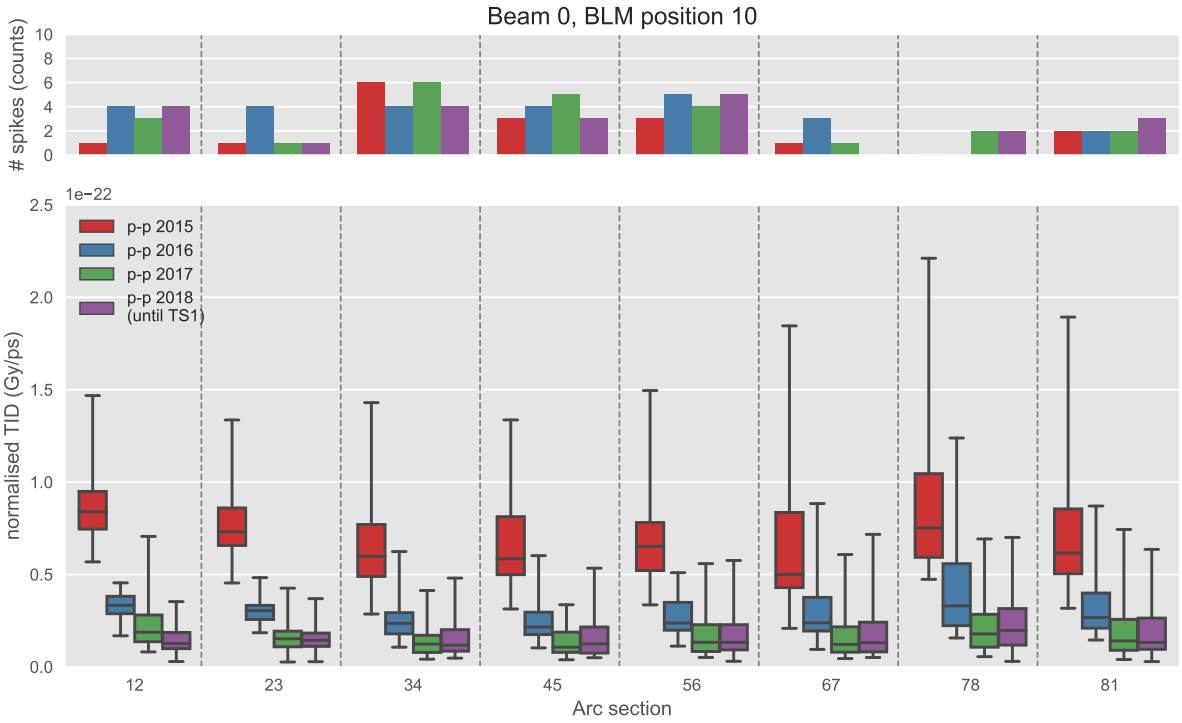

Figure 49: Box plot of the total normalised integrated dose rate for years 2015-2018. Only top BLMs with position 10 considered.

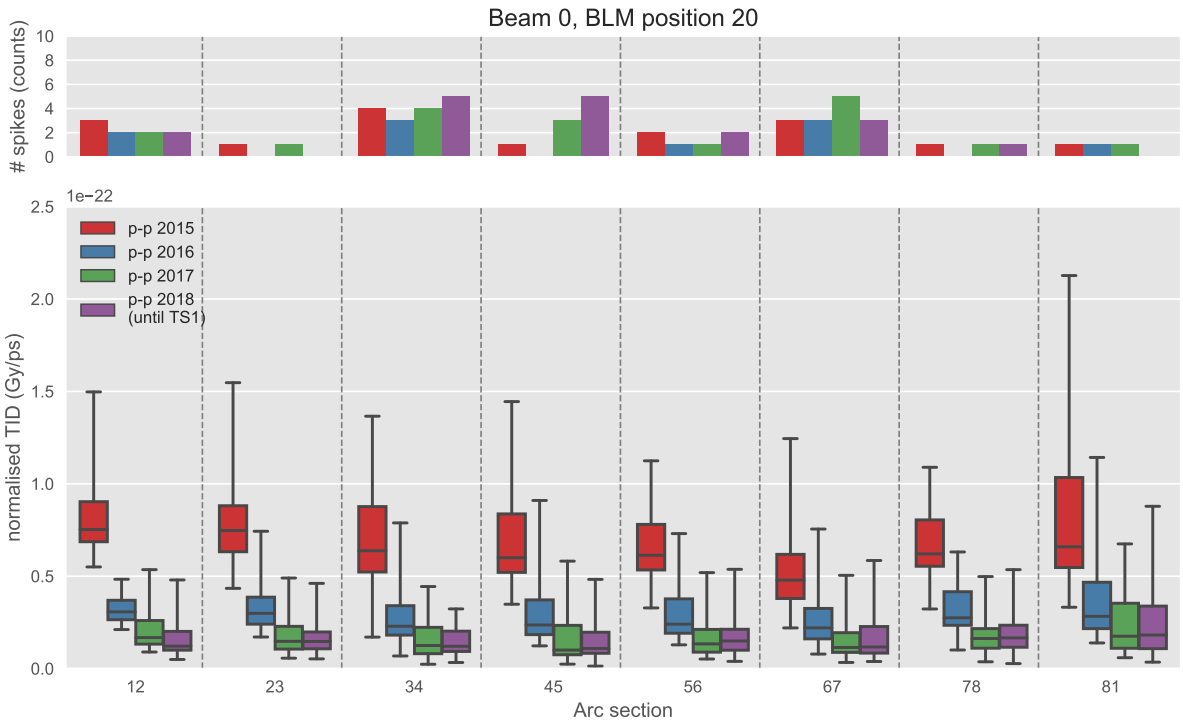

Figure 50: Box plot of the total normalised integrated dose rate for years 2015-2018. Only top BLMs with position 20 considered.

C. Baseline

C.1. Baseline normalised dose levels

Table 4: Total integrated dose baseline levels (with the standard deviation) for different years, normalised with integrated intensities. Only B1 and 30 position's BLMs considered.

ARC	2015	2016	2017	2018	unit
12	4.46±0.51	1.60±0.17	0.85±0.11	0.56±0.12	10^{-23} Gy/ps
23	3.69±0.50	1.28±0.19	0.614±0.092	0.57±0.13	10^{-23} Gy/ps
34	2.81±0.43	0.92±0.15	0.444±0.079	0.429±0.078	10^{-23} Gy/ps
45	2.91±0.47	0.90±0.13	0.404±0.065	0.405±0.081	10^{-23} Gy/ps
56	3.64±0.53	1.19±0.18	0.511±0.077	0.52±0.11	10^{-23} Gy/ps
67	2.37±0.36	0.90±0.14	0.469±0.046	0.427±0.047	10^{-23} Gy/ps
78	3.14±0.48	1.11±0.16	0.552±0.092	0.54±0.11	10^{-23} Gy/ps
81	3.12±0.47	1.05±0.19	0.518±0.094	0.57±0.12	10^{-23} Gy/ps

Table 5: Total integrated dose baseline levels (with the standard deviation) for different years, normalised with integrated intensities. Only B2 and 10 position's BLMs considered.

ARC	2015	2016	2017	2018	unit
12	8.83±0.98	3.39±0.31	1.71±0.27	1.21±0.22	10^{-23} Gy/ps
23	6.5±1.2	2.51±0.47	1.06±0.20	1.05±0.25	10^{-23} Gy/ps
34	5.32±0.87	2.02±0.32	0.85±0.17	0.93±0.20	10^{-23} Gy/ps
45	5.43±0.85	2.08±0.29	0.83±0.14	0.88±0.20	10^{-23} Gy/ps
56	6.05±0.96	2.37±0.38	1.00±0.18	1.13±0.20	10^{-23} Gy/ps
67	3.95±0.68	1.74±0.32	0.72±0.15	0.71±0.16	10^{-23} Gy/ps
78	6.0±1.1	2.41±0.42	1.00±0.21	1.00±0.23	10^{-23} Gy/ps
81	5.42±0.81	2.12±0.39	0.92±0.16	1.03±0.20	10^{-23} Gy/ps

Table 6: Total integrated dose baseline levels (with the standard deviation) for different years, normalised with integrated intensities. Only B2 and 30 position's BLMs considered.

ARC	2015	2016	2017	2018	unit
12	4.82±0.67	1.70±0.24	0.98±0.18	0.62±0.13	10^{-23} Gy/ps
23	4.26±0.78	1.56±0.31	0.68±0.12	0.66±0.15	10^{-23} Gy/ps
34	3.18±0.52	1.15±0.23	0.55±0.13	0.56±0.14	10^{-23} Gy/ps
45	3.36±0.64	1.25±0.19	0.57±0.12	0.62±0.12	10^{-23} Gy/ps
56	3.63±0.70	1.28±0.26	0.62±0.13	0.66±0.15	10^{-23} Gy/ps
67	2.35±0.37	0.96±0.15	0.478±0.080	0.437±0.088	10^{-23} Gy/ps
78	3.15±0.39	1.20±0.18	0.58±0.11	0.58±0.13	10^{-23} Gy/ps
81	3.26±0.48	1.26±0.24	0.58±0.11	0.69±0.16	10^{-23} Gy/ps

Table 7: Total integrated dose baseline levels (with the standard deviation) for different years, normalised with integrated intensities. Only B0 and 10 position's BLMs considered.

ARC	2015	2016	2017	2018	unit
12	7.21±0.78	2.80±0.43	1.36±0.24	0.88±0.30	10^{-23} Gy/ps
23	6.39±0.73	2.52±0.30	1.02±0.33	1.02±0.32	10^{-23} Gy/ps
34	4.75±0.77	1.75±0.31	0.81±0.21	0.87±0.22	10^{-23} Gy/ps
45	4.79±0.77	1.68±0.33	0.77±0.17	0.80±0.22	10^{-23} Gy/ps
56	5.06±0.89	1.84±0.36	0.87±0.24	0.92±0.26	10^{-23} Gy/ps
67	4.10±0.74	1.79±0.39	0.82±0.23	0.82±0.20	10^{-23} Gy/ps
78	5.90±0.82	2.19±0.38	1.14±0.37	1.14±0.41	10^{-23} Gy/ps
81	4.99±0.74	2.05±0.33	0.89±0.25	0.85±0.30	10^{-23} Gy/ps

Table 8: Total integrated dose baseline levels (with the standard deviation) for different years, normalised with integrated intensities. Only B0 and 20 position's BLMs considered.

ARC	2015	2016	2017	2018	unit
12	6.77±0.50	2.66±0.26	1.30±0.21	0.92±0.21	10^{-23} Gy/ps
23	6.26±0.77	2.42±0.33	1.05±0.28	1.04±0.29	10^{-23} Gy/ps
34	4.8±1.0	1.73±0.40	0.76±0.25	0.87±0.22	10^{-23} Gy/ps
45	5.09±0.62	1.81±0.29	0.73±0.20	0.76±0.26	10^{-23} Gy/ps
56	5.15±0.80	1.88±0.32	0.87±0.23	0.99±0.28	10^{-23} Gy/ps
67	3.77±0.70	1.53±0.34	0.81±0.22	0.84±0.22	10^{-23} Gy/ps
78	5.18±0.80	2.25±0.42	1.06±0.35	1.03±0.40	10^{-23} Gy/ps
81	5.42±0.77	2.12±0.38	1.11±0.34	1.10±0.37	10^{-23} Gy/ps

C.2. Baseline not-normalised dose levels

Table 9: Total integrated dose baseline levels for different years with the standard error. Only B1 and 10 position's BLMs considered.

ARC	2015	2016	2017	2018 (until 19 June)	unit
12	77.5±2.5	98.8±3.4	49.4±1.8	14.34±0.58	mGy
23	71.9±2.8	84.1±3.7	33.6±1.6	14.51±0.66	mGy
34	47.1±1.9	61.2±2.3	25.3±1.1	10.88±0.44	mGy
45	54.3±1.5	67.3±2.3	27.3±1.1	11.84±0.54	mGy
56	62.2±2.0	75.1±2.1	28.99±0.74	13.28±0.49	mGy
67	34.1±1.3	50.1±1.8	22.50±0.99	9.36±0.42	mGy
78	51.3±1.7	69.1±2.0	25.69±0.89	11.53±0.35	mGy
81	57.1±1.7	72.5±2.7	28.1±1.4	13.37±0.59	mGy

Table 10: Total integrated dose baseline levels for different years with the standard error. Only B1 and 30 position's BLMs considered.

ARC	2015	2016	2017	2018 (until 19 June)	unit
12	31.94±0.78	41.64±0.95	21.34±0.56	5.99±0.26	mGy
23	26.45±0.77	33.2±1.1	15.42±0.49	6.03±0.29	mGy
34	20.10±0.66	24.03±0.84	11.16±0.43	4.55±0.18	mGy
45	20.85±0.72	23.31±0.74	10.15±0.35	4.29±0.18	mGy
56	26.08±0.82	30.95±0.97	12.85±0.41	5.50±0.26	mGy
67	16.98±0.55	23.49±0.77	11.77±0.25	4.53±0.11	mGy
78	22.46±0.73	28.82±0.89	13.86±0.49	5.69±0.26	mGy
81	22.37±0.72	27.4±1.1	13.01±0.50	6.05±0.27	mGy

Table 11: Total integrated dose baseline levels for different years with the standard error. Only B2 and 10 position's BLMs considered.

ARC	2015	2016	2017	2018 (until 19 June)	unit
12	63.2±1.5	88.2±1.7	43.0±1.5	12.79±0.50	mGy
23	46.3±1.9	65.3±2.6	26.7±1.1	11.11±0.58	mGy
34	38.1±1.3	52.4±1.8	21.42±0.93	9.82±0.45	mGy
45	38.9±1.3	54.0±1.6	20.84±0.75	9.29±0.44	mGy
56	43.3±1.5	61.6±2.1	25.10±0.94	11.97±0.46	mGy
67	28.3±1.0	45.3±1.8	18.05±0.78	7.51±0.35	mGy
78	43.0±1.6	62.5±2.3	25.1±1.1	10.60±0.52	mGy
81	38.8±1.2	55.1±2.2	23.23±0.84	10.95±0.45	mGy

Table 12: Total integrated dose baseline levels for different years with the standard error. Only B2 and 30 position's BLMs considered.

ARC	2015	2016	2017	2018 (until 19 June)	unit
12	34.5±1.0	44.3±1.3	24.55±0.98	6.58±0.30	mGy
23	30.5±1.2	40.5±1.7	16.97±0.64	7.04±0.34	mGy
34	22.75±0.80	29.8±1.3	13.78±0.68	5.95±0.31	mGy
45	24.03±0.98	32.4±1.1	14.37±0.66	6.56±0.28	mGy
56	26.0±1.1	33.2±1.4	15.61±0.67	7.01±0.34	mGy
67	16.82±0.57	24.88±0.81	12.00±0.43	4.64±0.20	mGy
78	22.53±0.59	31.22±0.98	14.67±0.61	6.14±0.29	mGy
81	23.38±0.74	32.7±1.3	14.60±0.57	7.35±0.35	mGy

Table 13: Total integrated dose baseline levels for different years with the standard error. Only B0 and 10 position's BLMs considered.

ARC	2015	2016	2017	2018 (until 19 June)	unit
12	51.6±1.2	72.7±2.3	34.2±1.3	9.29±0.66	mGy
23	45.8±1.1	65.5±1.7	25.7±1.7	10.85±0.70	mGy
34	34.0±1.1	45.4±1.7	20.4±1.1	9.22±0.48	mGy
45	34.3±1.1	43.8±1.8	19.29±0.88	8.45±0.48	mGy
56	36.2±1.3	47.9±2.0	21.9±1.3	9.75±0.57	mGy
67	29.3±1.1	46.5±2.1	20.5±1.2	8.75±0.45	mGy
78	42.3±1.2	57.0±2.1	28.7±2.0	12.08±0.91	mGy
81	35.7±1.1	53.3±1.8	22.3±1.3	9.02±0.66	mGy

Table 14: Total integrated dose baseline levels for different years with the standard error. Only B0 and 20 position's BLMs considered.

ARC	2015	2016	2017	2018 (until 19 June)	unit
12	48.48±0.74	69.1±1.4	32.7±1.1	9.73±0.48	mGy
23	44.9±1.1	63.0±1.8	26.4±1.5	10.99±0.65	mGy
34	34.4±1.5	45.0±2.2	19.1±1.3	9.25±0.48	mGy
45	36.42±0.93	47.2±1.5	18.4±1.0	8.01±0.58	mGy
56	36.9±1.2	48.8±1.8	21.7±1.2	10.50±0.62	mGy
67	27.0±1.0	39.7±1.9	20.5±1.2	8.93±0.48	mGy
78	37.1±1.2	58.4±2.3	26.7±1.9	10.88±0.88	mGy
81	38.8±1.1	55.1±2.1	27.9±1.8	11.62±0.82	mGy

C.3. Baseline beam modes contribution

Table 15: Percentage contribution of selected beam modes to the baseline for all arcs and all BLM families for the years 2015 and 2016 with the standard deviation.

	2015				2016			
	inj. (%)	ramp (%)	squ. (%)	col. (%)	inj. (%)	ramp (%)	squ. (%)	col. (%)
ARC12								
B1_10	6.7±1.5	2.04±0.27	4.81±0.36	84.0±2.0	1.97±0.97	1.72±0.34	5.79±0.61	88.7±1.8
B1_30	11.2±2.4	2.78±0.35	5.12±0.44	77.9±3.0	4.1±1.5	2.19±0.52	6.13±0.77	85.5±2.8
B2_10	5.3±1.1	2.06±0.30	4.90±0.33	85.3±1.6	2.00±0.66	1.62±0.30	5.53±0.32	89.2±1.2
B2_30	11.4±1.3	3.03±0.39	5.08±0.40	77.9±1.9	3.79±0.65	2.29±0.32	6.06±0.62	85.8±1.5
B0_10	5.7±1.4	2.28±0.54	5.24±0.66	83.9±1.9	2.2±1.3	1.76±0.56	5.81±0.45	88.3±2.2
B0_20	5.56±0.97	2.20±0.30	5.00±0.59	84.5±1.6	2.01±0.53	1.60±0.30	5.54±0.45	89.0±1.0
ARC23								
B1_10	11.0±8.7	2.28±0.30	4.64±0.65	79.6±7.8	3.9±3.7	1.94±0.59	5.75±0.58	86.6±3.9
B1_30	14.4±4.9	3.34±0.96	5.8±1.4	72.7±6.6	6.1±2.8	2.7±1.1	6.4±1.2	82.6±5.2
B2_10	7.1±1.3	2.63±0.78	5.40±0.81	81.8±2.8	3.2±1.0	2.19±0.93	5.76±0.79	87.0±2.4
B2_30	12.4±2.2	3.41±0.66	5.23±0.78	75.9±3.1	4.6±1.4	2.6±1.0	6.04±0.82	84.8±3.1
B0_10	6.9±2.4	2.73±0.87	5.91±0.94	80.6±4.4	3.1±1.6	1.98±0.75	6.42±0.66	86.4±3.0
B0_20	7.6±2.3	2.81±0.73	6.4±1.3	79.1±4.3	3.6±1.6	2.15±0.75	6.72±0.98	85.3±3.4
ARC34								
B1_10	8.3±1.5	3.6±1.8	4.76±0.36	80.7±2.6	2.8±1.1	3.4±3.0	5.80±0.61	86.0±3.1
B1_30	14.3±2.1	3.55±0.62	5.61±0.41	72.7±2.5	6.4±1.7	2.73±0.83	6.43±0.47	82.1±2.4
B2_10	7.6±1.5	2.85±0.64	5.13±0.56	81.5±2.5	2.96±0.77	1.79±0.36	5.71±0.30	87.6±1.2
B2_30	13.6±1.6	3.23±0.39	5.32±0.52	74.7±2.3	5.2±1.3	2.46±0.35	6.01±0.65	84.1±2.1
B0_10	8.2±3.2	3.20±0.89	5.37±0.80	80.0±4.5	3.4±1.3	2.02±0.47	6.41±0.58	86.2±1.9
B0_20	7.8±4.5	3.20±0.95	5.31±0.73	80.5±5.1	3.5±2.7	2.15±0.94	6.58±0.71	85.7±4.0
ARC45								
B1_10	8.7±1.1	2.48±0.27	4.80±0.28	81.2±1.4	2.60±0.49	1.89±0.36	5.97±0.45	87.6±1.2
B1_30	16.1±3.3	3.51±0.46	6.11±0.57	70.2±4.3	7.1±1.8	2.78±0.44	6.91±0.77	80.8±2.9
B2_10	8.7±2.0	2.60±0.50	5.32±0.59	80.3±3.0	3.1±1.2	1.80±0.33	6.03±0.96	87.2±2.5
B2_30	14.7±2.5	3.25±0.48	5.50±0.48	73.3±3.3	4.83±0.80	2.33±0.41	6.28±0.91	84.5±2.0
B0_10	9.0±2.1	3.15±0.96	5.57±0.76	79.1±2.9	3.6±1.6	2.10±0.65	6.28±0.85	85.9±2.7
B0_20	9.7±3.1	2.70±0.56	5.73±0.89	78.2±3.8	3.1±1.3	1.80±0.32	6.19±0.77	86.8±2.2
ARC56								
B1_10	8.9±1.2	2.42±0.55	4.94±0.43	81.2±1.6	2.48±0.87	1.87±0.28	5.76±0.48	88.0±1.3
B1_30	16.0±2.3	3.42±0.51	5.84±0.62	71.1±3.6	5.7±1.6	2.73±0.56	6.80±0.79	82.5±2.9
B2_10	10.6±4.1	2.62±0.67	5.12±0.53	79.1±5.0	2.9±1.3	1.72±0.42	5.63±0.70	88.0±2.4
B2_30	17.5±2.7	3.75±0.74	5.79±0.75	69.7±4.0	5.5±1.7	2.64±0.57	6.22±0.87	83.4±3.1
B0_10	11.6±3.3	3.3±1.1	5.48±0.84	76.6±3.4	3.2±1.4	2.20±0.93	5.89±0.63	86.8±2.5
B0_20	11.6±3.1	3.5±1.6	5.49±0.82	76.4±4.1	3.4±1.3	2.20±0.73	5.97±0.87	86.5±2.3
ARC67								
B1_10	11.0±2.0	2.75±0.57	4.82±0.46	78.6±2.4	3.37±0.98	1.89±0.32	5.89±0.46	86.9±1.5
B1_30	17.1±2.9	3.27±0.58	5.51±0.81	70.5±3.5	6.3±1.2	2.66±0.51	6.41±0.85	82.2±2.3
B2_10	11.3±2.3	3.2±1.8	5.3±1.1	77.2±3.4	3.7±1.3	2.00±0.50	5.82±0.53	86.5±2.1
B2_30	18.7±3.7	3.85±0.76	5.66±0.78	68.3±4.1	6.6±1.8	2.64±0.44	6.32±0.57	82.3±2.5
B0_10	11.2±2.8	3.9±3.0	5.72±0.67	75.7±5.0	3.2±1.3	1.91±0.57	6.49±0.63	86.1±1.9
B0_20	11.8±4.8	3.5±1.1	5.48±0.87	76.0±5.8	4.3±2.0	2.37±0.82	6.42±0.73	84.8±3.0
ARC78								
B1_10	8.4±3.7	2.21±0.43	4.73±0.58	81.9±4.2	2.36±0.42	1.62±0.21	5.68±0.29	88.57±0.76
B1_30	14.0±3.3	2.91±0.37	4.93±0.42	75.0±3.3	5.4±1.4	2.12±0.44	6.05±0.54	84.4±2.1
B2_10	8.4±5.8	2.35±0.59	4.87±0.55	81.6±5.6	3.5±2.2	1.74±0.56	5.36±0.42	87.6±2.3
B2_30	15.1±4.8	3.05±0.47	5.05±0.49	73.9±4.9	5.3±1.5	2.20±0.38	5.83±0.59	84.7±2.1
B0_10	6.7±1.5	2.59±0.69	5.42±0.77	81.8±2.7	3.0±1.1	1.91±0.62	6.08±0.56	87.0±2.0
B0_20	8.6±4.2	3.02±0.99	5.01±0.60	80.3±5.0	3.3±2.6	1.83±0.89	5.81±0.69	87.2±3.8
ARC81								
B1_10	8.0±2.2	2.41±0.34	4.86±0.58	81.9±2.2	2.33±0.42	1.73±0.28	5.78±0.77	88.3±1.5
B1_30	13.2±2.4	3.06±0.38	5.50±0.69	74.7±3.1	5.6±1.8	2.23±0.53	6.24±0.85	83.8±3.1
B2_10	8.5±4.7	2.36±0.42	5.11±0.57	81.1±5.2	2.95±0.90	1.61±0.19	5.56±0.66	88.1±1.5
B2_30	13.9±4.4	3.14±0.49	5.17±0.77	74.7±5.3	4.6±1.6	2.09±0.51	5.64±0.77	85.7±2.8
B0_10	7.8±2.6	3.0±1.3	5.22±0.64	80.1±4.6	3.0±1.5	1.91±0.74	5.77±0.54	87.5±2.1
B0_20	6.7±2.1	2.60±0.54	5.39±0.89	82.2±3.1	3.0±1.5	1.78±0.56	5.79±0.95	87.5±2.6

Table 16: Percentage contribution of selected beam modes to the baseline for all arcs and all BLM families for the years 2017 and 2018 with the standard deviation.

	2017				2018			
	inj. (%)	ramp (%)	squ. (%)	col. (%)	inj. (%)	ramp (%)	squ. (%)	col. (%)
ARC12								
B1_10	5.6±1.3	2.25±0.31	3.29±0.35	87.4±1.8	5.4±1.8	2.40±0.31	5.00±0.66	85.3±2.5
B1_30	9.2±2.1	3.07±0.53	3.43±0.35	82.5±2.6	11.7±3.9	3.59±0.70	5.65±0.83	76.3±5.2
B2_10	5.0±2.1	2.29±0.45	3.25±0.25	87.9±2.7	5.5±2.2	2.35±0.46	4.62±0.62	85.6±3.0
B2_30	11.5±2.5	3.17±0.65	3.42±0.51	80.1±3.4	11.5±2.8	3.84±0.99	5.52±0.73	76.4±4.2
B0_10	5.5±1.8	2.70±0.72	3.37±0.41	86.7±2.7	8.3±5.9	3.2±1.5	5.3±1.1	80.7±7.8
B0_20	5.6±1.8	2.69±0.79	3.33±0.50	86.7±2.7	6.8±2.4	3.1±1.1	5.5±1.1	82.0±4.5
ARC23								
B1_10	10.1±5.3	2.60±0.50	3.45±0.43	82.2±5.2	10.4±4.9	2.94±0.64	4.95±0.76	79.7±5.4
B1_30	14.7±5.1	4.0±1.1	3.60±0.53	75.5±6.3	17.6±8.9	4.7±1.4	5.82±0.77	69±10
B2_10	8.6±2.1	3.3±1.4	3.45±0.46	83.0±3.6	8.6±3.5	4.0±2.6	5.13±0.90	79.7±6.3
B2_30	13.0±3.2	4.2±1.3	3.61±0.50	77.2±4.7	13.5±4.9	4.7±1.8	5.5±1.1	73.4±6.8
B0_10	8.9±6.2	3.4±2.4	3.82±0.49	81.8±8.5	9.6±6.2	3.6±1.6	6.4±1.1	76.9±8.1
B0_20	9.2±4.9	3.0±1.2	3.89±0.70	81.7±6.4	10.0±6.9	3.4±1.4	6.3±1.3	76.9±9.0
ARC34								
B1_10	6.8±2.2	3.5±2.2	3.43±0.35	84.6±4.0	7.3±2.6	5.0±4.2	5.16±0.76	80.6±6.2
B1_30	13.8±3.8	3.79±0.81	3.58±0.44	76.6±4.7	14.7±4.5	4.3±1.3	6.4±1.4	71.8±6.8
B2_10	7.3±2.0	2.62±0.60	3.35±0.33	85.0±2.6	6.7±2.5	2.86±0.74	5.06±0.89	83.2±3.8
B2_30	11.4±3.2	3.52±0.68	3.49±0.37	79.6±4.2	11.6±4.4	3.97±0.80	5.3±1.2	76.4±5.9
B0_10	7.1±3.2	2.45±0.92	3.52±0.31	85.1±3.7	5.9±2.7	3.2±1.3	5.68±0.86	82.8±4.4
B0_20	7.9±5.4	2.9±1.3	3.40±0.42	84.1±6.3	6.6±5.2	3.4±1.8	5.55±0.98	82.0±6.6
ARC45								
B1_10	6.1±1.3	2.24±0.38	3.47±0.52	86.6±2.2	6.3±2.1	2.85±0.57	5.15±0.55	83.8±2.8
B1_30	15.8±3.7	4.35±0.71	3.94±0.62	73.4±4.9	15.5±4.8	4.7±1.0	6.1±1.0	70.3±5.9
B2_10	8.2±3.5	2.77±0.74	3.66±0.49	83.4±4.7	7.4±3.6	2.80±0.83	5.03±0.74	82.7±5.4
B2_30	10.8±2.7	3.41±0.75	3.41±0.61	80.5±4.0	9.7±2.7	3.50±0.75	5.3±1.2	79.2±4.5
B0_10	7.9±2.6	3.07±0.89	3.96±0.65	82.9±3.6	7.4±3.1	3.3±1.0	5.9±1.2	80.9±4.9
B0_20	8.5±6.4	3.3±2.1	3.77±0.77	82.4±8.3	10±10	3.9±3.1	5.5±1.4	78±13
ARC56								
B1_10	6.4±1.7	2.51±0.37	3.65±0.38	85.6±2.4	5.5±1.4	2.79±0.42	5.20±0.70	84.6±2.2
B1_30	13.7±3.2	4.07±0.83	4.01±0.76	75.9±4.7	13.0±4.2	4.5±1.0	6.17±0.99	73.1±6.1
B2_10	8.5±4.3	2.60±0.69	3.56±0.51	83.6±5.0	6.7±2.7	2.73±0.71	4.95±0.69	83.7±3.7
B2_30	12.8±4.7	3.72±0.99	3.79±0.64	77.6±6.4	11.3±4.5	4.0±1.1	5.6±1.2	76.5±6.9
B0_10	7.3±2.8	2.51±0.64	3.56±0.73	84.8±3.6	5.7±2.6	2.97±0.95	5.7±1.3	83.2±4.9
B0_20	7.8±2.9	2.71±0.89	3.84±0.59	83.6±4.1	6.1±3.9	3.0±1.1	5.9±1.5	82.1±5.6
ARC67								
B1_10	9.4±3.2	2.71±0.62	3.12±0.42	83.0±4.2	9.7±4.2	2.95±0.80	4.89±0.78	80.5±5.1
B1_30	14.2±2.2	3.81±0.62	3.51±0.54	76.3±3.4	14.4±4.0	4.08±0.71	5.6±1.2	73.2±5.2
B2_10	9.9±3.1	2.88±0.67	3.35±0.48	81.6±4.7	9.1±3.6	2.87±0.78	4.91±0.98	80.9±5.4
B2_30	14.7±3.9	3.65±0.72	3.35±0.71	76.0±4.8	15.2±4.6	4.20±0.88	5.4±1.0	72.4±6.2
B0_10	9.3±3.4	2.8±1.0	3.38±0.58	82.5±4.3	7.5±3.1	2.8±1.3	4.97±0.85	82.4±3.8
B0_20	10.4±5.8	3.0±1.4	3.52±0.74	80.9±6.9	8.6±4.8	2.8±1.3	4.87±0.74	81.2±5.2
ARC78								
B1_10	8.6±3.8	2.28±0.39	3.52±0.51	83.9±4.0	7.3±2.7	2.54±0.30	5.20±0.59	83.0±3.1
B1_30	15.3±8.1	3.20±0.55	3.43±0.77	76.0±8.4	13.6±7.5	3.44±0.55	5.3±1.4	75.3±8.4
B2_10	11.9±6.9	2.59±0.70	3.24±0.56	80.6±6.8	7.8±3.4	2.85±0.96	4.83±0.66	82.3±4.7
B2_30	15.2±6.1	3.13±0.71	3.42±0.59	76.3±6.3	11.3±3.6	3.42±0.84	5.3±1.1	77.5±4.6
B0_10	7.0±3.4	2.47±0.87	3.54±0.52	85.1±4.2	6.8±4.6	2.8±1.5	5.6±1.2	82.3±6.9
B0_20	8.1±5.9	2.7±1.2	3.68±0.73	83.5±6.8	8.8±8.1	3.3±2.4	5.41±0.79	80±11
ARC81								
B1_10	7.0±3.3	2.9±2.7	3.40±0.45	85.1±5.3	6.0±1.9	3.7±4.9	4.77±0.54	83.6±6.0
B1_30	11.2±2.9	3.5±1.4	3.46±0.64	79.9±4.4	10.2±2.6	4.0±2.8	4.87±0.65	78.3±5.1
B2_10	6.5±2.1	2.34±0.56	3.22±0.47	86.3±2.8	6.2±1.9	2.51±0.74	4.50±0.69	84.9±2.9
B2_30	9.9±2.6	3.11±0.67	3.29±0.52	81.9±3.3	9.4±3.0	3.5±1.2	4.89±0.85	80.0±4.5
B0_10	7.6±4.1	2.8±1.0	3.74±0.70	83.8±5.7	8.3±6.7	3.9±2.7	5.7±1.0	80±10
B0_20	5.9±2.6	2.31±0.80	3.53±0.70	86.4±3.5	6.6±5.9	3.1±2.8	4.9±1.0	83.2±8.8

C.4. Baseline evolution

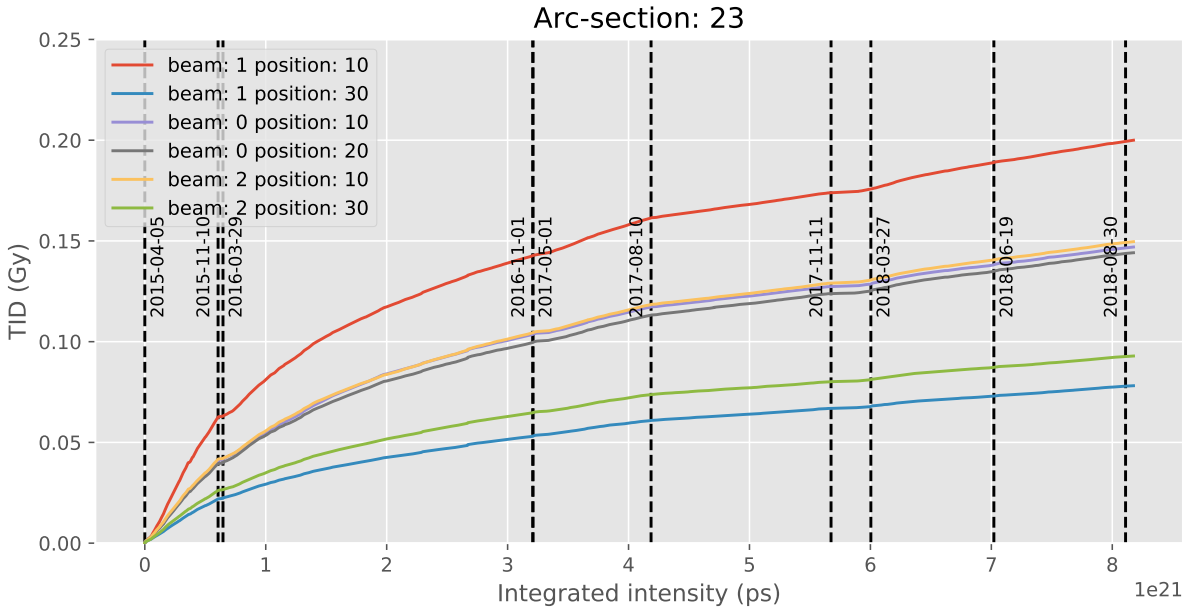

Figure 51: Evolution of the prompt dose baselines over integrated intensity for arc23 for all beam modes. Each BLM family is plotted separately.

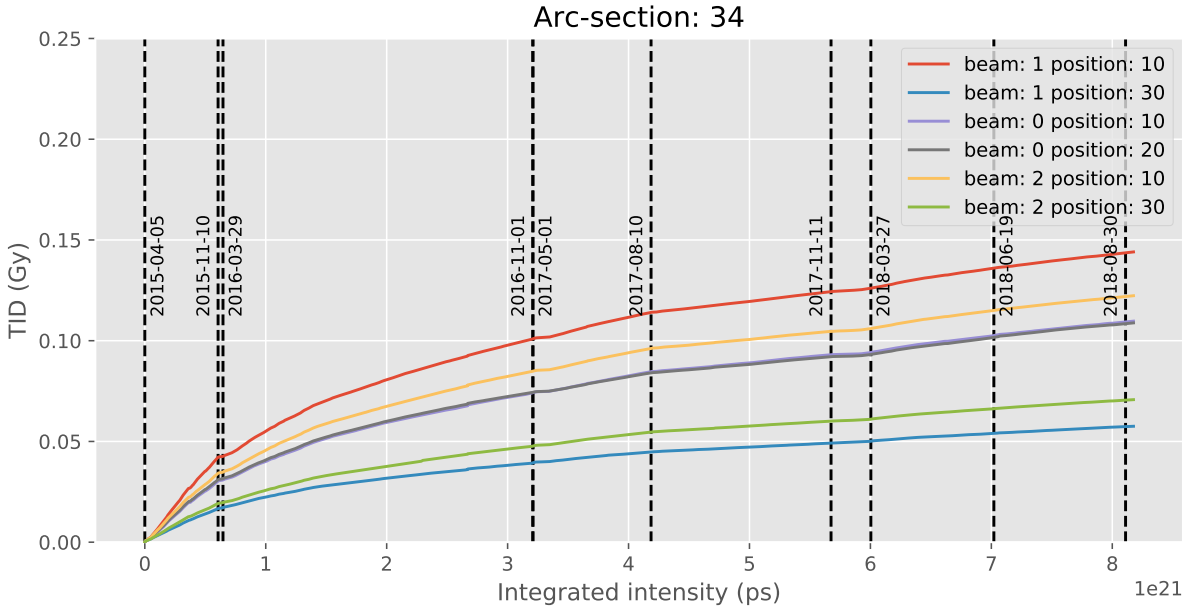

Figure 52: Evolution of the prompt dose baselines over integrated intensity for arc34 for all beam modes. Each BLM family is plotted separately.

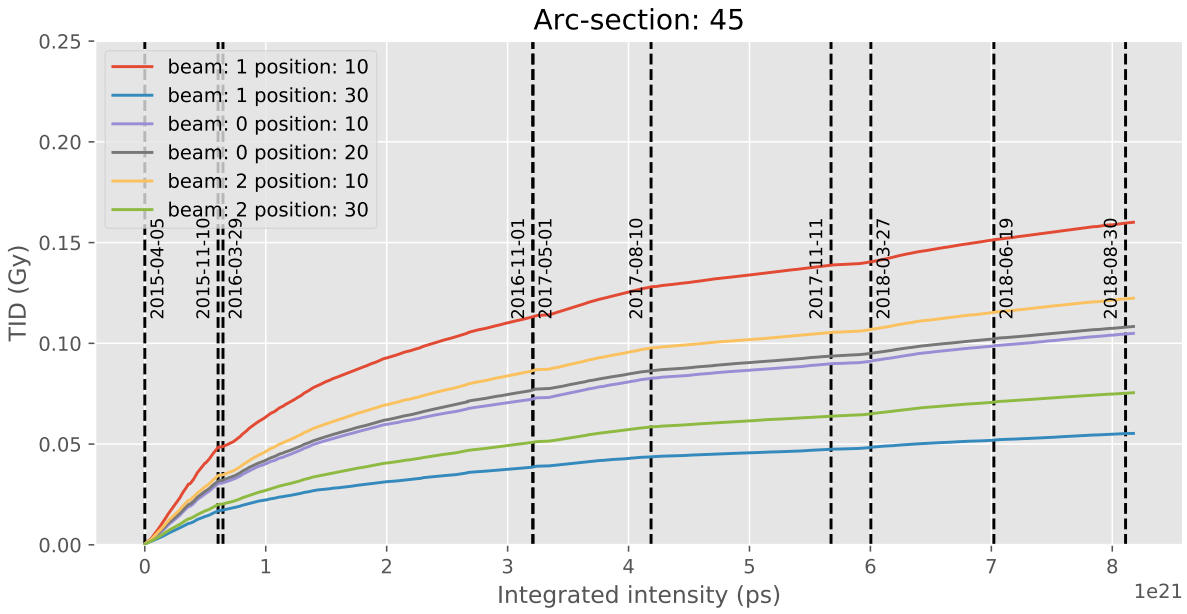

Figure 53: Evolution of the prompt dose baselines over integrated intensity for arc45 for all beam modes. Each BLM family is plotted separately.

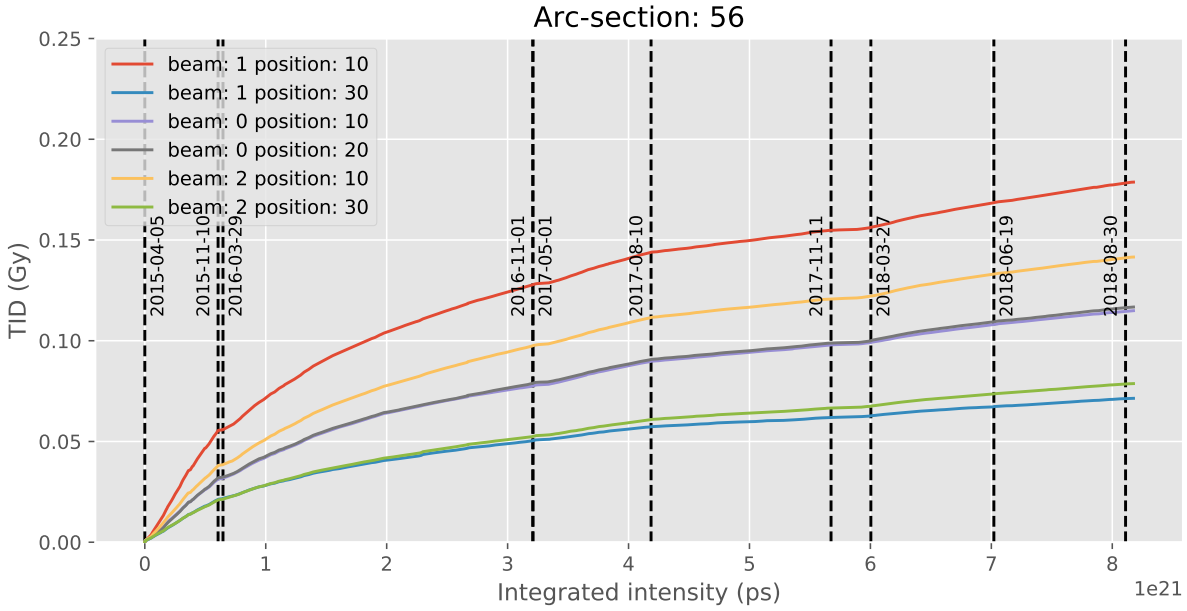

Figure 54: Evolution of the prompt dose baselines over integrated intensity for arc56 for all beam modes. Each BLM family is plotted separately.

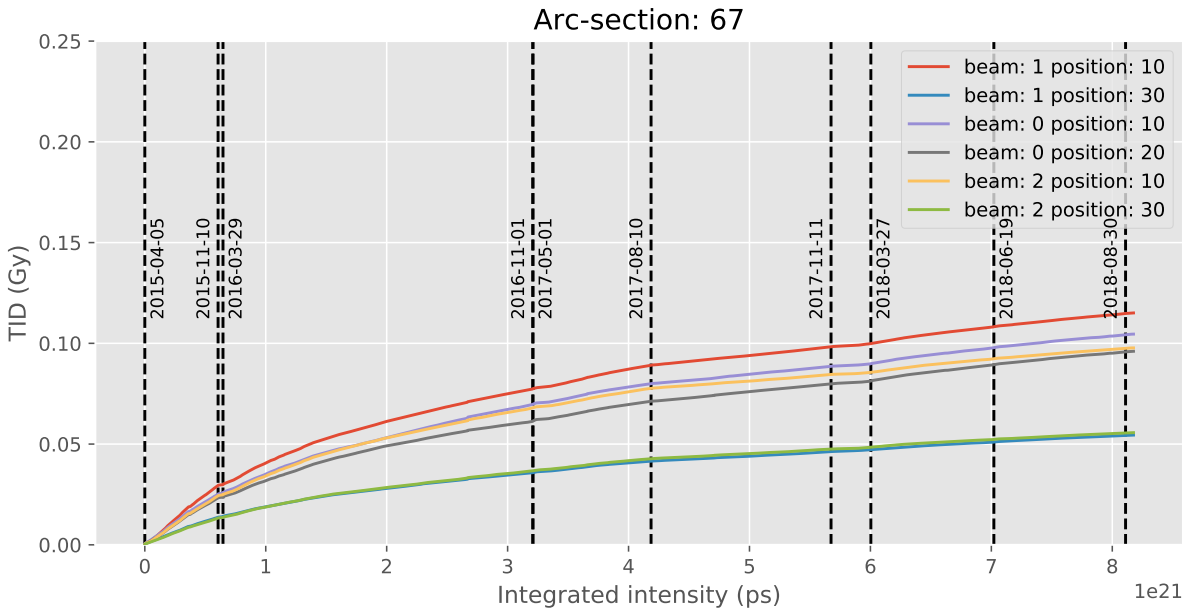

Figure 55: Evolution of the prompt dose baselines over integrated intensity for arc67 for all beam modes. Each BLM family is plotted separately.

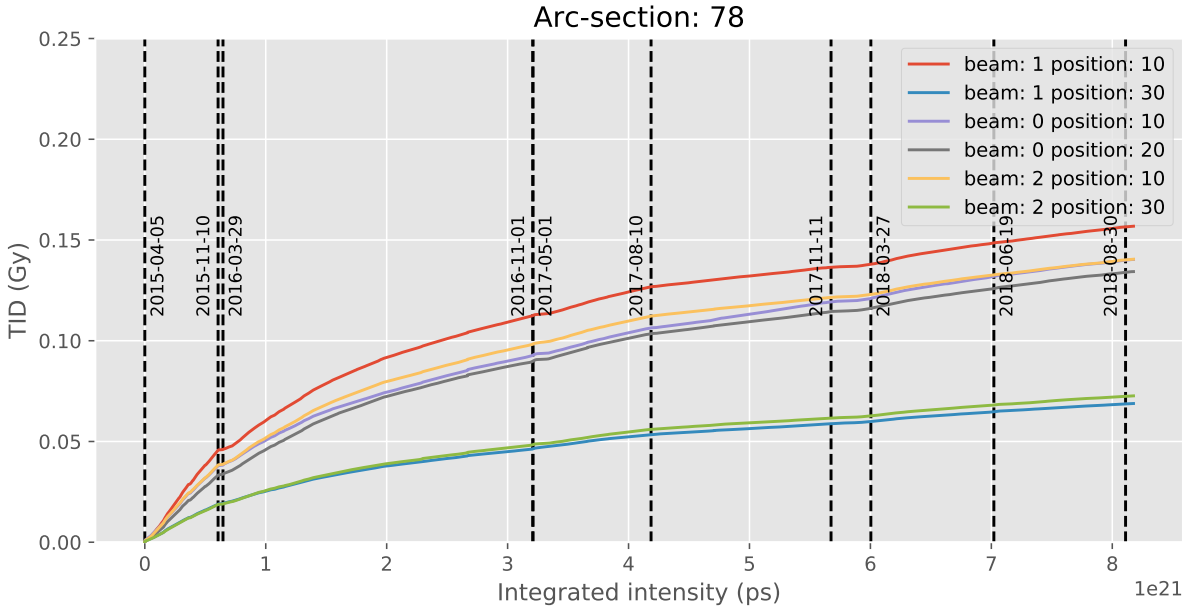

Figure 56: Evolution of the prompt dose baselines over integrated intensity for arc78 for all beam modes. Each BLM family is plotted separately.

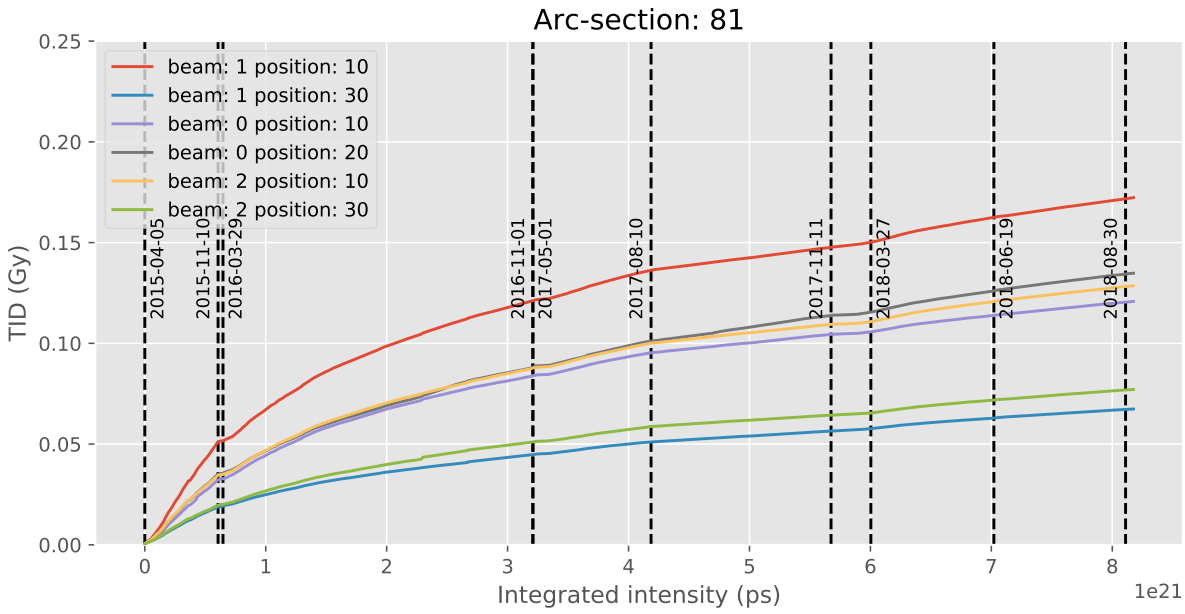

Figure 57: Evolution of the prompt dose baselines over integrated intensity for arc81 for all beam modes. Each BLM family is plotted separately.

C.5. FLUKA simulation

Table 17: Doses obtained using the FLUKA simulation for the idealised LHC arc cell normalised with integrated intensity and residual hydrogen gas density.

Beam	Position	Normalised dose (10^{-35} Gy/ps/(number of H_2 molecules per m^3))	Uncertainy (%)
1	10	1.495	2.8
1	30	0.441	5.7
2	10	1.495	2.8
2	30	0.441	5.7
0	10	1.035	4.5
0	20	1.035	4.5

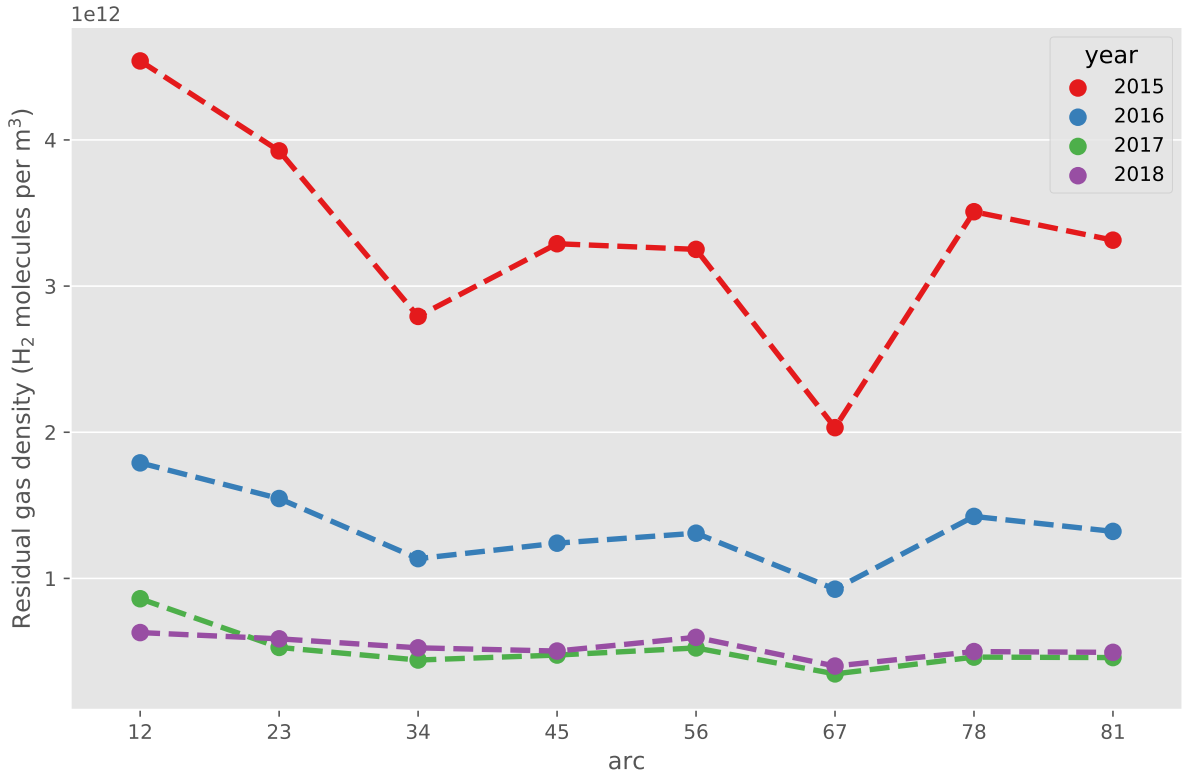

Figure 58: Estimations of the annual residual gas densities for all arc sections based on the baseline doses and the FLUKA simulation. It is assumed that residual dose is 0.

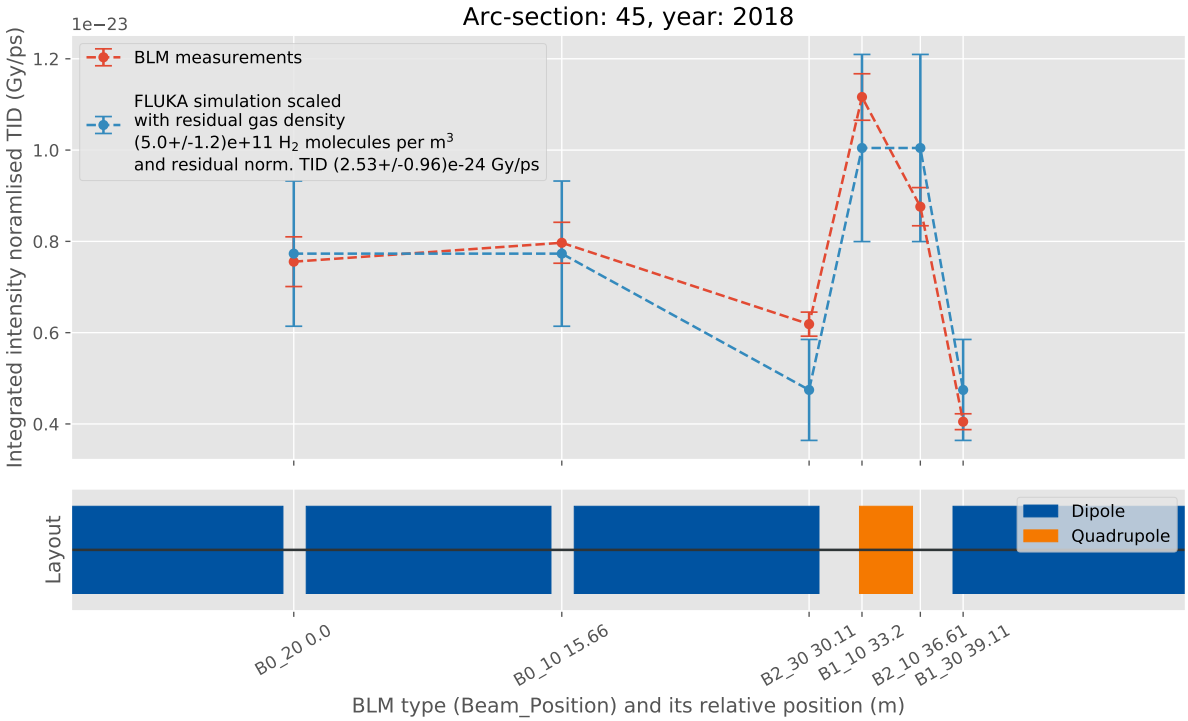

Figure 59: An example of the comparison between BLM measurements and the FLUKA simulation for the FODO cell. For the simulation scaling residual gas density in arc 45 in 2018 was used. Moreover, it is assumed that residual dose is 0.

D. Spikes

Figure 60: Spikes distribution in the LHC for different years. The radius and colour at the plot reflects the spike strength with respect to the highest spike in the top BLMs at the given year.

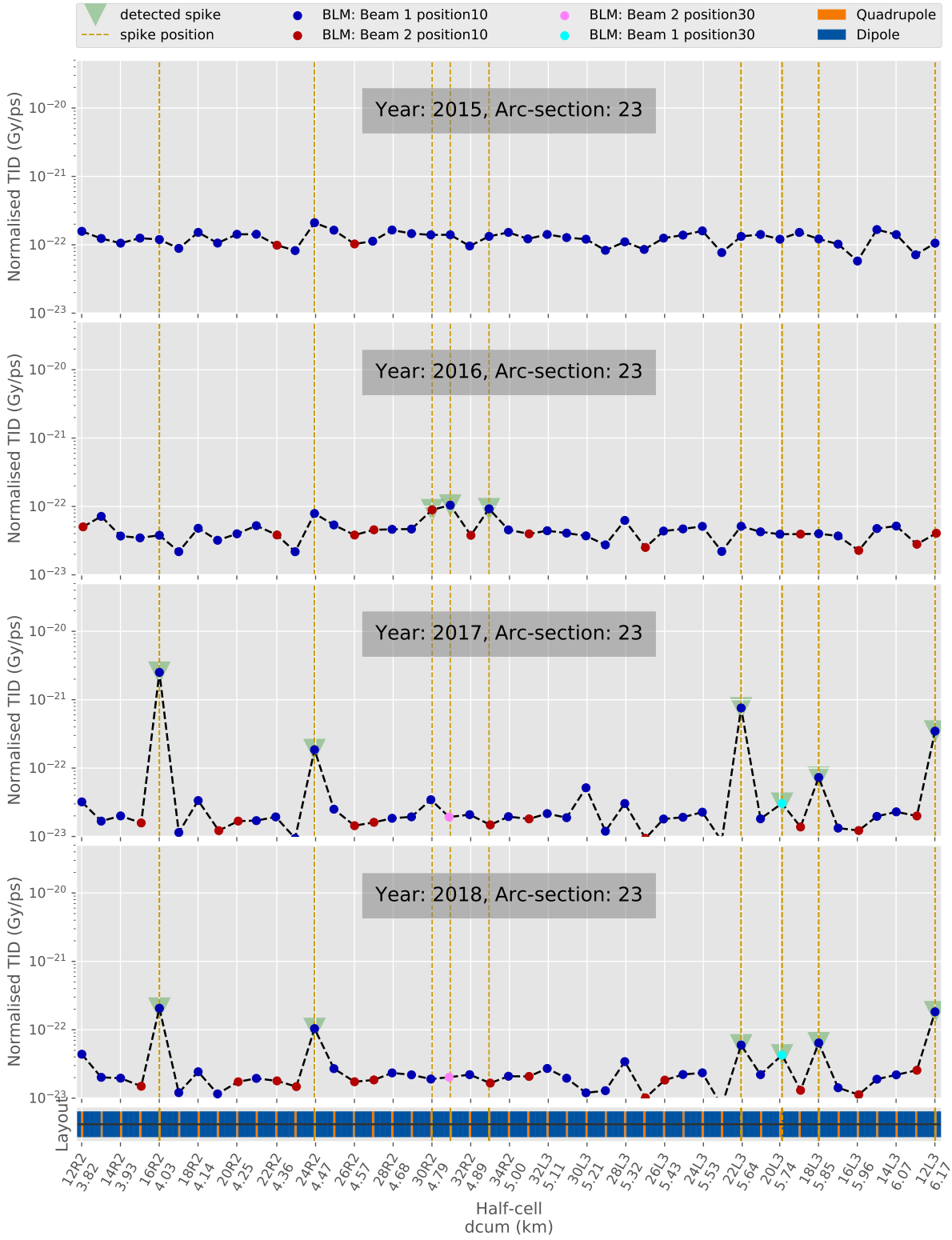

Figure 61: Normalised dose levels in the arc 23 for the years 2015-2018. Top BLMs are not considered and for each half-cell only BLM with highest dose is plotted.

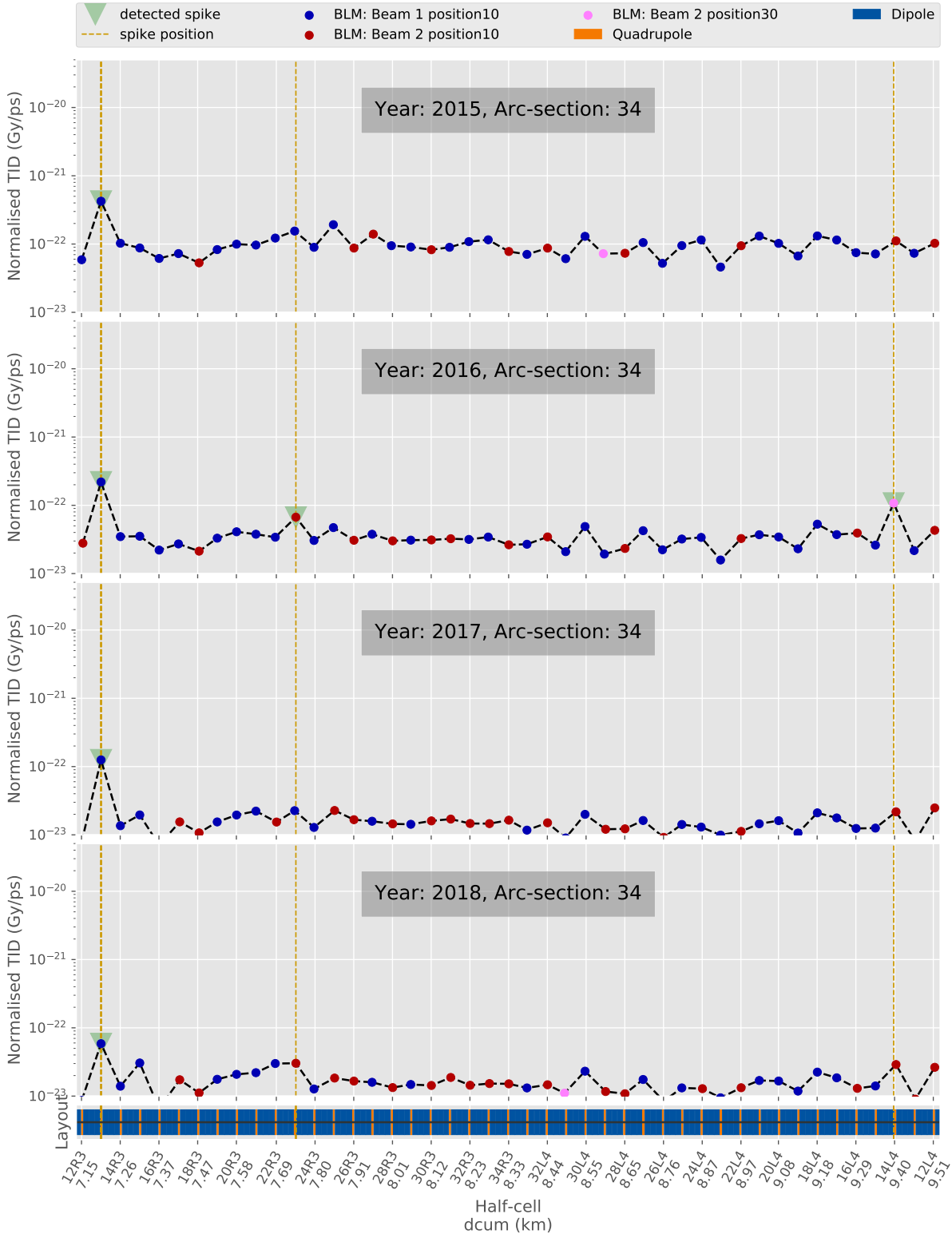

Figure 62: Normalised dose levels in the arc 34 for the years 2015-2018. Top BLMs are not considered and for each half-cell only BLM with highest dose is plotted.

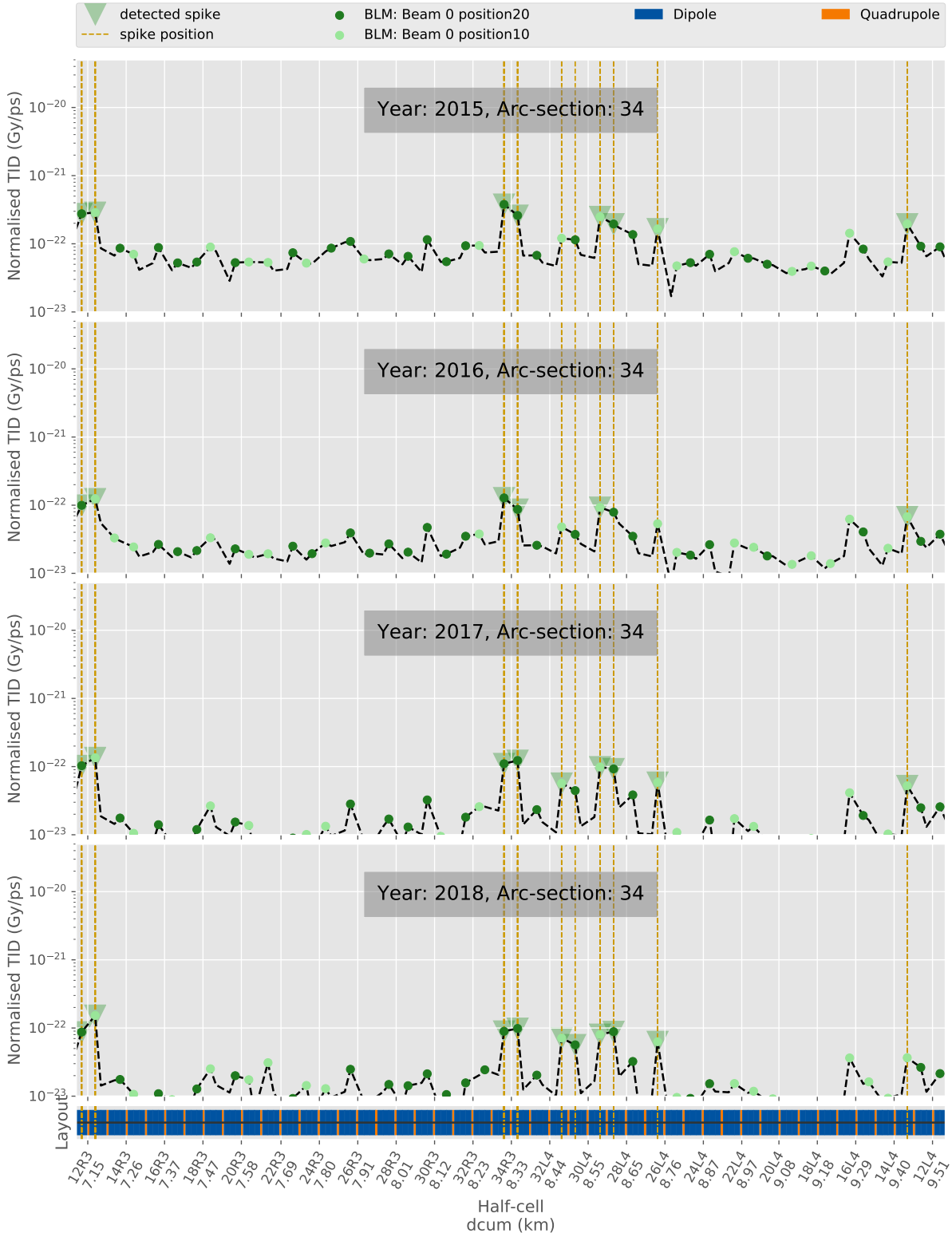

Figure 63: Normalised dose levels in the arc 34 for the years 2015-2018. Only top BLMs are considered.

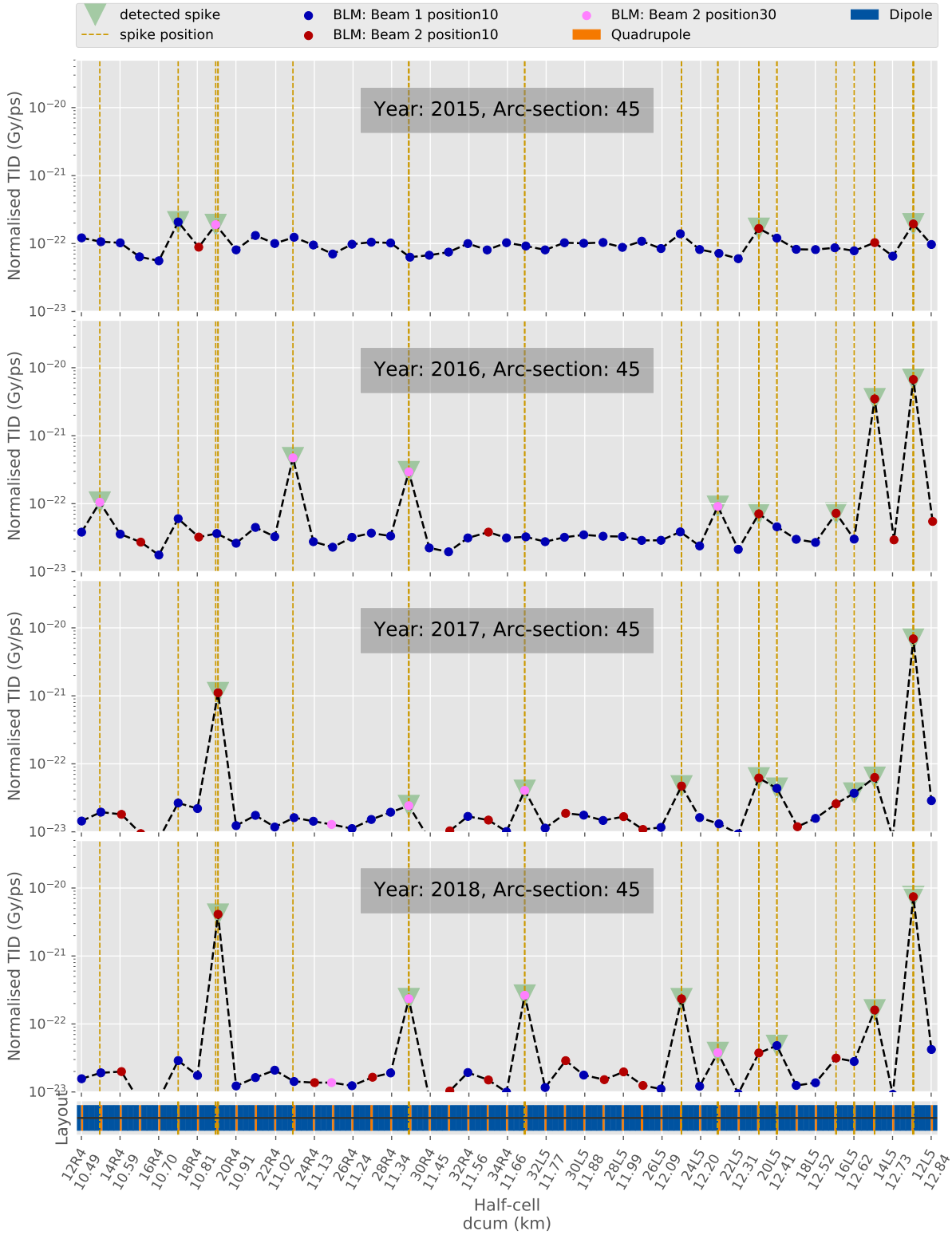

Figure 64: Normalised dose levels in the arc 45 for the years 2015-2018. Top BLMs are not considered and for each half-cell only BLM with highest dose is plotted.

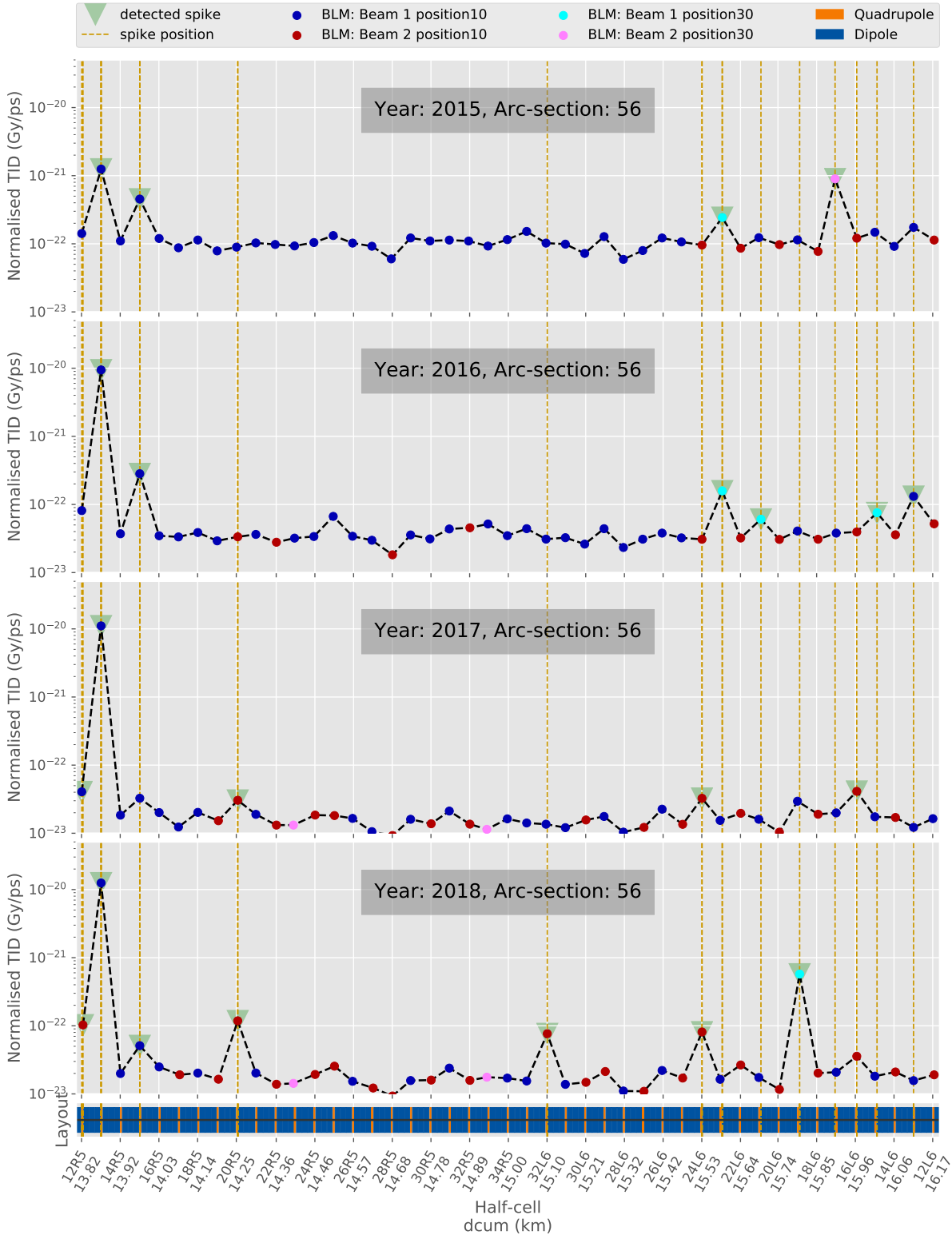

Figure 65: Normalised dose levels in the arc 56 for the years 2015-2018. Top BLMs are not considered and for each half-cell only BLM with highest dose is plotted.

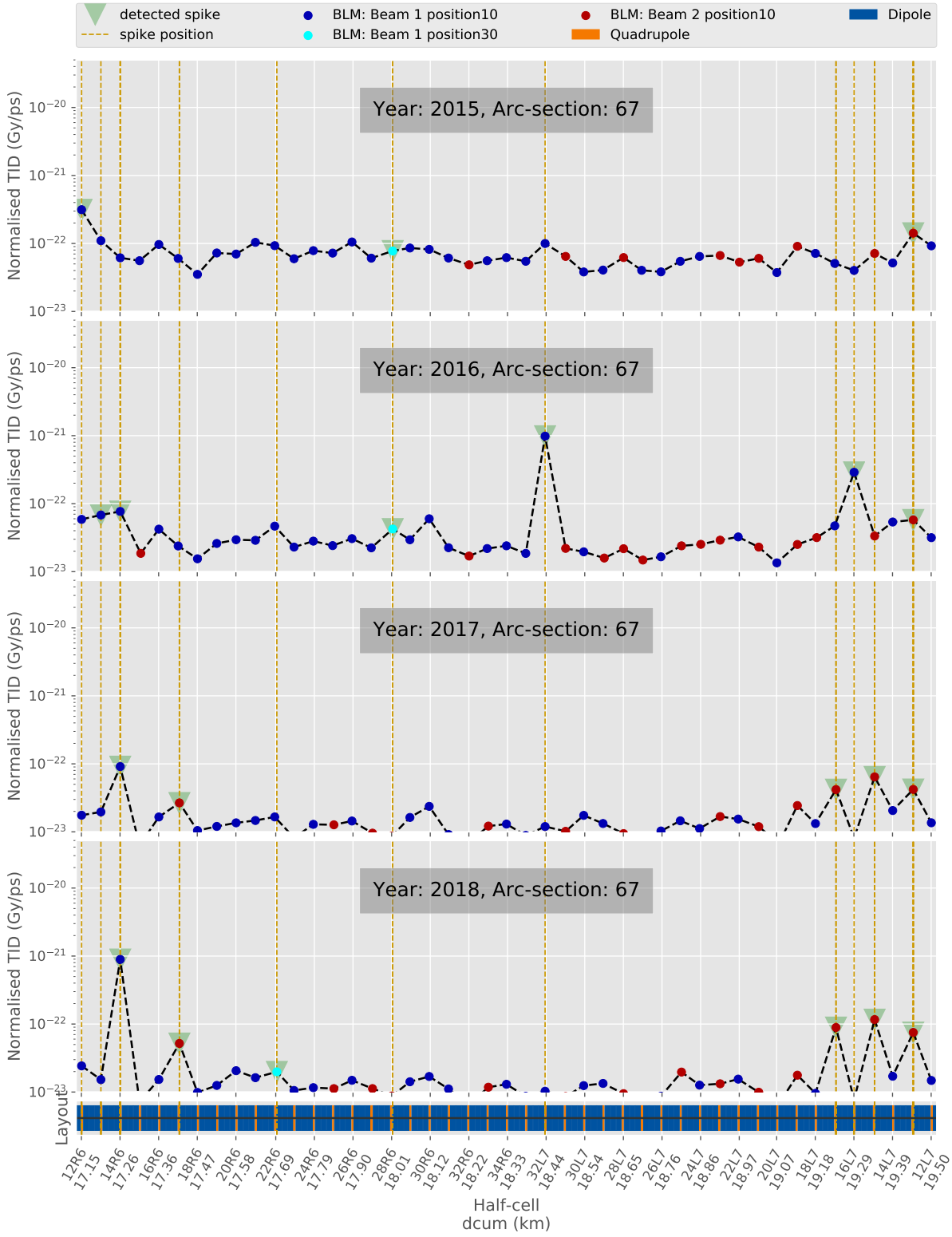

Figure 66: Normalised dose levels in the arc 67 for the years 2015-2018. Top BLMs are not considered and for each half-cell only BLM with highest dose is plotted.

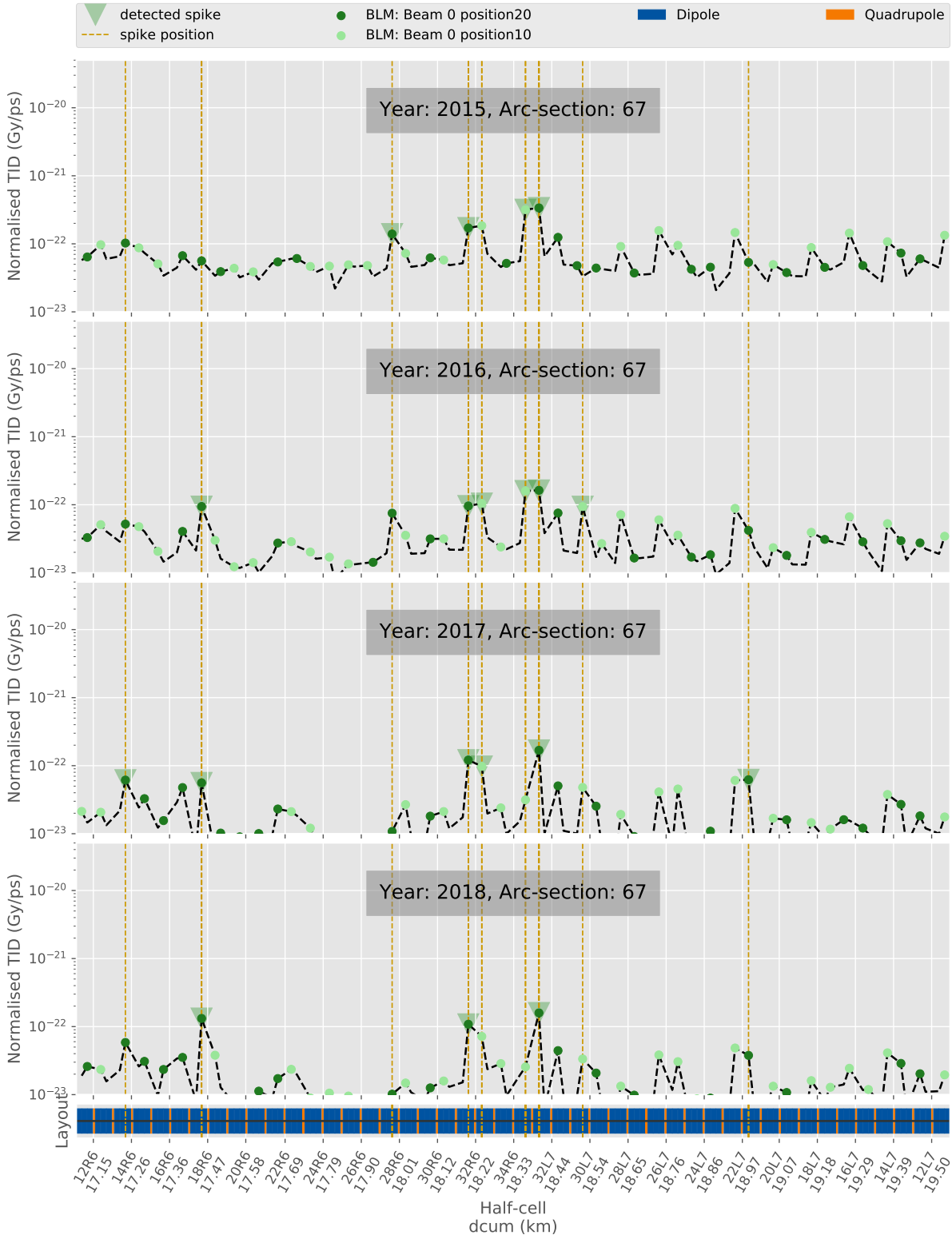

Figure 67: Normalised dose levels in the arc 34 for the years 2015-2018. Only top BLMs are considered.

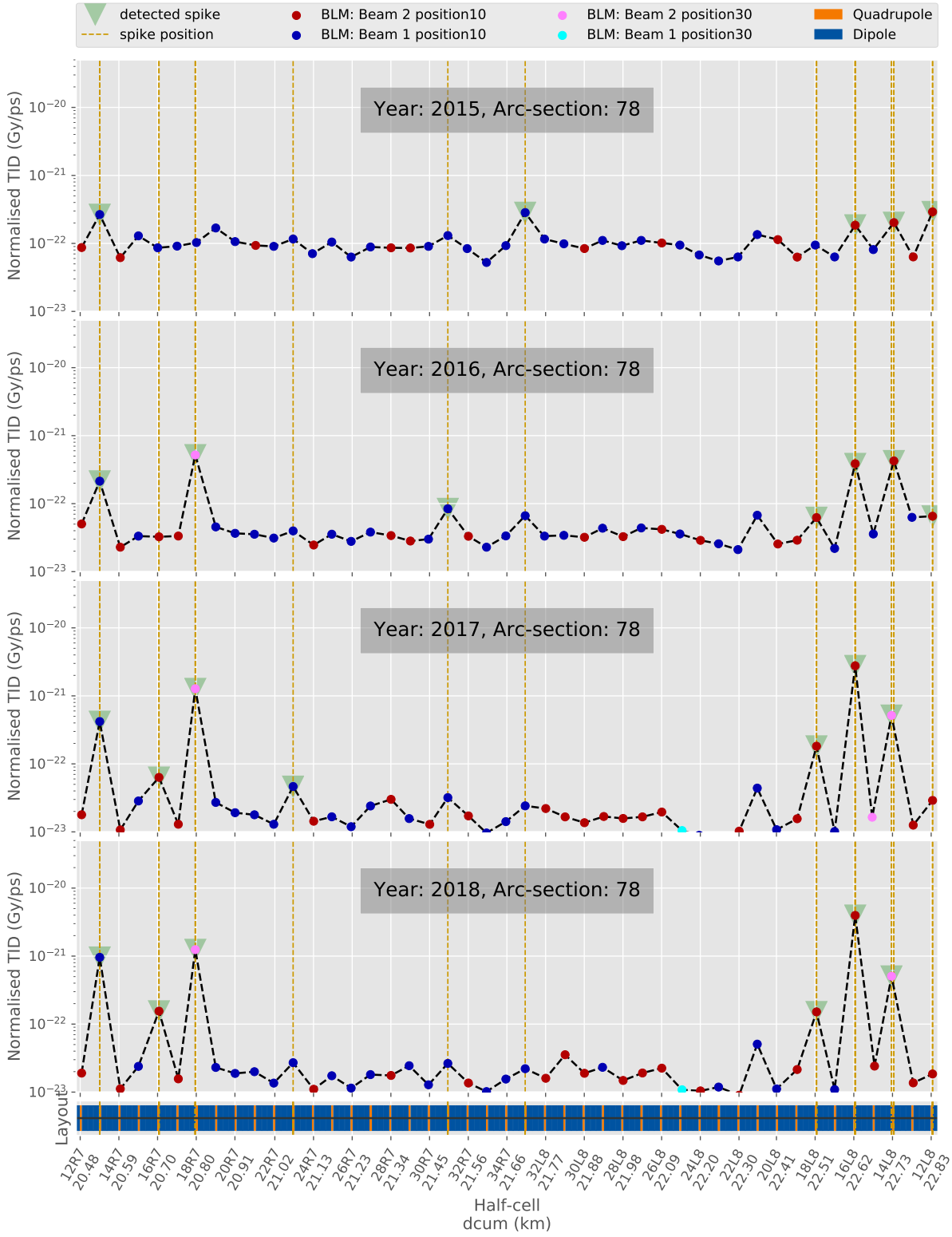

Figure 68: Normalised dose levels in the arc 78 for the years 2015-2018. Top BLMs are not considered and for each half-cell only BLM with highest dose is plotted.

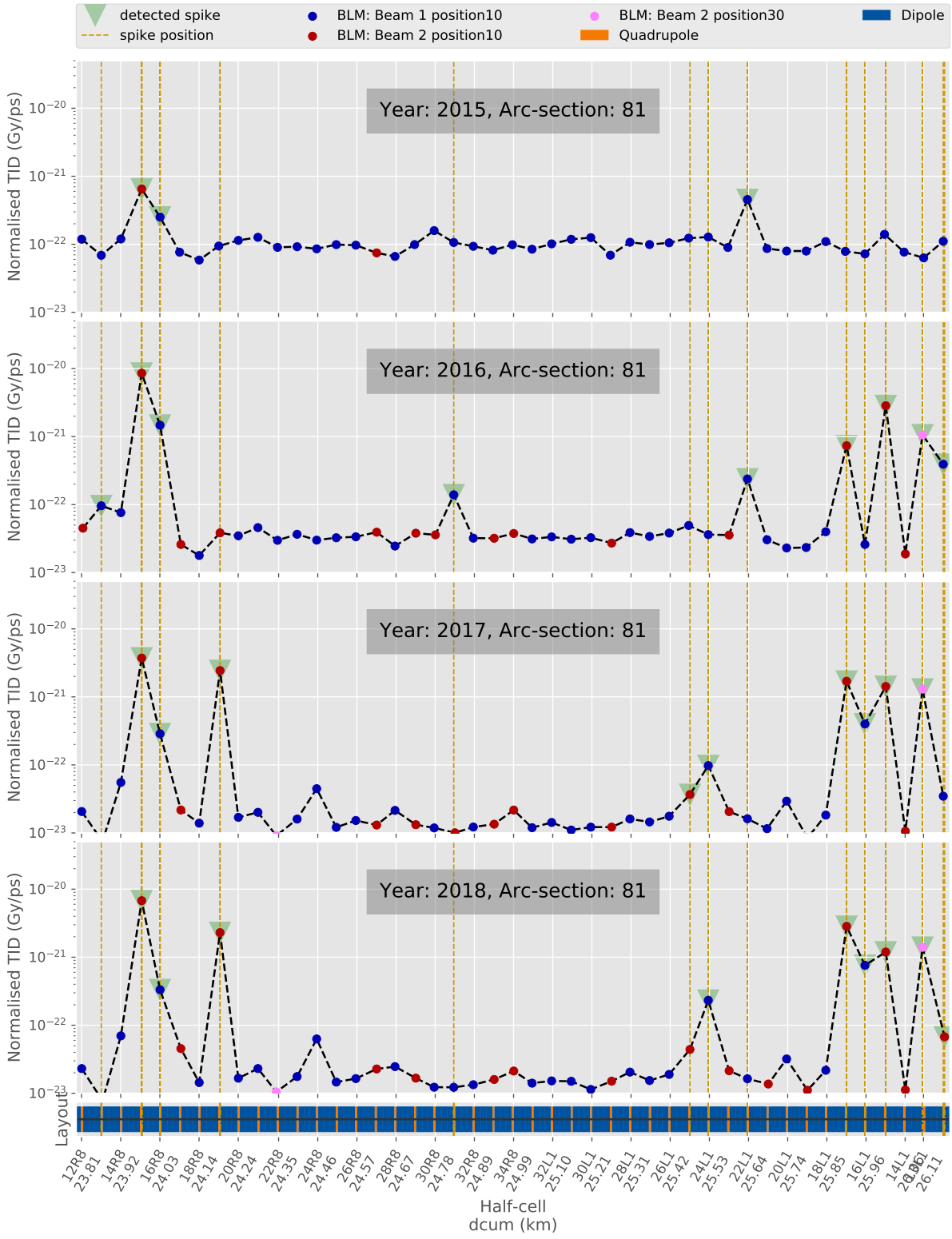

Figure 69: Normalised dose levels in the arc 81 for the years 2015-2018. Top BLMs are not considered and for each half-cell only BLM with highest dose is plotted.

References

[1] R. Alemany, M. Lamont, and S. Page. *Functional specification: LHC MODES*. Tech. rep. 865811. Geneva: CERN, Oct. 2009. URL: https://edms.cern.ch/file/865811/1.1/LHC-OP-ES-0005-10-10.pdf.

[2] R. García Alía et al. „LHC and HL-LHC: Present and Future Radiation Environment in the High-Luminosity Collision Points and RHA Implications". In: *IEEE Transactions on Nuclear Science* 65.1 (Jan. 2018), pp. 448–456. ISSN: 0018-9499. DOI: 10.1109/TNS.2017.2776107.

[3] K. Bilko. *LHC dependency between scrubbing and doses*. June 28, 2018. URL: https://indico.cern.ch/event/724716/contributions/2981030/attachments/1638205/2614614/LHC_dependency_between_scrubbing_and_doses.pdf.

[4] Leo Breiman. „Random Forests". In: *Machine Learning* 45.1 (Oct. 2001), pp. 5–32. ISSN: 1573-0565. DOI: 10.1023/A:1010933404324. URL: https://doi.org/10.1023/A:1010933404324.

[5] Maximilien Brice. „Views of the LHC tunnel sector 3-4." Oct. 2009. URL: https://cds.cern.ch/record/1211045.

[6] Oliver S. Bruning et al. „LHC Design Report Vol.1: The LHC Main Ring". In: (2004). URL: http://cds.cern.ch/record/782076/files/CERN-2004-003-V1.pdf?version=2.

[7] Serge Dailler. „Schematic layout of one LHC cell (23 periods per arc).. Shéma de présentation d'une cellule LHC (23 périodes par arc)." AC Collection. Legacy of AC. Pictures from 1992 to 2002. Oct. 1999. URL: https://cds.cern.ch/record/842724.

[8] L.D. Edmonds et al. *An Introduction to Space Radiation Effects on Microelectronics*. JPL publication. Jet Propulsion Laboratory, National Aeronautics and Space Administration, 2000. URL: https://books.google.ch/books?id=3azqHAAACAAJ.

[9] Werner Herr and B Muratori. „Concept of luminosity". In: (2006). URL: http://cds.cern.ch/record/941318.

[10] K. E. Holbert. „RADIATION EFFECTS AND DAMAGE ". URL: http://holbert.faculty.asu.edu/eee560/RadiationEffectsDamage.pdf.

[11] Eva Barbara Holzer et al. „Beam Loss Monitoring for LHC Machine Protection". In: *Physics Procedia* 37 (2012). Proceedings of the 2nd International Conference on Technology and Instrumentation in Particle Physics (TIPP 2011), pp. 2055–2062. ISSN: 1875-3892. DOI: https://doi.org/10.1016/j.phpro.2012.04.110. URL: http://www.sciencedirect.com/science/article/pii/S1875389212019281.

[12] Eva Barbara Holzer et al. „Design of the Beam Loss Monitoring System for the LHC Ring". In: (2004), 3 p. URL: http://cds.cern.ch/record/823249.

[13] A. Holzner. *Magnetic field of an idealized quadrupole with forces*. May 11, 2018. URL: https://en.wikipedia.org/wiki/File:Magnetic_field_of_an_idealized_quadrupole_with_forces.svg.

[14] Giovanni Iadarola. *e-cloud and heat load in the LHC arcs*. URL: https://indico.cern.ch/event/740046/attachments/1689072/2717155/022_abp_forum.pdf.

[15] Giovanni Iadarola et al. „Analysis of the beam induced heat loads on the LHC arc beam screens during Run 2". In: (Dec. 2017). URL: http://cds.cern.ch/record/2298915.

[16] J.M. Jimenez et al. „Observations, Analysis and Mitigation of Recurrent LHC Beam Dumps Caused by Fast Losses in Arc Half-Cell 16L2". In: *Proc. 9th International Particle Accelerator Conference (IPAC'18), Vancouver, BC, Canada, April 29-May 4, 2018*. (Vancouver, BC, Canada). International Particle Accelerator Conference 9. https://doi.org/10.18429/JACoW-IPAC2018-MOPMF053. Geneva, Switzerland: JACoW Publishing, June 2018, pp. 228–231. ISBN: 978-3-95450-184-7. DOI: doi:10.18429/JACoW-IPAC2018-MOPMF053. URL: http://jacow.org/ipac2018/papers/mopmf053.pdf.

[17] *LHC Optics Web: LHC Run II pp physics optics*. Sept. 11, 2018. URL: http://abpdata.web.cern.ch/abpdata/lhc_optics_web/www/opt2017/.

[18] *LHC Schedule 2015*. June 28, 2018. URL: https://indico.cern.ch/event/367052/contributions/1782854/attachments/729631/1001227/LHC_Schedule_2015.pdf.

[19] *LHC Schedule 2016*. June 28, 2018. URL: https://beams.web.cern.ch/sites/beams.web.cern.ch/files/schedules/LHC_Schedule_2016.pdf.

[20] *LHC Schedule 2017*. June 28, 2018. URL: https://beams.web.cern.ch/sites/beams.web.cern.ch/files/schedules/LHC_Schedule_2017.pdf.

[21] *LHC Schedule 2018*. June 28, 2018. URL: https://beams.web.cern.ch/sites/beams.web.cern.ch/files/schedules/LHC_Schedule_2018.pdf.

[22] Esma Mobs. „The CERN accelerator complex. Complexe des accélérateurs du CERN". In: (July 2016). General Photo. URL: https://cds.cern.ch/record/2197559.

[23] C. Pralavorio. *Chasing clouds in the LHC*. Sept. 11, 2018. URL: https://home.cern/about/updates/2015/06/chasing-clouds-lhc.

[24] *Restarting the LHC: Why 13 Tev?* URL: https://home.cern/about/engineering/restarting-lhc-why-13-tev.

[25] K. Roeed et al. „Method for Measuring Mixed Field Radiation Levels Relevant for SEEs at the LHC". In: *IEEE Transactions on Nuclear Science* 59.4 (Aug. 2012), pp. 1040–1047. ISSN: 0018-9499. DOI: 10.1109/TNS.2012.2183677.

[26] *SQLAlchemy*. June 28, 2018. URL: https://www.sqlalchemy.org/.

[27] R. Steerenberg. *LHC Report: An eventful and successful 2017*. Sept. 11, 2018. URL: https://home.cern/cern-people/updates/2017/12/lhc-report-eventful-and-successful-2017.

[28] R. Steerenberg. *LHC report: full house for the LHC*. Sept. 11, 2018. URL: https://home.cern/cern-people/updates/2017/07/lhc-report-full-house-lhc.

[29] O. Stein, K. Bilko, et al. „A Systematic Analysis of the Prompt Dose Distribution at the Large Hadron Collider". In: *Proc. 9th International Particle Accelerator Conference (IPAC'18), Vancouver, BC, Canada, April 29-May 4, 2018*. (Vancouver, BC, Canada). International Particle Accelerator Conference 9. https://doi.org/10.18429/JACoW-IPAC2018-WEPAF082. Geneva, Switzerland: JACoW Publishing, June 2018, pp. 2036–2038. ISBN: 978-3-95450-184-7. DOI: doi:10.18429/JACoW-IPAC2018-WEPAF082. URL: http://jacow.org/ipac2018/papers/wepaf082.pdf.

[30] J. Wenninger. *LHC morning meeting - 04.10.2017*. June 28, 2018. URL: https://indico.cern.ch/event/667004/contributions/2726828/attachments/1533870/2403682/2017.10.04-morning-meeting.pdf.

[31] Andrzej Wolski. „Low-emittance Storage Rings". In: arXiv:1507.02213. arXiv:1507.02213 (July 2015). Presented at the CERN Accelerator School CAS 2013: Advanced Accelerator Physics Course, Trondheim, Norway, 18-29 August 2013, 245–294. 50 p. URL: http://cds.cern.ch/record/1982424.